Non-Conventional Diagnostics of Injection Process in Single Cylinder Compression Ignition Engine

Luigi Sequino

A thesis submitted to UNIVERSITÁ DEGLI STUDI DI NAPOLI FEDERICO II and produced in collaboration with ISTITUTO MOTORI – CNR of Napoli in fulfilment of the requirements for the Degree of Doctor of Philosophy

in

Mechanical Engineering

Scuola di dottorato in Ingegneria Industriale
Dottorato di ricerca in Ingegneria dei Sistemi Meccanici XXVIII Ciclo

2016

TUTOR

Prof. Ing. Fabio Bozza

Dr. Ing. Ezio Mancaruso

Dott.sa Bianca Maria Vaglieco

COORDINATOR

Prof. Ing. Fabio Bozza

Per aspera ad astra

Acknowledgments

I am grateful to all the people who guided and supported me during this PhD.

I want to thank dr. Bianca Maria Vaglieco and eng. Ezio Mancaruso of Istituto Motori for introducing me in the world of research. They always believed in me and brought out the best of me, often more than I thought.
Thanks to prof. Fabio Bozza for being my University tutor.

It is fundamental to give the deserved recognition to all the researchers and students of Istituto Motori that contributed to the deepen of my technical knowledge: Paolo Sementa and Francesco Catapano, Silvana Di Iorio and Agnese Magno, Renato Marialto, Guido Marseglia, prof. Gaetano Continillo, Simone Lombardi and prof. Katarzyna Bizon.
The experimental activities would not have been in place without the technical support of two of the world's best technicians, thank you Carlo Rossi and Bruno Sgammato for your help.

Lastly, thanks to my parents for teaching me "everyday life" and how to face its difficulties. Pasquale, I cannot imagine a brother better than you.
Heartfelt thanks to Sara, the first encouragement the first criticism, we are good to improve each other.

Abstract

This thesis has been carried out in the Istituto Motori – CNR of Napoli. The mission of the institute is the research on engines and other kinds of propellers for the development of the future transport systems. The main targets of the research activities concern the reduction of pollutant emissions and fuel consumption of modern engines. A variety of experimental and numerical activities are carried out in the institute with the aim to understand the entire functioning chain of internal combustion engines. The research activities of the present doctoral thesis have been run in the optical diagnostics laboratory. In particular, the present work focuses on the analysis of the injection process in a single-cylinder compression ignition engine via direct imaging with high speed cameras. The research engine is derived from a light duty production engine and is fed with commercial Italian diesel fuel. The engine performances have been analyzed in seven operating conditions that are representative of the engine behavior during the homologation cycle New European Driving Cycle (NEDC) when installed on a D-class vehicle.

The approach used in this work for the investigation of in-cylinder processes is based on the combination of experimental activities and numerical simulations. A mono-dimensional (1d) model developed by the Sandia National Laboratories to simulate the fuel injection in a control volume combustion vessel has been implemented and adjusted to fit in-cylinder thermodynamic conditions and geometrical limitations. The model has been set up using experimental data collected on the single-cylinder optical engine. The thermodynamic parameters have been collected in conjunction to images of the injection process in the visible range. A sensitivity analysis to the model input values has been made and by comparing the model result to injection images it has been possible to understand the model limitations and potentialities. It has revealed to work well for the simulation of the injection process inside the engine and could provide additional information to the investigated phenomena. For example, the jet/wall interaction has been investigated and the fuel mass impinging on the combustion chamber wall has been correlated to the exhaust emissions of particulate matter (PM). Moreover, the model has been able to provide both the penetrations of the liquid and vapor fuel. Whereas visible imaging of the injection process could provide only images of the fuel liquid phase, it could be very useful to get information about the vapor phase too. The 1d model has revealed to be a valid support for the development of a novel optical technique for the visualization of the vapor fuel using infrared imaging. As aforementioned, visible imaging is able to detect only the fuel liquid phase; for the visualization of the fuel vapor phase there exist several optical techniques characterized by

complex set up and high sensitivity to fuel impurities and geometrical limitations. On the contrary, infrared imaging is able to overcome the limitations of the previous diagnostics. For this reason, this technique has been setup and applied for the optical diagnostics in the single-cylinder research engine. The spectral analysis in the range 1.5-5 μm allowed to identify two wavelengths to investigate: at 3.4 μm and at 3.9 μm. The penetration curves obtained from the infrared images have been compared to the ones from visible images and from the model (liquid and vapor penetrations). The two selected wavelength, 3.4 μm and 3.9 μm, demonstrated to be good for the visualization in the infrared of the vapor and liquid phase, respectively. According to these observations, a more accurate analysis of the infrared radiation of the fuel jets and the modeled fuel evaporation rate allowed to understand better the fuel vaporization process.

The results reported in this doctoral thesis, the description of the 1d model of fuel injection inside the engine, and the presentation of an innovative optical technique in the infrared for the detection of the fuel vapor phase could contribute to the present scientific context for the development of sustainable transport systems with low environmental impact.

Contents

Introduction

1 Introduction

1.1 Background

1.1.1 Internal combustion engines

The internal combustion engine is so far the most common form of engine or prime mover. It has had an important impact on society through improved transportation and industrial applications. Although the basic principle of the four-stroke engine has not changed since Beau de Rochas' patent in 1862, engines have continuously been under development. In 1876, Nicolaus Otto presented the first four-stroke gas engine (spark assisted ignition, SI) [1]. Rudolph Diesel built the first compression ignition (CI) engine in 1892, the so-called diesel engine [2]. As with most engines the usual aim has been to achieve a high work output with a high efficiency; in the second half of the twentieth century the focus has shifted to the development of more efficient and cleaner engines. Fuel consumption became a major constrain as well as emission of specific pollutants for the exhaust tail pipe. This major shift was due to awareness from governmental authorities of atmospheric pollution induced by the extensive usage of internal combustion engines [3]. Concerns about the effects of greenhouse gases (GHG) on climate change have brought carbon dioxide (CO_v), a major GHG, to the front scene of emissions discussions. A recent analysis showed that, in Italy, the production of GHG due to transport sector was 103 million tons CO_2 equivalent in 1990, to become 128 million tons in 2005, and to decrease again to 103 million tons in 2013 [4]. These data show the importance of the research towards more fuel-efficient engines and other technologies leading to lowered carbon dioxide emissions.

In September 2015 the automotive world has been shocked by the "Dieselgate", the German carmaker Volkswagen Group was found to intentionally program turbocharged direct injection (TDI) diesel engines to activate certain emissions controls only during laboratory emissions testing to meet US standards [5]. But these vehicles emit up to 40 times more NOx in real-world driving. Then, also gasoline direct injection engines have been indicted [6, 7].

This episode points out the close relationship between ecology and economy. Advanced technologies are continuously developed to reduce engine pollutant emissions in order to preserve the environment. At the same time, that technological level allows the carmaker to be on the market. For this reason, it is fundamental to be always updated on the most advanced technologies in order to prevent unfair episodes like this.

To this purpose, diesel engines are constantly improved. This process passes through the deep investigation of the whole functioning chain, from the intake air and injection systems, to in-cylinder processes, up to after-treatment systems.

1.1.2 Benefits of Compression Ignition Engines

The compression ignition engines have a higher maximum efficiency than the spark ignition engines for different reasons. CI engines can have a higher compression ratio because only air is aspired in the cylinder, while the fuel is injected in the end of the compression stroke. Furthermore, the air/fuel mixture is always weak of stoichiometric, in order to achieve complete combustion. The fuel is injected into the combustion chamber towards the end of the compression stroke. Thus, the power can be regulated by varying the quantity of fuel injected with no need to throttle the air supply that increases the pumping work. Finally, the diesel engine is designed to operate at lower speeds and consequently the frictional losses are smaller.

1.2 Objectives and scope of the thesis

As aforementioned, the development of modern diesel engine is in continuous progress and many efforts are being made to fulfill emissions legislations. As new challenges arise, deeper insights in the understanding of the combustion process are needed. Optical diagnostics provided considerable insights for the development of modern diesel engines. Several optical methods have been adopted in order to investigate all the steps of the functioning chain of internal combustion engine (ICE) [8]. For example, the visualization of the spray injection is performed via Mie Scattering, Schlieren, and shadowgraph techniques [9, 10]. For the analysis of the species formed during the combustion process, emission spectroscopy in the UV-visible range, Laser Induced Incandescence, chemiluminescence, Laser Induced Fluorescence, and Raman spectroscopy are used [8, 11]. The investigation of the infrared spectrum has been always limited to the spectroscopic emission [12, 13]; on the other hand, it can reveal to be a very powerful tool for the investigation of all the aforementioned in-cylinder processes with benefits in terms of ease of application and amount of provided information.

To this purpose, this thesis focused on the application of an innovative optical diagnostics to a research engine for the investigation of in-cylinder processes. The new technique, set up in this work, consists of 2d infrared imaging of injection and combustion phenomena at high temporal and spatial resolution. The infrared range has been investigated at different wavelengths. The main advantage of using this technique is to visualize the fuel vapor distribution having at the same time a very simple optical setup compared to well-known techniques like Schlieren, LIF,

shadowgraph etc. Moreover, by using the appropriate filter in the infrared, also the fuel liquid phase can be detected.

Another fundamental tool for the development of modern engines is modeling. The combination of experimental and model tests has spread widely in the research and industrial contest to reduce costs and to get additional information not available from experimental measurements.

A key point of the present work concerned the adaptation of an already made 1d model of fuel injection to in-cylinder conditions. The original model is the one from Siebers and Musculus' works [14, 15] and it was built up to constant volume environment. To reproduce in-cylinder conditions, the variation of thermodynamic properties and the jet/wall interaction have been implemented in the original model. Since the injection process is fundamental for the air-fuel mixing that affects the subsequent formation of the pollutant emissions, new technologies are constantly developed and it is subject to continuous studies. To this aim, the model has been used to better comprehend the fuel injection process. The predicted and experimental liquid and vapor penetrations have been compared in order to get additional information about this process.

Some results of the present work concerned the analysis of the correlation between the equivalent ratio along the jet axis and the infrared emission, the correlation between the fuel that impinges on the combustion chamber wall and the exhaust pipe particulate matter (PM) emissions, and the evaluation via 1d model of the fuel evaporation rate.

1.3 Approach

In this work, the injection process of a Common Rail injection system was investigated in an optical engine equipped with the head of a Euro 5, 1.9l commercial diesel engine. The main tool for the investigation of the in-cylinder processes was the optical diagnostics in terms of visible and infrared imaging. The tests selected for this analysis reproduce the behavior of the real engine when performing the homologation cycle NEDC (New European Driving Cycle). Seven operating conditions at different engine speeds and loads were chosen. Typical multi-injection strategies with a pilot and main injections were performed. A well-established 1d model for the simulation of the injection process has been used to get more insights in the investigated phenomena.

1.4 Thesis contributions

The main purpose of this PhD thesis has been to provide new tools for the analysis of the injection process in an optical engine. The contributions concerned both a simple numerical approach to the problem and the presentation of an innovative non-conventional optical diagnostics.

A 1d model of fuel injection has been set up for engine environment. The simulation of in-cylinder processes provides additional information to experimental data and helps in their comprehension and explanation.

A new optical diagnostics for the detection of fuel liquid and vapor phases has been presented and its benefits have been illustrated. The results obtained using these techniques allowed to better understand the fuel evaporation process and air fuel mixing.

Chapter 2

Compression Ignition Engines

2 Compression Ignition Engines

2.1 Basic concepts

The main peculiarity of Compression Ignition (CI) engines is in the way the combustion is triggered. Whereas in Spark Ignition (SI) engines the spark provides the energy needed to the air/fuel mixture to burn, in CI engine the mixture auto-ignite when the proper thermodynamic conditions (pressure and temperature) inside the cylinder are reached. This process results in multiple simultaneous starts of ignition.

Diesel engines are divided into two basic categories according to their combustion chamber design: the direct injection (DI) engines, which have a single open combustion chamber where the fuel is injected directly; the indirect injection (IDI) engines, where the chamber is divided into two regions and the fuel is injected into the pre-chamber connected to the main chamber via either a nozzle or one or more orifices.

IDI engine designs are only used in the smallest engine size [2], this has lead DI engine designs to become the dominant type among nowadays compression ignition engines. The load is controlled by the amount of injected fuel while the combustion phasing is controlled by the injection timing. After the fuel is injected into the combustion chamber, the spray is atomized into small droplets, mixes with air, evaporates, and self-ignites due to the high in-cylinder pressure and temperature. The combustion event is strictly linked to a series of processes that concern physical (atomization, mixing) and chemical (evaporation, auto-ignition) reactions of fuel and air. Hence, the injection process is a crucial operation for an efficient mixture formation in a diesel engine and for this reason it has been extensively investigated [16-19].

2.2 Injection process

Fuel is injected in the combustion chamber at pressures of up to 3000 bar through small orifices which diameter is about 180 microns and less. These conditions ensure the fuel atomization at the nozzle exit. The liquid enters the combustion chamber with velocities of up to 500 m/s and the jet breaks up according to the mechanisms of the atomization regime [20].

2.2.1 Break-up

The break-up of droplets in a spray is caused by aerodynamic forces (friction and pressure) induced by the relative velocity between droplets and surrounding gas. The aerodynamic forces result in an instable growing of waves on the gas/liquid interface or of the whole droplet itself, which finally leads to disintegration and to the formation of smaller droplets. These droplets are

again subject to further aerodynamically induced break-up. The surface tension force on the other hand tries to keep the droplet spherical and counteracts the deformation force [21].

Immediately after leaving the nozzle hole, the jet starts to break up into a conical spray. This first break-up of the liquid is called primary break-up and results in large ligaments and droplets that form the dense spray near the nozzle. In case of high-pressure injection, cavitation and turbulence, which are generated inside the injector holes, are the main responsible for break-up mechanisms. The subsequent break-up process of already existing droplets into smaller ones is called secondary break-up and is due to aerodynamic forces caused by the relative velocity between droplets and surrounding gas [22].

During the fuel injection process, a conical spray is formed that is more and more diluted downstream the nozzle by the entrainment of air. Most of the liquid mass is concentrated near the spray axis, while the outer spray regions contain less liquid mass and more fuel vapor [20].

In the dense spray, the probability of droplet collisions is high. These collisions can result in a change of droplet velocity and size. Droplets can break up into smaller ones, but they can also combine to form larger drops, this phenomenon is called droplet coalescence [23].

Numerous fundamental experiments and semi-empirical relations about the general behavior of the relevant spray parameters of diesel sprays such as spray cone angle, spray penetration, break-up length, and average droplet diameter as a function of the boundary conditions have been performed and published by many different authors [18, 24-27]; they contributed in the understanding of such a complex phenomenon.

2.2.2 Theoretical correlations for the jet penetration

Several researchers studied the front penetration and found correlations that allowed to establish the main variables that affect the penetration of a diesel spray.

Dent (1971) [28] was one of the pioneers in the study of spray phenomena. He proposed an experimentally adjusted correlation which is applicable to pulsed diesel sprays:

$$S(t) = 3.07\left(\frac{\Delta P}{\rho_a}\right)^{\frac{1}{4}}\left(\frac{294}{T_a}\right)^{\frac{1}{4}}\sqrt{d_0 t} \qquad Eq.(2.1)$$

Where ΔP is the difference between injection and ambient pressure, ρ_a is the ambient density, T_a is the ambient temperature, d_0 is the nozzle nominal diameter, and t is the injection duartion.

Hiroyasu and Arai in 1990 [24] proposed two expressions to determine the sprays penetration as a function of the time of break-up (t_{br}).

$$t_{br} = 29\frac{\rho_f d}{\sqrt{\rho_a \Delta P}} \qquad Eq.(2.2)$$

$$S(t) = 0.39\sqrt{\frac{2\Delta P}{\rho_f}\cdot t} \qquad t < t_{br} \qquad Eq.(2.3)$$

$$S(t) = 2.95\left(\frac{\Delta P}{\rho_a}\right)^{0.25}\sqrt{d_0 t} \qquad t > t_{br} \qquad Eq.(2.4)$$

where ρ_f is the fuel density.

An empirical equation considering the dimensionless parameter $\rho^* = (\rho_a/\rho_f)$ was developed by Jiménez et al. in 2000 [29] obtaining the following expression:

$$S(t) = 0.6^{-3}U_0 t^{0.9}\left(\frac{\rho_a}{\rho_f}\right)^{-0.163} \qquad Eq.(2.5)$$

where Uo is the medium velocity at the beginning of the injection.

From the derivation of the expressions developed by Dent [28] and Arai [26], Bae et al. in 2000 [30] proposed the following expression for the penetration of the spray:

$$S(t) = C\left(\frac{\Delta P}{\rho_a}\right)^{0.25}\sqrt{d_0 t} \qquad Eq.(2.6)$$

$$t = t_0 = \sqrt{\frac{\rho_f}{\rho_a}}\left(\frac{d_0}{U_0}\right) \qquad Eq.(2.7)$$

As a summary it can be said that the penetration of the spray basically depends on the following parameters:

-Injection pressure ΔP: Increasing the injection pressure, the velocity of the penetration of the spray increases and hence the development of the spray will be easier [25, 26].

-Density ratio (ρ*): this dimensionless parameter ρ* or relation of densities, according to [25-27] considerably affects the penetration of the spray because of the increase or decrease of the aerodynamic interaction. High relation of densities causes the penetration to reduce considerably.

-Working fluid temperature (Ta): density reduction can be caused by the increase of the working fluids temperature, hence, the decrease of spray penetration.

2.3 Combustion process

As fuel is injected directly in the combustion chamber where high pressure and temperature air is present, there is not a homogeneous mixture at the start of combustion but different zones are formed. Dec proposed a conceptual model describing DI diesel combustion for a single injection event near the Top Dead Center (TDC) [31, 32]. This representation of diesel combustion is appropriate for typical heavy-duty diesel engines operating at moderate to high load conditions. The quasi-steady diesel spray during the mixing controlled part of combustion prior to the end of injection is depicted in Figure 2.1.

The quasi-steady jet in the figure is divided in several specific zones that describe what happens to the fuel from its entering in the cylinder. Liquid fuel penetrates in the combustion chamber from the nozzle on the left side of the image and mixes with the hot compressed air. The air entrainment increases as the fuel penetrates, the droplets begin to vaporize and downstream of the liquid-phase region of the spray, a fuel-rich mixture zone establishes. When the temperature inside this fuel-rich zone reaches about 750 K, the first reactions, resulting in a breakdown of high cetane fuel, begin to occur. These reactions, as well as the further entrainment of hot air and the additional compression of the cylinder charge, increase the temperature and the rate of the reactions. This results in a burning of the complete fuel-air mixture that has been formed since the start of injection (this period is called ignition delay).

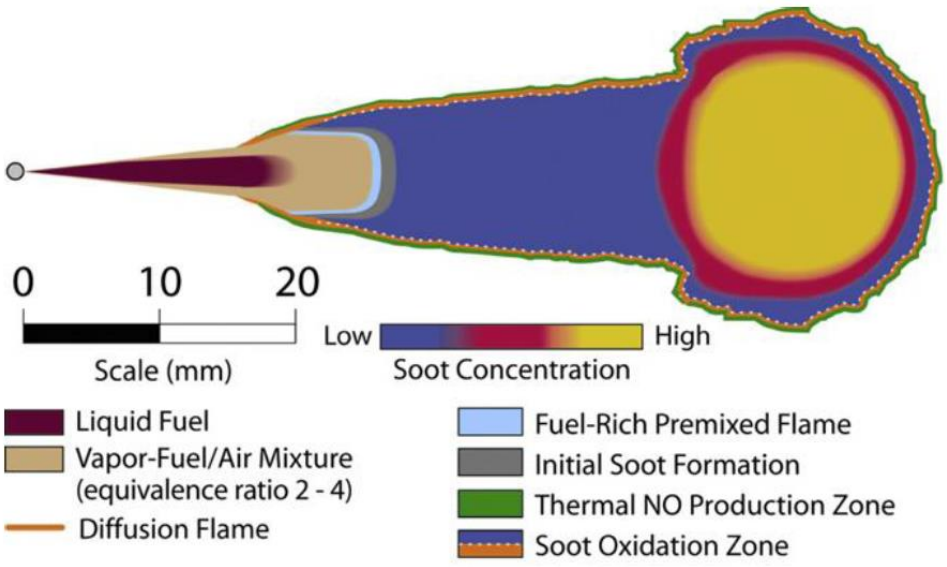

Figure 2.1: Conceptual model of a quasi-steady diesel spray. Reproduced from [31].

The combustion of premixed fuel-air mixture produces a strong and sudden increase of heat release and in-cylinder pressure. The high temperatures involved are responsible for a first production of NOx. Values of about 2000 K must be reached in order to split the triple bond of N2-molecules and then to enable the formation of NOx according to the Zeldovich mechanism [33].
After the combustion of premixed fuel-air mixture, air and partial burnt products are burnt in a very thin reaction zone at the periphery of the spray, the so-called diffusion flame. This kind of combustion is limited by the mixing of partial burnt products and air, resulting in a slower reaction compared to the premixed one. The fresh injected fuel upstream of the jet is quickly heat up by the hot air and combustion products entrainment. Due to the lack of oxygen in the inner region of the spray, the fuel is partially oxidized. This, in combination with the high temperature due to the diffusion flame, realizes the conditions for the formation of soot [34].
The products from inside this partial oxidation zone diffuse to the boundary and are consumed by the diffusion flame. This is fed with oxygen from the surrounding and therefore near stoichiometric equivalence ratios are reached on the flame boundary. Due to the very high temperatures, about 2700 K, nearly all soot that reaches the border of the diffusion flame is consumed. On the other hand, here there is enough oxygen to produce large amounts of NOx [20].

2.4 In-cylinder pollutants formation and oxidation

Particulate and NOx emissions are considered as the major pollutants of a diesel engine, for this reason their formation and reduction mechanisms have been deeply investigated in combustion studies [1, 35-37]. Particulates are the combination of soot formed inside the cylinder and other liquid or solid phase materials that are collected during the exhaust phase in the exhaust pipe. Particulate matters at the exhaust consist of soot for more than 50% while the other main sources are partially burned fuel and lubricant oil, bound water, wear metals and fuel-derived sulphate [38]. The formation of soot from vaporized fuel involves five main processes shown in Figure 2.2. First, the fuel molecule structure is modified without being oxidized even in the presence of oxygen, this process is called pyrolysis. These altered fuel molecules become soot precursors such as poly-aromatic hydrocarbons (PAH). The rate of reaction of the pyrolysis increases with temperature. Soot precursors form nuclei in the nucleation process. This phase consists of additions of small hydrocarbons to larger aromatic molecules.
These nuclei are very small and represent only a small fraction of the total soot mass. During the following phase, the surface growth phase, mass as hydrocarbons in gas-phase are added to the nuclei.

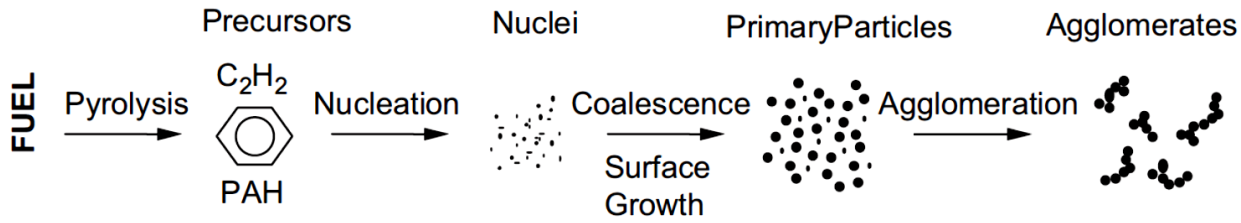

Figure 2.2: Schematic diagram of the step in the soot formation process from gas phase to solid agglomerated particles. Reproduced from [38].

Finally, these soot particles are combined through the coalescence and agglomeration phases. The coalescence process leads to larger spherical soot particles from the collision of smaller spherical particles; whereas the agglomeration phase forms groups or chains of primary particles [38].

The soot formation process is only half of the mechanism behind engine out soot emissions. Most of the soot formed is oxidized into CO or CO_2 before the exhaust valves open. More than 90 % of the formed soot is oxidized before leaving the combustion chamber in modern light-duty engines as shown in [39]. Oxidation can take place at any time in the process described above. Soot precursors as well as nuclei or agglomerates can be oxidized.

The second main pollutant in diesel engines is NOx, it identifies NO and NO_2 molecules. There are three main mechanisms for NOx-formation [40]. First, fuels containing organic nitrogen can form so-called fuel-NOx. Secondly, NOx can be formed in rich zones through the so-called prompt mechanism. Finally, NOx can be formed by reactions between N_2 and O_2 in the air. This mechanism is sensitive to temperature and is therefore called thermal NOx. It has a fast formation rate at high temperature. Fast cooling rates during expansion cause a freezing of the reactions. Thermal NOx is generally the dominant source in diesel combustion. The reactions describing thermal NOx formation are given by the extended Zeldovic-mechanism [2]:

$$O + N_2 \rightleftarrows NO + N$$

$$N + O_2 \rightleftarrows NO + O$$

$$N + OH \rightleftarrows NO + H$$

As seen in the formation processes of both soot and NOx, temperature is an important factor for the formation of pollutants. The local equivalence-ratio (Φ) is also central in the soot formation process, as richer mixtures will have a higher soot formation rate. These two parameters, i.e. temperature and equivalence ratio, were used in simulation work by Akihama et al. [41] and gave

a major insight into soot and NOx production mechanisms, notably by using the so-called Φ-T map introduced by Kamimoto and Bae [42].

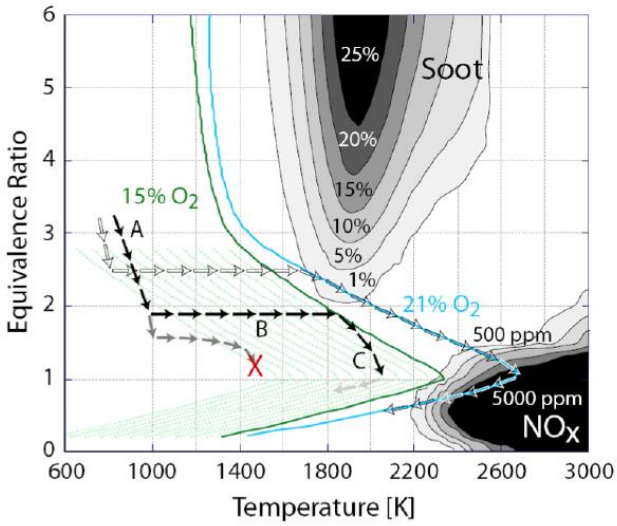

Figure 2.3: Equivalence ratio - temperature map.

Soot forms when a fuel element passes through the soot formation zone, which is located approximately between the temperatures 1600 and 2400 K, and a Φ-value greater than two.

NOx is formed at high temperature, above 2400 K, when equivalence ratios are around stoichiometric conditions.

Chapter 3

Optical Diagnostics in Compression Ignition Engines

3 Optical Diagnostics in Compression Ignition Engines

3.1 Optical engines

Optical diagnostics can provide deep understanding of the processes that take place inside the cylinder. In order to perform these measurements an optical access to the combustion chamber must be obtained. Optical engines are able to fulfill these requirements; they have the advantage of maintaining the main features of the original metal engine by providing the view of the cylinder inside. The amount of optical access varies; some optical engines only have access through an endoscope and others have most of the combustion chamber made of transparent parts.

The most widely used design in engine combustion research is the so-called Bowditch design, named for its inventor who developed it in General Motors research laboratories in 1961 [43]. The engine can be either based on multi-cylinder or single-cylinder architecture. To get the optical access, the cylinder head is separated from the cylinder block, and a piston extension is placed on the original piston in the block.

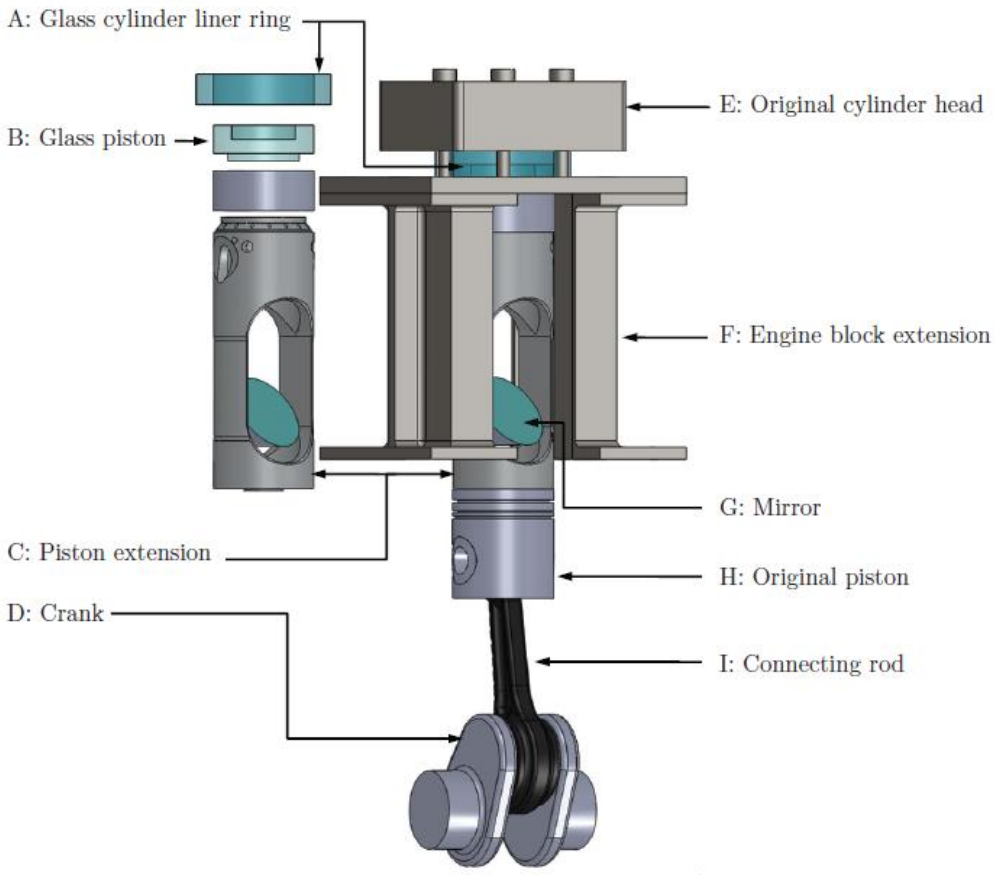

Figure 3.1: Optical engine of Bowditch design. Items A, B, C, F, and G are added to achieve optical access to the combustion chamber while the rest are all-metal engine parts. Reproduced from [44].

The piston elongation is hollow for fitting a 45-degree mirror inside it which allows viewing the combustion chamber from beneath. A completely transparent piston or modified with optical parts is mounted on the top of the piston elongation. Transparent parts are usually made of quartz or sapphire. An additional cylinder liner is finally added between the elongated cylinder and the engine head. Optical engines demonstrated to be a powerful and effective tool for the analysis of combustion processes and for this reason they have had a wide spread in the research context. As example, some images of optical engine test rigs used world-wide have been reported in figure 3.2. They refer to the light duty engine at the Wayne State University (Detroit, Michigan, USA), the heavy duty engine at the Sandia National Laboratories (Livermore, California, USA), the heavy duty engine at the Lund University (Lund, Sweden), and the light duty engine at the Istituto Motori (Napoli, Italy). As it can be seen in the figure, despite all engines adopt the Bowditch design they have been adapted in a different way depending on the various requirements. Moreover, both heavy and light duty engines can be converted into optical engines.

Finally, optical engines can be seen as complementary research tools in the middle between metal engines and constant volume combustion vessels.

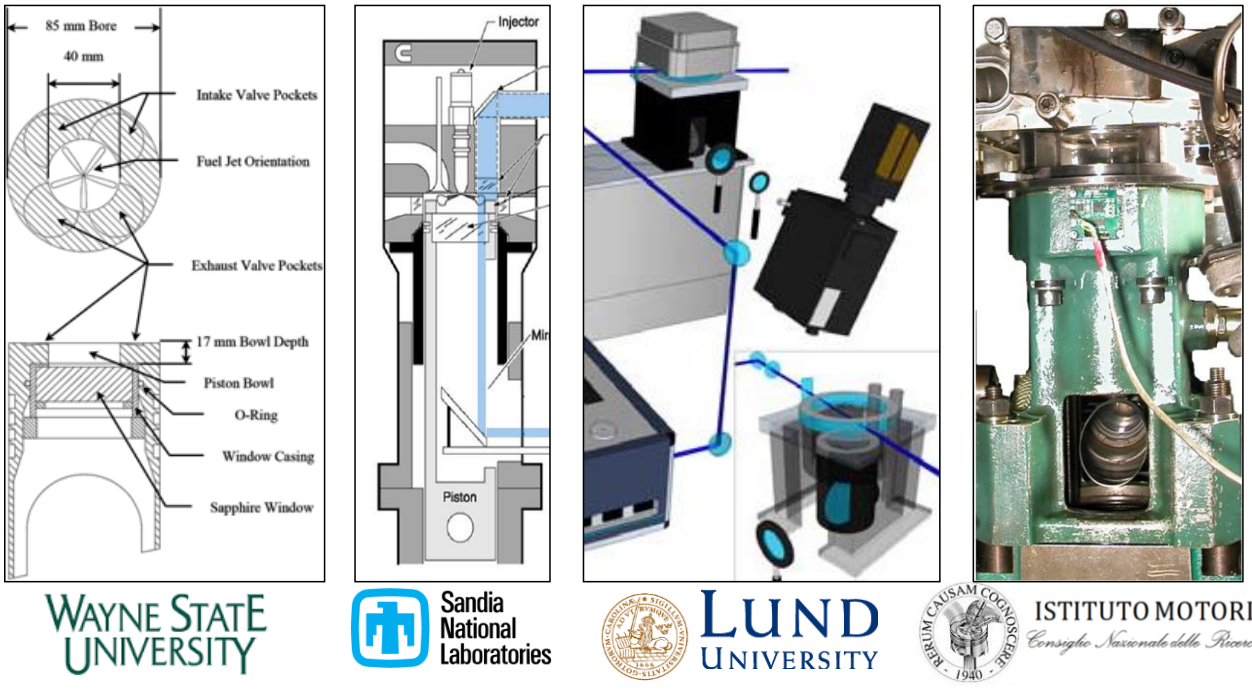

Figure 3.2: Examples of Bowditch based optical engine among different combustion research centers [45-48].

Compared to the former, they have the great advantage to provide the view of combustion process; on the other hand, in addition to the latter they can take into account volume/pressure variations, in-cylinder flows, jet-jet interactions and jet-wall interactions. These results combined

with the findings relative to different test rigs contribute additional knowledge of the complex combustion processes happening in a production engine.

3.2 Limitations of Optical Engines

There are some clear differences between the optical and the metal engines which lead to intrinsic limitations of the optical engine despite its close resemblance to a regular metal engine. First of all there are some obvious operating limitations due to the presence of optical components that lower the strength of overall structure and limit the load range of the engine. Added mass on the original piston with its extension limits the maximum engine speed due to increased mass forces that could damage the crankshaft. Having lower thermal conductivity than steel or aluminum, quartz parts have higher surface temperatures during operation. Heat transfer from the in-cylinder gases to the wall is reduced compared to a combustion chamber entirely made of metal parts. For this reason, optical engines are often operated in skip-fired mode, meaning that the combustion event is not realized every cycle in order to lower the components temperature.

The second group of limitations deals with the relative similarity of in-cylinder flow fields between metal and optical engines. Combustion chambers in production engines have a complex piston bowl geometry designed for maximizing combustion efficiency and limiting pollutants formation. The production of an optical piston with the same geometry can be hard and expensive. Moreover, the view of the combustion chamber results wrapped because of the optical deformations produced by curved surfaces. For this reason, optical pistons generally have a flat bowl that prevents image deformations. Of course, this kind of design affects the turbulent in-cylinder flow fields.

Another deviation from the metal case is the crevice flow between the cylinder liner and the piston. Piston rings are mounted on the lower part of the piston holder to avoid contact with optical windows, in a much lower position than usual. The top ring land is thus longer which increases the crevice volume. The flow from the crevice volume to the squish region and to the piston bowl is thereby altered. Furthermore non-metallic piston rings have to be used due to the absence of lubrication of the cylinder liner. The bowl-by flow through the piston rings can also in that way be affected. Finally, for safety, an extra margin is put on the squish height to prevent the transparent piston from touching the valves, mostly at gas exchange TDC. Although some of these differences are difficult to fully compensate for, optical engines still provide conditions that resemble those in real engines in many important aspects.

3.3 Optical diagnostics

Depending on the purpose of the optical engine investigation, different diagnostic techniques are used. There are two main classifications of optical measurement techniques: passive and active. In passive techniques, the phenomenon is imaged as it is without interference. All passive optical measurement techniques give a line of sight perspective of the combustion chamber. Therefore it is impossible to image the inside of a reacting diesel flame with passive measuring techniques. Another limitation is that only species that radiate naturally can be imaged. On the other hand, in active optical techniques, an external radiation source is used to actively generate the radiation from the measurement volume. This gives the opportunity to investigate the interior of the flame and more processes can be studied. Active optical techniques can be used to measure in a point, along a line, in a plane, or in three dimensions. The three dimensional measurements consist of several spatially dispersed planar images captured over a short time period. In combustion engine diagnostics the dominant radiation source is lasers [3, 49].

3.3.1 Passive optical diagnostics

They are generally used to impress images of the combustion process. The natural radiation of the combustion can be detected without external sources due to the natural luminosity in the UV and infrared ranges from different gas molecules. In particular, the soot luminosity is dominant and emits radiation over the whole spectrum as a black body radiator. The chemiluminescence arises from excited combustion radicals. One commonly imaged species is the hydroxyl radical (OH) that gives information of where high temperature reactions occur [50].

3.3.2 Active optical diagnostics

These techniques can be used for the investigation of both the injection and the combustion processes. Since the main focus of this work concerns the analysis of the fuel spray, a brief summary of the active optical diagnostics for the detection of fuel liquid and vapor phases will be presented. Figure 3.3 reports some examples of optical set up adopted to perform these diagnostics. The figure aims to highlight the complexity of these techniques and the high variety of components needed to perform them (light sources, lenses, number of optical accesses).

The most used techniques are shadowgraph, Schlieren, back-light illumination, Laser Induced Fluorescence (LIF), and Mie scattering [51- 54]. For the first three, a forward and backward access to the spray is needed, which limits their application to combustion vessels. LIF is the optical radiation from laser excited molecules that return from a higher to a lower energy state. This technique is suitable for optical engines because the light source and the detector can have an

angle of 90° allowing sending the light through the liner and collecting the image from beneath the piston. Mie scattering is also commonly used in optical engines due to the limited optical access needed. When the target particles have a size that is comparable to or larger than the laser wavelength it is called Mie scattering; it is suitable to image liquid fuel droplets and soot particles. In the case of the spray, it is illuminated by a laser light source and the elastically scattered light from the fuel droplets is spectrally isolated with an interference filter and collected on a video camera. Laser light is typically in the visible range at 532 nm [55]. The laser beam can be used as it is or can be converted into a laser sheet to perform a planar imaging.

To image the liquid phase of the fuel in this work, a simplified Mie scattering-based technique has been used. Two halogen lamps of 1000 W power have been used as light source in the visible range. The light is sent from beneath the piston that is the same location of the detector (camera). The liquid droplets scatter the light coming from the lamps that is collected from the camera. The resulting image is a line of sight perspective of the spray.

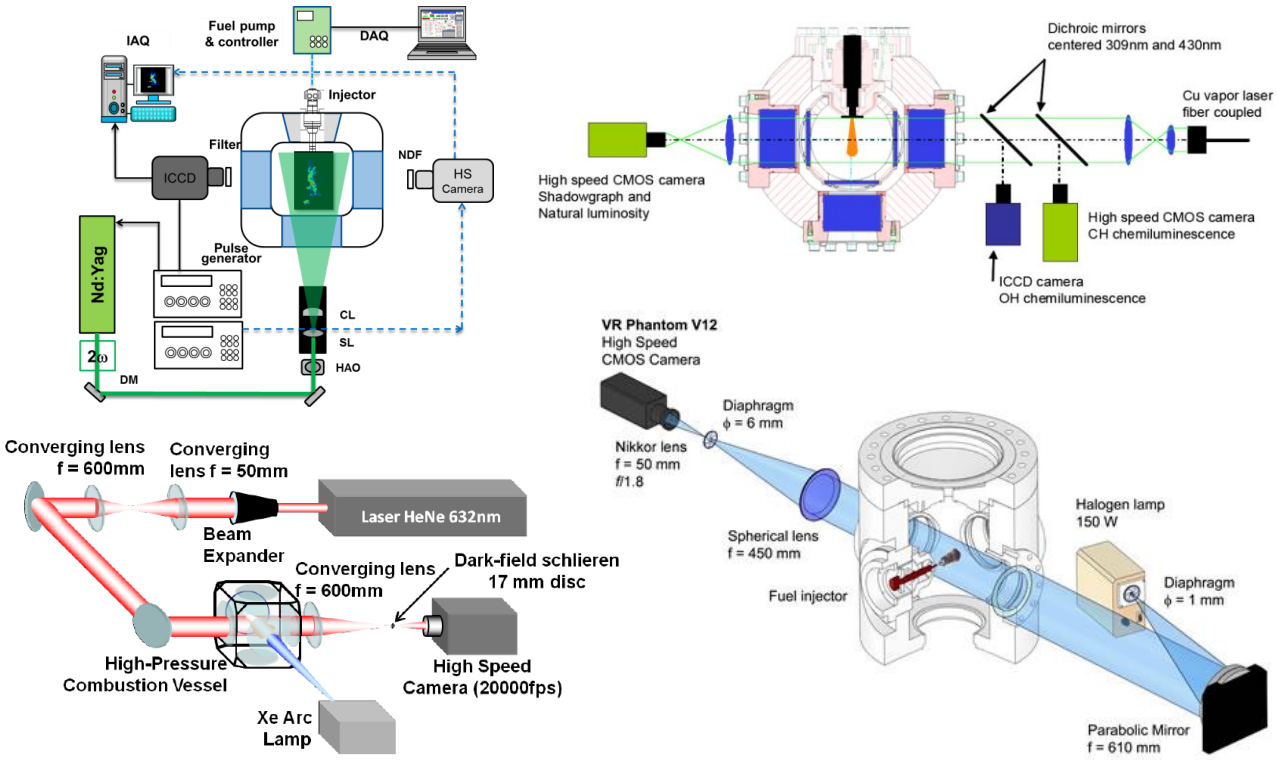

Figure 3.3: Examples of different set up for active optical diagnostics in a combustion vessel [51- 54].

3.3.3 Infrared diagnostics

As aforementioned, for the detection of the fuel liquid and vapor phase active optical diagnostics are applied as shadowgraph, Schlieren, Laser Induced Fluorescence [8, 10, 11]. Figure 3.3 shows how complex is the optical set up for these techniques. They need a light source that in some case must be a laser beam at a specified wavelength and power. The laser frequency is often an upper limit for the engine speed. Moreover, additional optical components are needed to obtain a planar sheet or to preserve the beam dimensions, e.g. dichroic splitter, polarizer, spherical or cylindrical lenses, band pass filters, prisms etc.… [10]. The application of some of these techniques is limited by the number of optical accesses needed. In some cases, as for the LIF, the directionality of the laser beam is a limit to the number of fuel jets that can be investigated. Laser sources are very susceptible to the window fouling that is a typical issue of optical engines. Also the fuel quality is important; whereas a target species needs to be excited, pure fuels which composition is known are used as surrogate of diesel fuel (e.g. n-dodecane, n-heptane, n-hexadecane etc.…) [55-57].

Each body which temperature is higher than 0 K emits energy in the form of electromagnetic waves in the infrared band that ranges from 0.76 μm to 1000 μm. It is divided into several regions (see figure 3.4): short wave infrared (from 0.76 μm to 2 μm), medium wave infrared (from 2 μm to 4 μm), and long wave infrared (from 4 μm to 1000 μm). Therefore, infrared diagnostics can be included among the passive optical diagnostics because the target does not need to be excited and an infrared camera can detect its natural emission. This advantage has allowed this technique to spread and to be applied in the engine research field. Two-dimensional (2d) imaging in the infrared band has been first used in the automotive sector to measure the temperature of the cylinder inner surfaces [58], to monitor the preheating plugs in diesel engines [59], to detect the brake thermal conditions [60], and to visualize the exhaust flow in catalytic converters [61]. However, 2d infrared imaging has never been used for the investigation of high speed phenomena as injection and combustion processes inside the engine.

In this work, 2d infrared diagnostics has been applied for the visualization of in-cylinder processes because it can help to overcome some of the limitations concerning active optical diagnostics described in the previous paragraph. The fuel liquid and vapor phases have been the targets of the investigation; however, by choosing the appropriate wavelength in the infrared also the combustion flames can be investigated. Moreover, only one optical access is required, this helps preserve the engine architecture. Finally, conventional fuels, as diesel, can be used instead of surrogates since they have themselves an infrared emission that can be collected.

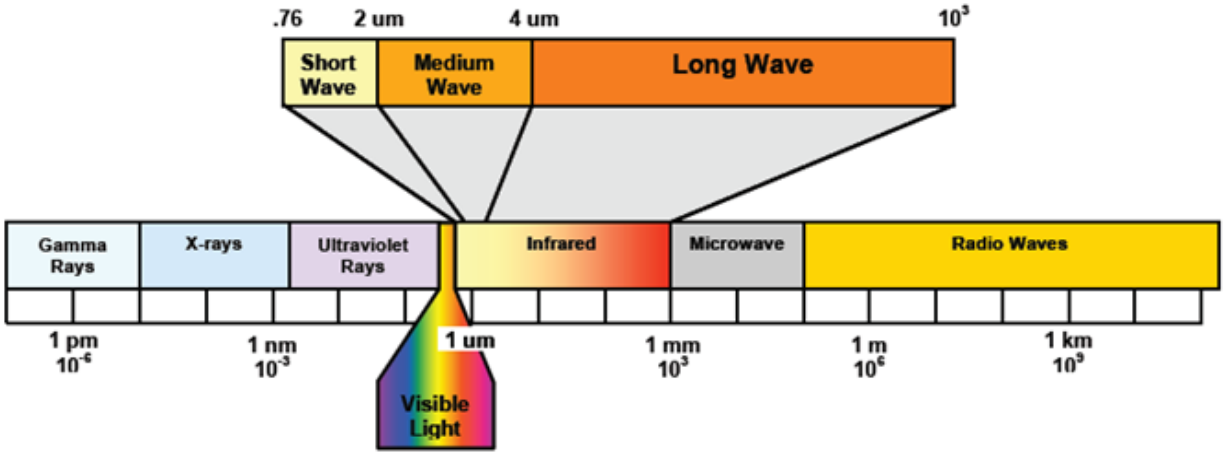

Figure 3.4: **The visible and infrared bands in the electromagnetic spectrum.**

Chapter 4

1d Model of Fuel Injection

4 1d Model of Fuel Injection

4.1 Siebers' liquid length scaling law for diesel spray

As engine technology advances, new computational models are being developed. With the introduction of the Common Rail injection system in 1997 [62-65] higher injection pressures have been reached than the previous mechanical systems. The delivery of fuel into the cylinder at pressure up to 2000 bar strongly influences the way the fuel penetrates compared to previous developed models. The work of Siebers [14] can be considered as the main contribution to this topic. He presented a scaling law for the prediction of the liquid-phase fuel penetration in a diesel jet. Assuming the fully developed jet, the mass, momentum, and energy balances are solved across a control surface. The idealized spray is assumed to have a constant spreading angle; uniform velocity, temperature, and fuel concentration profiles (i.e., perfect mixing inside the spray boundaries); and no velocity slip between the injected fuel and the entrained ambient gas. The latter assumption is uncertain very close to the injector orifice but starts to be valid well before the region of complete fuel vaporization. In Figure 4.1, a representation of the spray according to Siebers is shown in comparison to the real image of the fuel jet experimentally obtained via visible imaging. Assuming that in x=L all the fuel is in the vapor-phase, L is the location of maximum liquid penetration.

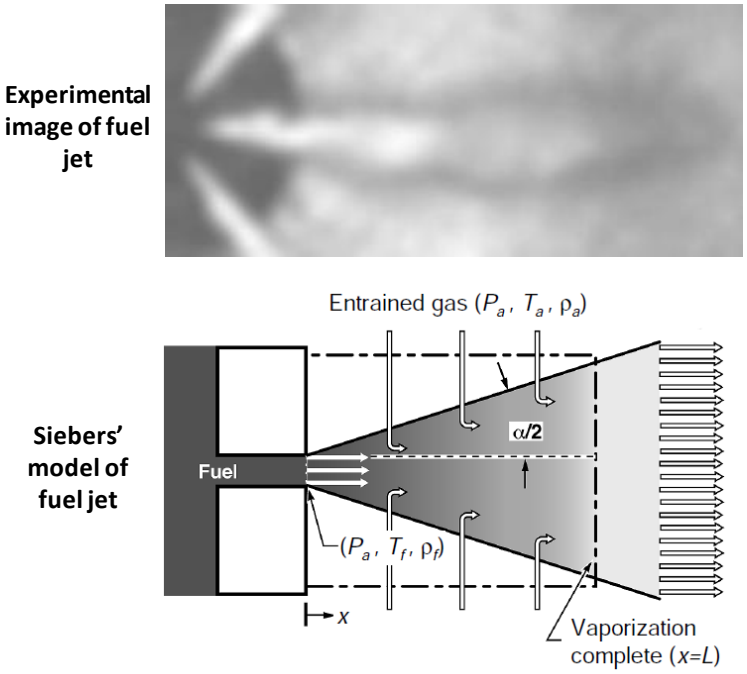

Figure 4.1: Experimental image of fuel jet and schematic of the Siebers' spray model [14].

At the axial location of L, the following thermodynamic assumption are made: the vapor phase fuel is at a saturated condition, the vapor fuel is in thermodynamic equilibrium with the entrained ambient gas and the liquid phase fuel, i.e. they all are at the same temperature, idealized phase equilibrium, the gas absorption in the liquid phase is neglected, the recovery of kinetic energy in the fuel vaporization region of the spray is neglected. No consideration is given to atomization processes or droplets. The transport rates between phases at droplet surfaces are fast relative to the transport rates as a result of the mixing processes in the spray [66]. The liquid length scaling law for diesel spray is obtained in three steps; the complete derivation of the law is reported in [14]. First, ratio (B) between the fuel and air mass flow is derived from the mass and energy equilibrium at the axial location x=L. The following identity:

$$B = \frac{Z_a(T_s, P_a - P_s) \cdot P_s \cdot M_f}{Z_f(T_s, P_s) \cdot [P_a - P_s] \cdot M_a} = \frac{h_a(T_a, P_a) - h_a(T_s, P_a - P_s)}{h_f(T_s) - h_f(T_f, P_a)} \qquad Eq.(4.1)$$

where:
B: ratio of fuel and the ambient gas mass flow rates required to vaporize the fuel,
$\mathbf{h_f}$ **,** $\mathbf{h_a}$: specific enthalpies of the fuel and ambient gas, respectively,
$\mathbf{T_f}$: injector tip temperature,
$\mathbf{P_a}$: ambient pressure,
$\mathbf{T_a}$: ambient temperature,
$\mathbf{P_s}$: partial pressure of the vapor fuel,
$\mathbf{T_s}$: saturation temperature,
$\mathbf{Z_f}$ **,** $\mathbf{Z_a}$: vaporized fuel and ambient gas compressibilities, respectively,
$\mathbf{M_f}$ **,** $\mathbf{M_a}$: fuel and ambient gas molecular weights, respectively.

Equation 4.1 can be solved iteratively to find the unknown Ts. Once determined Ts, B can be calculated as well as all the thermodynamic properties of fuel and ambient gas at the liquid length location.

The next step consists in finding the ratio between the fuel and air mass flow rate as function of the axial location. An additional assumption is made: the axial variation of this ratio in a vaporizing spray is similar to that in a non-vaporizing, isothermal spray. This implies that the droplets in the spray (non-vaporizing or vaporizing) are small enough that they follow the gas flow, or that the spray has locally homogeneous flow, as discussed in Kuo [66]. The assumption also implies that temperature effects do not significantly alter the mean fuel/ambient-gas ratio at any axial location in the spray. The relationship for the axial variation of the ratio of the fuel and ambient gas mass flow rates is the following:

$$\frac{\dot{m}_f(x)}{\dot{m}_a(x)} = \frac{2}{\sqrt{1 + 16 \cdot \tilde{x}^2} - 1} \qquad Eq.(4.2)$$

where:
$\dot{m}_f$, $\dot{m}_a$: fuel and ambient gas mass flow rates, respectively,
$\tilde{x}$: normalized axial location.

Finally, to get the liquid length scaling law for diesel spray, the term B, derived from equation 4.1, must be substituted in equation 4.2 and solve for $\tilde{x} = \tilde{L}$. The final equation in dimensional form is:

$$L = \frac{b}{a} \cdot \sqrt{\frac{\rho_f}{\rho_a}} \cdot \frac{\sqrt{C_a} \cdot d}{tan\left(\vartheta/2\right)} \cdot \sqrt{\left(\frac{2}{B(T_a, P_a, T_f)} + 1\right)^2 - 1} \qquad Eq.(4.3)$$

where:
ρ_f , ρ_a: density of fuel and ambient gas, respectively,
d: physical orifice diameter,
C_a: orifice coefficient of area-contraction,
θ: measured spray angle for a real spray,
a and **b:** constant.

In equation 4.3, the square-root term containing B accounts for the effects of parameters involved in the energy equation while the terms in front of the square-root term with B account for the effects of various parameters on the spray mass and momentum transport.

The Siebers' scaling law for diesel spray penetration has shown a good agreement with experimental measurements over a wide range of operating conditions [14, 15, 48]. The success of the Siebers' model indicates that the control volume analysis is able to captures the important physics affecting diesel jets. The reliability of this model has assured its wide use in the research field and has allowed to deep the understanding of diesel injection at high pressure. On the other hand, their solution treats the jet velocity at any axial location as invariant with time, like in a steady jet. Therefore, the dynamics of a jet with an unsteady injection rate cannot be predicted.

4.2 The 1d model proposed by Musculus and Kattke

To overcome the limitations of the Siebers' stationary model, Musculus and Kattke [15] proposed a mono-dimensional array of discrete control volumes in the axial direction of the jet, where mass and momentum transport are solved numerically for each control volume. A representation of the one-dimensional array of control volumes is reported in Figure 4.2. The jet radial extension is

determined using a constant spreading angle. The jet boundaries are defined as the radial position where the axial velocity is zero. This effectively corresponds to a position on a Gaussian error function fit to the axial velocity profile at 3% of the centerline value.

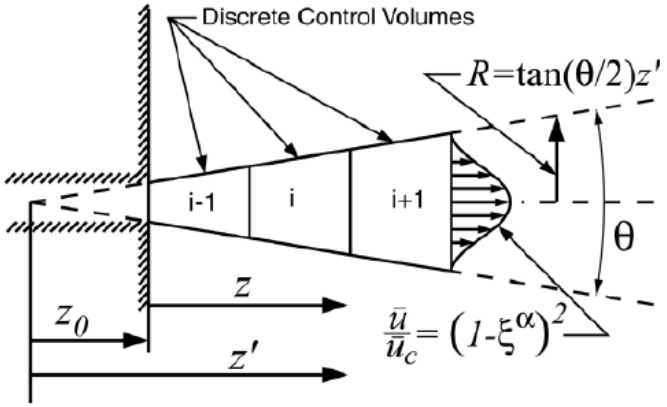

Figure 4.2: One-dimensional discrete control volume transient diesel jet model. Reproduced from [15].

In the model, the following assumptions are made: the jet is non-vaporizing as the effects of the evaporation process cannot be simulated in such a simple model. Even if the fuel is universally treated as liquid, the model can evaluate both the fuel liquid and vapor penetration assuming the hypothesis of mixing-limited vaporization [18]. The penetration of the liquid-phase is identified as the position from the nozzle where the fuel-to-air (F/A) ratio reaches the critical equivalence ratio for the thermodynamic equilibrium. The flow is incompressible; this hypothesis is well accepted for the regions downstream the jet where the compressibility effects are negligible. Turbulent and viscous forces acting on each control volume are neglected because they are very small compared to pressure forces. Only axial convection is considered in the transient momentum transport equation while the effects of molecular and turbulent diffusion are neglected. The net force due to any axial pressure gradient is assumed negligible. The jet spreading angle is treated as constant. Differently from Siebers' model, this one is able to simulate a variable rate-of-injection (ROI) with the typical ramp-up and ramp-down of the injection profile.

The transient transport equations for fuel mass m_f and axial momentum M in each control volume are the following:

$$\frac{\partial m_f}{\partial t} = \dot{m}_{f,in} - \dot{m}_{f,out} \qquad Eq.(4.4)$$

$$\frac{\partial M}{\partial t} = \dot{M}_{in} - \dot{M}_{out} \qquad Eq.(4.5)$$

The mass and momentum fluxes are considered across the upstream and downstream faces of each control volume. The integral fuel mass and momentum fluxes are written as:

$$\dot{m}_f = \rho_f \int \bar{X}_f \, \bar{u} \, dA \qquad Eq.(4.6)$$

$$\dot{M} = \int \bar{\rho} \, (\bar{u})^2 \, dA \qquad Eq.(4.7)$$

where,
$\boldsymbol{\rho_f}$**:** density of liquid fuel,
Ū: turbulent mean velocity,
$\boldsymbol{\bar{\rho}}$**:** turbulent mean density,
$\boldsymbol{\bar{X}_f}$**:** turbulent mean fuel volume fraction,
A : jet cross sectional area.

The turbulent mean velocity ū and fuel volume fraction $\bar{X}_f$ are non-uniform over the jet cross-section; they are assumed to vary according the Abramovich profile [67]. This results in higher values on the centerline and lower values on the jet contour.

$$\frac{\bar{X}_f}{\bar{X}_{f,c}} = (1 - \xi^{\alpha})^2 \qquad Eq.(4.8)$$

$$\frac{\bar{u}}{\bar{u}_c} = (1 - \xi^{\alpha})^2 \qquad Eq.(4.9)$$

The Musculus model, derived from the Siebers' one, has been developed to simulate the injection process in a constant volume combustion vessel. Its simplicity contributed to its wide spread in the combustion research context. The Musculus model has revealed reliable in the prediction of the jet behavior in a non-reacting environment [15, 68] and in a reacting ambient [56] in high-pressure combustion vessels; however it is of great interest to simulate the fuel injection in a system more similar to the real engine. For this reason, in this work it has been used as starting point for the development of a transient jet model in a light duty optical engine.

4.3 Validation, use, and implementation of Musculus and Kattke's model

In 2011, Pickett et al. [55] quantitatively measured the fuel-vapor concentration in evaporating diesel sprays in a high-pressure combustion vessel. The aim of their work was to identify the mixture fraction at the edge of the jet that corresponds to the spreading angle detected by Schlieren imaging. They also evaluated the accuracy of the mixing prediction for the variable-radial

profile model by Musculus and Kattke to determine if the assumption made to build up the model were justified. They observed that using measured penetration coupled with the variable profile model to predict mixing and spreading angle is more accurate and easier than using the model and Schlieren derived spreading angle to predict mixing and penetration. According to this description, this approach is called *penetration matching technique*.

By comparing the predicted local mixture fractions with Rayleigh scattering measurements, they assessed that the radial distribution used in the variable profile model is a reasonable representation of mixture fraction in a fully developed, vaporized diesel jet. Finally, they introduced the need to assume different spreading angle values in the near and in the far fields to match both the liquid penetration upstream and the mixture fraction downstream.

Nerva et al. [56], in 2012, studied the effects of biodiesel fueling on the combustion processes of a diesel engine. Experiments were conducted in an optically accessible, constant-volume vessel at ambient conditions representative of a modern diesel engine. The Musculus and Kattke jet model was used to model spray penetration with different assumptions for nozzle coefficients and spreading angle; these subtle variations produced predictions that fell within the experimental uncertainty. They concluded that the differences in penetration for biodiesel and diesel jets were not significant enough to ascertain a causal effect of either spreading angle or flow coefficients on the penetration. The similarity in penetration suggested a similar fuel mixture fraction distribution for diesel and biodiesel, which could be estimated using the 1d mixing model.

In the work of Pickett et al. [68] of 2013, the Musculus and Kattke's model predictions of penetration when using the recommended model ROI [69] were compared to the measured experimental data. Experiments were conducted in a combustion vessel. They pointed out a potential improvement to the Musculus and Kattke model consisting in implementing a variable spreading angle. The size and growth rate of each control volume in the model is indeed determined by user via the spreading angle value. The logical conclusion of the work of Pickett et al. [68] was that both a variable ROI and a variable spreading angle were required in order to represent the correct physics of the spray penetration.

Recently, in 2015 Tauzia et al. [70] set up a 1d combustion model derived from the transient 1D spray model of Musculus and Kattke. The original model was modified in order to take into account fuel vaporization and combustion. They compared the model results to several experiments from the Engine Combustion Network (ECN) database [71] on inert and reacting Diesel spray measured in a constant volume bomb. The qualitative agreement with calculations

was good, while quantitative discrepancies sometimes appeared. They pointed out some improvement to include in the model. For example, a better estimation of spray angle with variations over time and/or distance from the injector. The dilatation estimation could also be improved, and a description of radial composition and temperature profiles could be implemented.

Regarding model application, their future purpose is to pass from a constant volume bomb to an engine-like environment by taking into account a variable volume combustion chamber and the spray/wall interaction. Finally, their intent is to use the model to simulate multiple injections too.

4.4 Model limitations and implementations to simulate engine environment

As seen in the previous paragraph, the Musculus and Kattke's model has had large diffusion over the engine research panorama. So far, its application is confined to the original environment it has been developed for, that is the constant-volume vessel. Conversely, the main objective of this work is to use the model for the simulation of the injection process in an optical engine.

To this purpose, all the assumptions made above have been made. n-Dodecane tables have been used in the model to calculate the equivalence ratio in saturated conditions. The air motion (swirl, tumble) inside the cylinder has been neglected because it is in author's experience that the air motion does not affect much the liquid fuel penetration because it is the bowl wall that plays the main role. For the application of the 1d model in the optical engine some modifications have been necessary in order to simulate the new testing environment. The model has been originally developed for a constant volume combustion vessel where the jet was not limited by the vessel wall. On the contrary, the space inside the combustion chamber is very limited and it is common that the jet is affected by the bowl wall and interacts with it. For these reasons, the boundary conditions of the model have been modified including the combustion chamber limits to simulate the presence of the bowl wall. Taking into account the injector and the piston geometries, the correct distance between each injector hole and the wall is 22.88 mm. To simulate the fuel impact on the chamber wall, additional boundary conditions have been considered: in the last element of the domain, the flow is set equal to zero to prevent that the mass moves outside of the domain. This is obtained by forcing the velocity and the momentum to be null in the last element. In this location, a fuel accumulation is produced according to the mass flow outside from the second-last element, and the mass and the static pressure increase. Obviously, the last element has a finite volume and then it can contain a limited fuel amount. Once all the available volume is filled with fuel, the mass excess in the last element is rebounded back to the second-last element where it

accumulates again. This kind of modeling simulates a layer-by-layer fuel deposit on the chamber wall. The fuel mass in these layers corresponds to the fuel quantity that impinges the wall.

A further modification of the original model concerned the identification of two jet penetration curves corresponding to the jet tip, downstream, and the jet body, upstream. As stated before, the model uses the equivalence ratio along the jet axis to detect the maximum liquid penetration. Due to the formation of a local peak on the jet tip, two separated liquid region are identified by the model. This break in of the liquid phase is predicted but not observed in the experimental images. According to Pastor et al. [57], this behavior is typical of ROI with a ramped-up profile and it can be ascribed to the simplifications used in the model regarding the diffusive nature of the transient liquid jet tip. In this case, the model assumes that, during the injection ramp-up, the freshly injected fuel has higher velocity than the previously delivered one, and then the fuel accumulates on the tip. In the present work, the model has been modified in order to take into account the penetrations of both the body and the detached tip of the jet. The penetration of the jet body has been used for the comparison with the experimental measurements. Figure 4.3 clarifies the concept of jet body and detached jet tip. In the figure, the jet is moving from the left (nozzle position) to the right. The chamber wall location is indicated with a dotted line. The dashed blue edges correspond to the liquid jet contour. At this time, there are two separated liquid regions. On the left, there is the fuel that comes out of the nozzle, it is the jet body, and on the right there is the jet tip that separated from the body and now lies on the chamber wall.

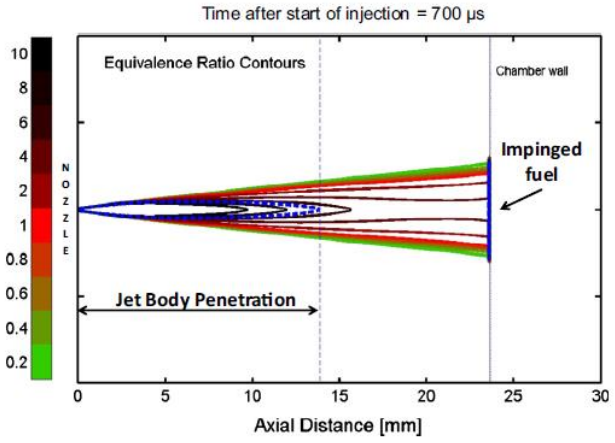

Figure 4.3: Predicted 2D contour plot of the equivalence ratio at 0.7 ms ASOI with wall.

Finally, a further implementation has been necessary to simulate carefully the in-cylinder conditions. As aforementioned, the model was developed in a constant volume environment, therefore, volume variations are not supposed to be. On the contrary, the peculiarity of

alternative engine is to realize the pressure increase by means of volume variations. Of course the volume variation due to the piston movement does not affect the simulation domain considered in the model. The volume variation produces variable pressure, temperature, and density values inside the cylinder. To take into account the variation of these thermodynamic properties, the experimentally measured signals of pressure and volume have been used, while the temperature and the density have been theoretically derived using the perfect gas model. These values have been given to the model in order to update the thermodynamic conditions at each temporal step of the simulation.

Finally, concerning the jet spreading angle, a constant one is assumed in the original model. This assumption has been taken for the prediction of the liquid phase penetration. However, when vapor phase penetration is considered, the need for two values of cone angles has arisen according to the work of Pickett [68]. A smaller angle is assumed in the near field of the jet while a larger one in the far field. Based on this, two regions of the spray with two different angles have to be considered. The distance from the nozzle where the cone angle value changes, is not defined [68]; however, they noted that the start of vaporization at the edges of liquid jet affected the measurements. Therefore, in the present work, the distance of maximum liquid penetration has been chosen to separate the two regions.

Chapter 5

Experimental Setup and Methods

5 Experimental Setup and Methods

5.1 Optical engine

The experimental activities have been run in the laboratories of the Istituto Motori - CNR of Napoli. In particular, the experiments have been performed in the “optical diagnostics laboratory” shown in the photograph of figure 5.1.

Figure 5.1: Photograph of the “Optical Diagnostics Laboratory” at Istituto Motori - CNR.

The laboratory hosts three engines, a SI engine with 4 optically accessible cylinders, a 3 cylinders CI metal engine, and a CI single cylinder optical engine. Optical measurements have been performed in the last one. This has been equipped with the combustion system architecture and injection system of a four-cylinder standard engine. The engine and the injection system specifications are reported in Table 5.1. To get the optical access from beneath the combustion chamber, an extended piston has been mounted. The piston crown is provided with a sapphire window of 46 mm diameter (Figure 5.2). The window was made of sapphire to minimize the heat release differences between metal and optical engine [72]. The bottom of the combustion bowl was flat; nevertheless its volume and the wall shape were similar to that of the standard engine by reducing the bowl bottom distance. The view of the combustion bowl is provided by a 45° inclined visible-IR mirror placed inside the extended piston.

Table 5.1: Engine and injection system specifications.

Engine type	4-stroke single cylinder
Bore	8.5 cm
Stroke	9.2 cm
Swept volume	522 cm^3
Combustion bowl	19.7 cm^3
Vol. compression ratio	16.5:1
Injection system	Common Rail
Injector type	Solenoid driven
Number of holes	7
Spreading angle of fuel jet axis	148°
Hole diameter	140 µm
Rated flow @ 100bar	440 cm^3/30s

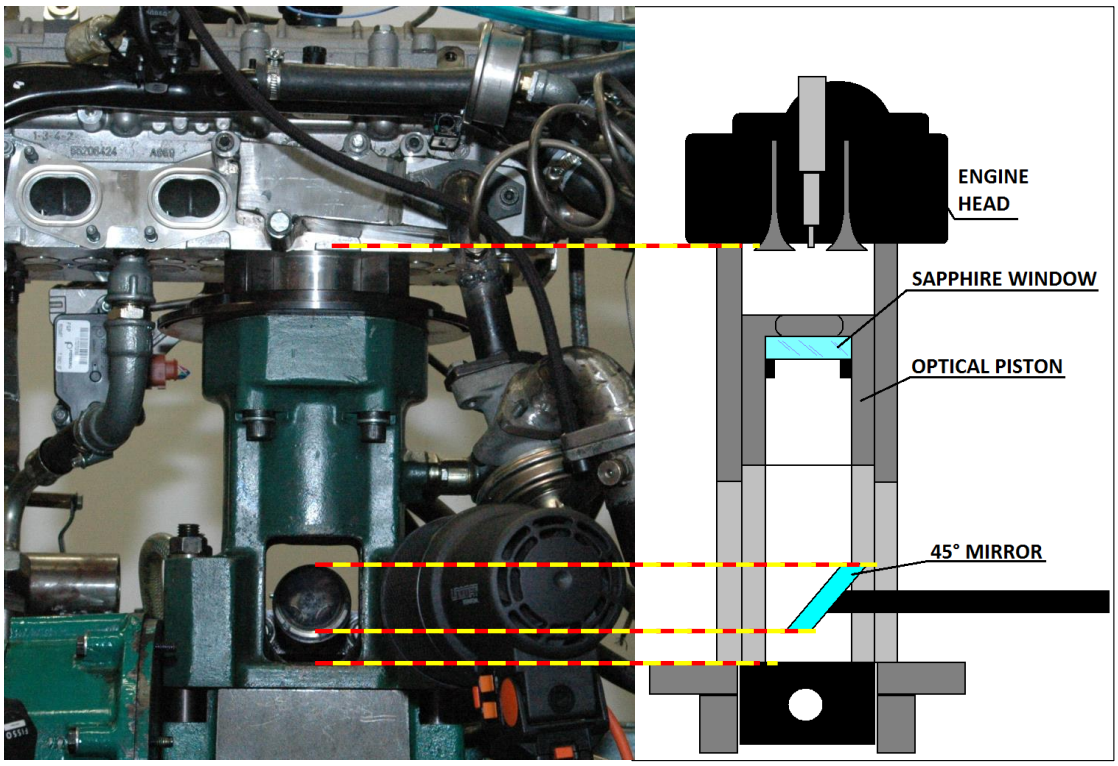

Figure 5.2: Picture from front (left) and scheme from lateral (right) view of the elongated optical piston.

Figure 5.3 depicts a scheme of the air management system. An external air compressor has been used to supply pressurized intake air that has been filtered and dehumidified in order to make reliable the measure of the air mass flow. The air was heated up to a desired inlet temperature to compensate for the low compression ratio, typical of optical engine [73].

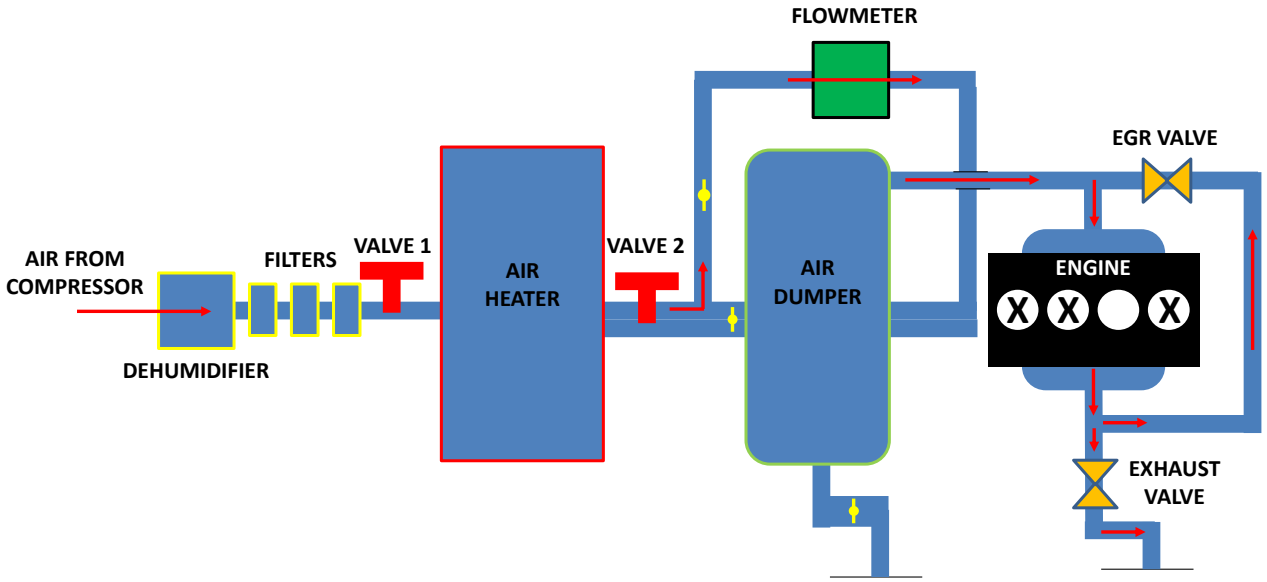

Figure 5.3: Scheme of the air management system.

The temperature and pressure values have been monitored by applying thermocouples and pressure sensors, respectively, to both the intake and exhaust lines. The engine was equipped with a Common Rail injection system managed by a fully opened electronic control unit (ECU). The ECU controlled the number of injections per cycle, the injection pressure, the injection start, the energizing time of the injector as well as the dwell time between two consecutive injections. A solenoid driven injector has been used, the specifications of the injection system have been reported in Table 5.1. A Hall-effect sensor has been applied to the line of the injector solenoid to monitor and analyze the current profile. Moreover, to record the in-cylinder pressure, a piezoelectric pressure transducer (AVL GH13P) has been set in the glow plug seat of the engine head. Injection and in-cylinder pressure signals have been monitored by means of INDIMODUL® by AVL, a multichannel acquisition system with 8 channels and an acquisition frequency up to 1MHz; the signals have been digitalized and recorded at 0.5°crank angle (CA) increments. The engine has been run in continuous fired mode and the average in-cylinder pressure has been measured from 200 consecutive combustion cycles. The heat release rate has been calculated from the ensemble averaged pressure data using the first law of thermodynamics and the perfect gas model [2].

5.2 Optical setup

In order to detect images of the combustion chamber in the visible and infrared spectra a charge coupled device (CCD) camera and an infrared camera have been used. A scheme of the optical setup for both the configuration has been reported in figure 5.4. The CCD camera used for visible imaging is the PixelFlyVGA COLOR by PCO; it has 640 x 480 pixels and a high sensitivity over a wide

visible range (400-750 nm). It has been equipped with the visible lens Nikkor 55 mm f/3.5. The resolution of the images is 10 pixel/mm. Two halogen continuous lamps have been used to light the jets in the bowl via the 45° mirror (Figure 5.4). The acquisition was not in cycle resolved mode but images have been recorded from separate cycles. In order to carry out a statistical analysis, 5 repetitions have been recorded and elaborated. The number of repetitions was limited by the fouling of the sapphire window. The images have been recorded with an exposure time that corresponded to 0.5°CA of the engine shaft for each tested speed.

IR imaging has been performed using the SC6800 fast IR camera by FLIR. It has a resolution of 640x420 pixels and a sensitivity range of 1.5-5 µm. The sensor is made of Indium Antimonide and it was equipped with a 100 mm lens. The image resolution is 9 pixel/mm. Images from IR camera have been detected with an exposure time of 10 µs. As for the CCD camera, one image per cycle has been recorded; the temporal resolution is of 0.5°CA of the engine shaft. The synchronization of the two cameras to the engine has been obtained by a delay unit which shifts the TDC signal coming from the engine shaft encoder.

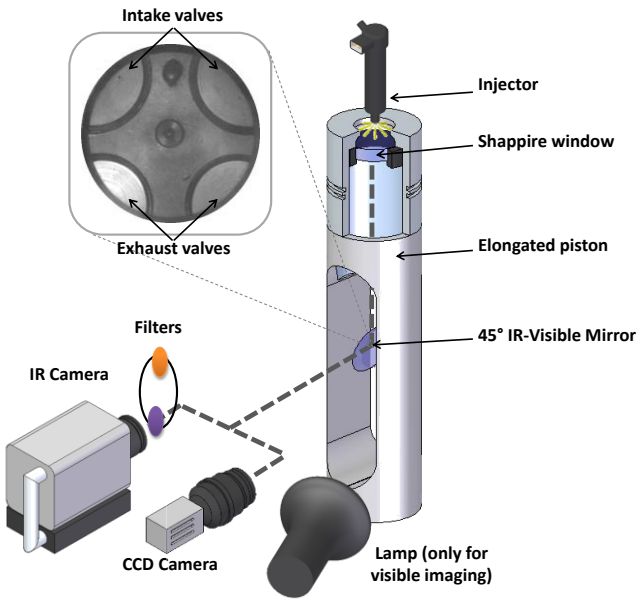

Figure 5.4: Scheme of the optical set up for visible and infrared imaging. The cameras are not used simultaneously.

5.2.1 Infrared wavelengths for combustion analysis

The spectral range of the IR cameras is quite wide (1.5-5 µm). As shown in figure 5.5, several species related to the combustion process emit in this band, e.g. CO, CO_2, NO, CH_4, H_2CO, H_2O [74]. One acquisition in the full camera range has been performed in order to get an overview of the radiations coming from the combustion chamber. Due to the great amount of collected energy, it has been necessary to use a Neutral Density filter with 10% attenuation (ND1) to prevent the saturation of the detected images. In the present work, different infrared wavelengths have been

investigated according to the target species. The first is the wavelength 3900 nm (bandwidth of ± 150 nm). From the chemical point of view, this wavelength is not characteristic of any species of those reported in figure 5.5; however, it is affected by the presence of other species with a broad signal centered around 3900 nm. For example, the range 3030-4000 nm is where acid OH emits (center at 3300 nm). The OH peaks due to carboxylic acids (COOH) show a very broad and less intense peak between 2850 and 4000 nm. The alkyl C-H has a peak between 3300 and 3580. And the aldehyde C-H has two medium intensity peaks on the right hand shoulder of the alkyl C-H's (3500 and 3600 nm) [74]. Hence, the band pass filter at 3900 nm has been used to visualize hydrocarbons and the intermediate products of the combustion reactions. In particular, during the injection process, a strong correlation between the signal at this wavelength and the liquid fuel detected with the visible camera has been found. Concerning the analysis of the fuel vapor phase, the contributions of Tomita et al. [75] and Klingbeil et al. [76] were fundamental. According to them, a strong hydrocarbon absorption band can be identified at wavelengths between 3300 nm and 3500 nm and it is associated with vibrational transitions of the C-H bond stretch. Here, the emission strength of the C-H stretch is supposed to vary almost linearly with the number of CH_2 groups [75]. Moreover, between 3300 nm and 3500 nm , the wavelength at 3400 nm seems to be well isolated from most other emitting species [77]. This wavelength has been investigated by Eagle et al. [46] to perform measurements of n-dodecane vapor penetration in a heavy-duty diesel engine. According to previous studies [12, 46, 75, 76], in this work, a second infrared wavelength has been investigated, it is at 3400 nm with a bandwidth ± 150 nm.

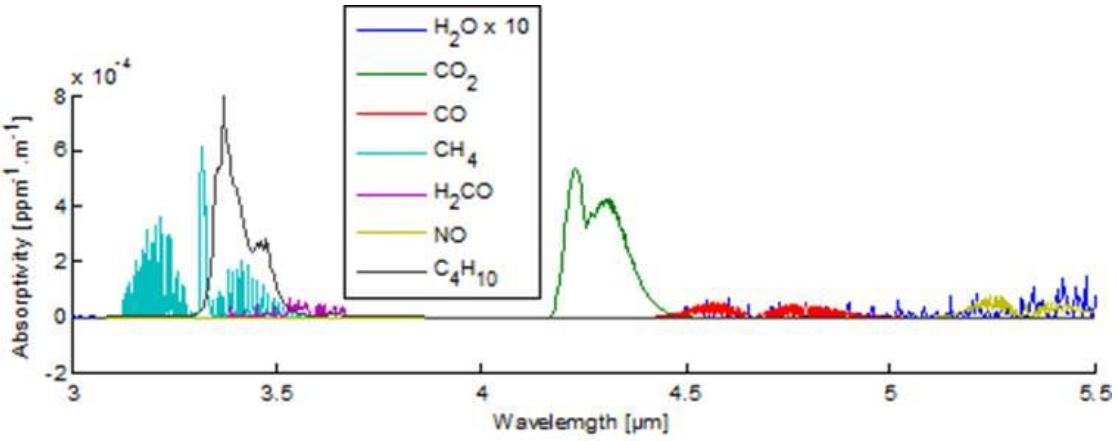

Figure 5.5: Absorptivity spectrum in the Mid-IR of the most significant species involved in the combustion process.

5.3 Measurements of fuel injection rate

The experimental rate of injection (ROI) indicates the rate of fuel delivery from the injector holes into the cylinder. This is an input required by the model to reproduce fuel injection process. Fuel injection rates have been measured by an AVL meter working on the “Bosch pipeline” principle [78]. This has been mounted close to the engine and the same fuel delivery line has been used in order to preserve the original configuration of the injection system. The injector temperature has been controlled by means of a thermocouple in the injector body and it has been set to 90°C. The pressure variations in the system measurement chamber have been registered by a GM12D – AVL piezoquartz transducer. The time resolution of the measurement was less than 1 µs. The signal has been converted to fuel mass flow taking into account the geometrical parameters of the device and chemical-physical properties of the fluid. The total injected fuel mass has been derived from the rate of injection curves. The values have been averaged on 4 subsequent tests of 300 repetitions each one. The coefficient of variation (CV) for each test was lower than 2.5%. Finally, the measured injected fuel has been compared to the one weighted by means of a precision balance at the system discharge and the two measurements were in line.

5.4 Measurements of the exhaust particulate matter

The combination of in-cylinder visualizations and engine exhaust emissions is very useful to understand the combustion process and the formation of pollutant emissions. The particulate matter is one of the major pollutant emissions of diesel engines. Hence, its concentration at the exhaust of the optical engine has been measured in order to support and interpret optical diagnostics results.

An AVL Smoke Meter 415SE has been used for the measurements; it uses the filter paper method to determine the soot concentration in the exhaust of line of the engine. A defined volume is sampled from the engine exhaust pipe and passed through clean filter paper inside the device. The filtered soot causes blackening of the filter paper, which is measured by a photoelectric measuring head and the result is analyzed by a microprocessor. The determined value is the Filter Smoke Number (FSN). Some characteristics of the device are reported in Table 5.2. The measurements of the others exhaust emissions have been made by Horiba MEXA 7100 DEGR analyzers whose main specifications are reported in Table 5.3.

Table 5.2: AVL smokemeter features.

Measurement principle:	Measurement of filter paper blackening
Measured value output:	FSN (filter smoke number) or mg/m³ (soot concentration)
Measurement range:	0 to 10 FSN
Detection limit:	0.002 FSN or ~ 0.02 mg/m³
Resolution:	0.001 FSN or 0.01 mg/m³
Exhaust pressure ranges:	-100 to 400 mbars
Maximum exhaust temperature:	600 °C
Repeatability:	Standard deviation 1σ ≤ ± (0.005 FSN + 3 % of the measured value @ 10sec intake time)

Table 5.3: Horiba MEXA 7100 DEGR specification [79].

Pollutant	Measurement technique	Range	Repeatability
CO	Non Dispersive Infrared	min 0-5000 ppm max 0-12 %vol.	<0.5% FS
CO_2	Non Dispersive Infrared	0-20 %vol.	<0.5% FS
HC	Flame Ionization Detector	min 0-500 ppm C max 0-50000 ppm	<0.5% FS
NO/NOx	Chemiluminescence	min 0-500 ppm max 0-10000 ppm	<0.5% FS

Non-dispersive infrared (NDIR) analyzers are used to measure the concentrations of CO and CO_2. Their principle of operation is based on the absorption of infrared radiation by these gases. For example, CO absorbs at about 4.6 μm whereas CO_2 absorbs at about 4.2 μm. The amount of radiation absorbed, *a*, is given by Beer's law [11]:

$$a_\lambda = 1 - \exp(-C_i Q_\lambda L) \qquad Eq.(5.1)$$

where:

C_i is the concentration of the species *i*;

Q_λ is the absorption efficiency;

L is the optical path length.

Therefore, the NDIR analyzer works by passing a pulsed beam of infrared light through a chamber containing the sampled gas. The amount of light absorbed by the measured gas is detected and is converted into an electrical signal. The electrical signal then is scaled to provide the concentration of the measured gas. The technique for HC measurement is the flame ionization detector (FID). A sample of exhaust gas is passed through a hydrogen flame that burns any HC present in the sample gas. An electrical current is passed across the flame and it changes in proportion to the

amount of HC [80]. Chemiluminescence analyzers were used to measure the NOx. They measure the NO by detecting the light emitted when it reacts with ozone (O_3):

$$NO + O_3 \Longrightarrow NO_2^* + O_2 \Longrightarrow NO_2 + O_2 + hv \qquad Eq.(5.2)$$

The intensity of the light, *hv*, proportional to the amount of NO in the sample gas, is measured and converted to an electrical signal. Other oxides of nitrogen are measured by passing them through a converter located before the reaction chamber that changes any NO_2, NO_3, and so forth into NO [11].

5.5 Engine operating conditions

The engine operating conditions investigated in this work were representative of the engine behavior when installed on a D-class vehicle during New European Driving Cycle (NEDC). They corresponded to seven operating conditions with different engine speeds and brake mean effective pressure (BMEP). The format in the text to indicate the operating points will be the following: ''rpmxBMEP'', hence the seven operating points are the following: 1000x0, 1500x2, 1500x5, 2000x2, 2000x5, 2000x10, 2500x8. A collection of engine load/speed values recorded during the NEDC has been reported in Figure 5.6.

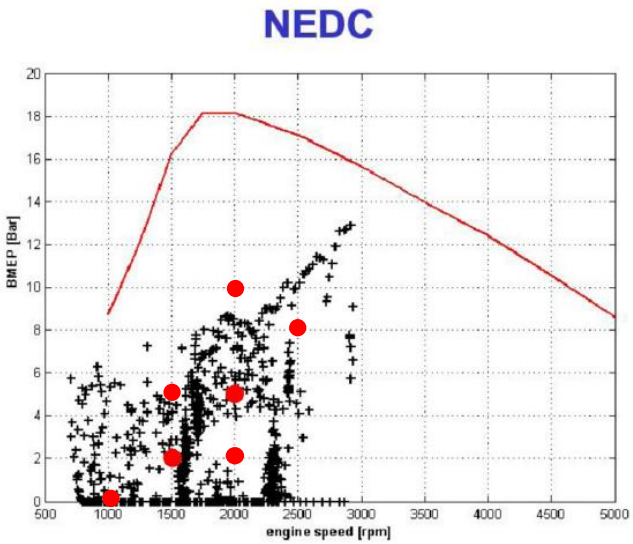

Figure 5.6: Load-speed diagram of the NEDC. The red line is the engine operating limit. The red dots correspond to the seven investigated engine conditions.

The engine operating conditions selected for this work correspond to the red dots. Commercial Diesel fuel has been used to feed the engine; the fuel properties have been reported in Table 5.4. The injection strategies consisted of two events per cycle, the pilot and the main; the injection strategies, in terms of timing, duration, and injection pressure, and the measured injected fuel

mass for each engine point have been reported in Table 5.5. All the data presented were taken with the engine operating in continuous mode. Then, true recirculation of exhaust gases (EGR) was performed using the hot gases of each combustion cycle. The EGR is used in order to reduce the emission of nitrogen oxides (NOx); values used for each engine operating point have been reported in Table 5.6. In motored conditions, temperature and density at Top Dead Center (TDC) were estimated assuming a polytrophic compression. The pressure at the bottom dead center (BDC) was assumed equal to the intake manifold pressure and the coefficient of the polytrophic was set to 1.36 [2]. This value was chosen after a validation procedure considering a sample of motored data at different intake pressures and engine speeds. Starting from the intake pressure, the pressure at the TDC was calculated using the polytrophic transformation. The calculated value was compared to the one measured by the pressure transducer. Using the exponent 1.36, errors were inside the range ±3%. Since no significant differences among the calculated Rate Of Heat Release (ROHR) curves were observed across the TDC when lower values of the polytrophic exponent were used, the value 1.36 was adopted for the calculation of the temperature and density at the TDC. Finally, a swirl motion is given to the intake flow by using a set of adjustable plates at the entering of one of the two intake ducts. The relative position of the swirl plates, the absolute intake air pressure, the ambient temperature and density at the TDC in motored conditions have been reported in Table 5.6.

Table 5.4: Properties of Italian commercial Diesel fuel.

Feature / Method		**Units**	**Value**
Density @ 15°C (EN ISO 12185)		[kg/m^3]	829
Cetane Number (EN ISO 5165)		[-]	51.8
Low Heating Value (ASTM D3338)		[MJ/kg]	42.4
Flash point (ASTM D93/IP 34/ EN ISO 2719)		[°C]	72
Kinematic viscosity @ 40°C (ASTM D445)		[mm^2/s]	2.7
Cloud point (ASTM D2500)		[°C]	-2.2
Lubricity 60°C (ISO 12156-1)		[µm]	382
Distillation (ASTM D86)	IBP	[°C]	159
	10% vol.	[°C]	194
	50% vol.	[°C]	268
	90% vol.	[°C]	333
	95% vol.	[°C]	350
	FBP	[°C]	361
Carbon (ASTM 5991)		[mol%]	~85.5
Hydrogen (ASTM 5991)		[mol%]	~13.5
Oxygen (ASTM 5991)		[mol%]	~1.4

Table 5.5: ***Engine operating conditions - Injection Parameters.***

Name	Speed	BMEP	SOI pilot	ET pilot	Inj. Quantity pilot	SOI main	ET main	Inj. Quantity main	Inj. pressure
	[rpm]	[bar]	[°]	[µs]	[mg/str]	[°]	[µs]	[mg/str]	[bar]
1000x0	1000	0	-13.4	420	0.8	-3.7	519	2	304
1500x2	1500	2	-16	290	0.7	-6	545	5.9	615
1500x5	1500	5	-11.6	269	0.8	0.3	570	13	867
2000x2	2000	2	-21.2	282	0.7	-8	520	6.1	700
2000x5	2000	5	-18.6	257	0.8	-2.4	560	13.3	891
2000x10	2000	10	-18.1	215	0.5	-5.7	632	21.8	1230
2500x8	2500	8	-21.7	215	0.4	-6.2	575	17.4	1334

Table 5.6: Engine operating conditions - Air ***Parameters*****.**

Name	Speed	BMEP	Intake air	EGR	Absolute intake pressure	Temperature @ TDC	Density @ TDC	Swirl
	[rpm]	[bar]	[kg/h]	[%]	[bar]	[K]	[kg/m^3]	[%]
1000x0	1000	0	8.8	61	1.25	803	16	75
1500x2	1500	2	15	58	1.32	834	18	66
1500x5	1500	5	22.8	39	1.36	818	20	61
2000x2	2000	2	20.7	48	1.22	811	19	60
2000x5	2000	5	34.2	29	1.39	824	22	58
2000x10	2000	10	45.2	25	1.74	829	29	42
2500x8	2500	8	52.1	24	1.71	839	27	40

5.6 Measurements of the jet parameters from image processing

The detection of the liquid penetration from visible images is made using an automatic segmentation process implemented in Matlab® and shown in figure 5.7. The image to process (with jets) is compared to the background (without jets) which was recorded before the start of injection. The background subtraction is useful to highlight the jet contour. A threshold is applied to the resulting image to detect the jets contour. A constant threshold has been used for visible images; while a variable threshold that depends on the pixel maximum value has been used for IR images because of the sharp increase of image intensity as the injection takes place. The

application of the threshold returns a binary image. The noise and the outliers are then removed and the shape of the seven jets is obtained. The last picture of figure 5.7 shows the overlay of the jets contours (yellow) on the original image. The jets have been detected with a good approximation.

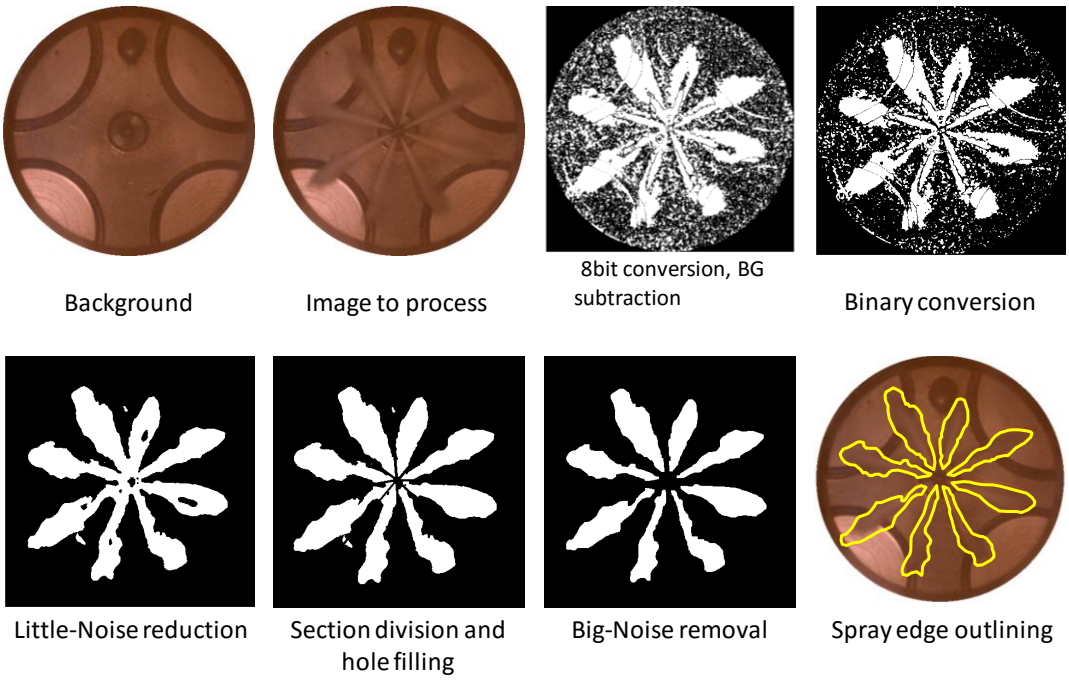

Figure 5.7: Sequence of pictures during the image processing .

From the detected jets contours, the jet global quantities as the penetration and the cone angle have been evaluated using the Naber and Siebers' [18] iterative procedure (figure 5.8). According to them, the values of penetration and cone angle depend on each other; starting from an initial value of cone angle (θ), the penetration is found as the median of the distance from the injector tip of all the pixel of the jet contour contained within an arc of θ/2. Then, the cone angle θ is calculated by the isosceles triangle of height S/2 and area A, using the following equation:

$$tan\left(\frac{\theta}{2}\right) = \frac{A}{(S/2)^2} \qquad Eq.(5.1)$$

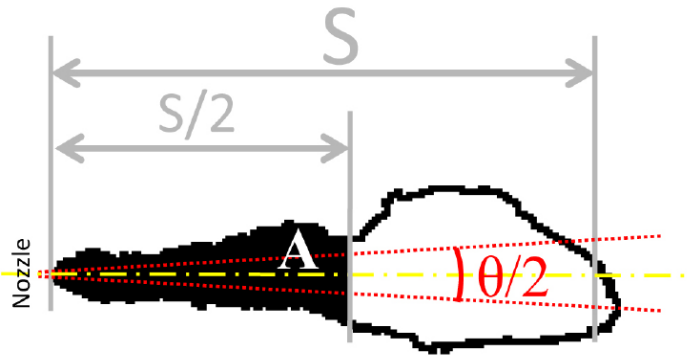

Figure 5.8: Definition of jet penetration and cone angle [18].

5.7 Uncertainty analysis

In any experiment, errors and uncertainties can arise from instrument selection, condition, calibration, environment, observation reading and test procedures. Uncertainty analysis is needed to prove the accuracy of the experiments [81]**.** Standard deviation is a statistical indicator to take into account measurements variation. The error is thus derived using the standard deviation from the average value. The experimental results shown throughout this work have been detected for five repetitions and then the average value has been displayed with error bars of ± standard deviation of the data sample.

Chapter 6

Experimental Results

6 Experimental Results

6.1 In-cylinder measurements

The most direct way to follow the combustion evolution in an ICE is to monitor its macroscopic parameters. The in-cylinder pressure is the most important variable to be measured in order to get information on the combustion process. The rate of heat release (ROHR) can be derived from the pressure trace and the volume variation [2]; it gives an idea of the rate of the reactions. More details about the calculation of the ROHR are reported in the Appendix A. Another significant signal to monitor is the current to the solenoid of the injector that shows the start and the duration of both the injections. The pressure trace, the ROHR, and the drive current to the injector to the solenoid injector are reported in figure 6.1. Data of the original metal engine are also shown as reference because it is important that the optical engine reproduces the same combustion evolution of the metal one. This is mandatory to validate the optical analysis. As shown in figure 6.1, the match between optical and metal engine data has been reached for all the conditions. Generally, the optical engine has higher pressure during the compression stroke. This is due to the higher intake pressure adopted to compensate for the blow-by losses of the optical engine. The major aim was to reach the same pressure at the top dead center, which has been made in almost all the conditions. Different comments must be made for the peak pressure. It is expected to see lower pressure for the optical engine because it depends on the compression ratio. Finally, the data of optical and metal engines are aligned during the expansion stroke. As aforementioned, the ROHR indicates how fast the reactions are occurring. The combustion reactions have been well reproduced in the research engine. The main differences concern the weaker pilot combustion, as in the conditions 1000x0, 1500x2, and 2000x2, and the lower peak of heat release, at 1500x5.

The current signals perfectly overlay for the two engines because they are electronically set.

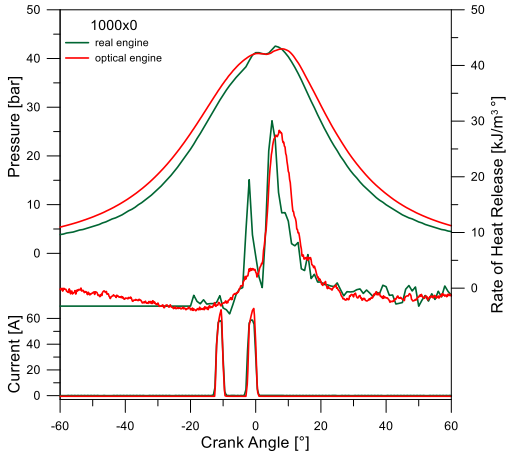

Figure 6.1: In-cylinder pressure, rate of heat release, and drive current to the injector in the operating conditions 1000x0, 1500x2, 1500x5, 2000x2, 2000x5, 2000x10, and 2500x8.

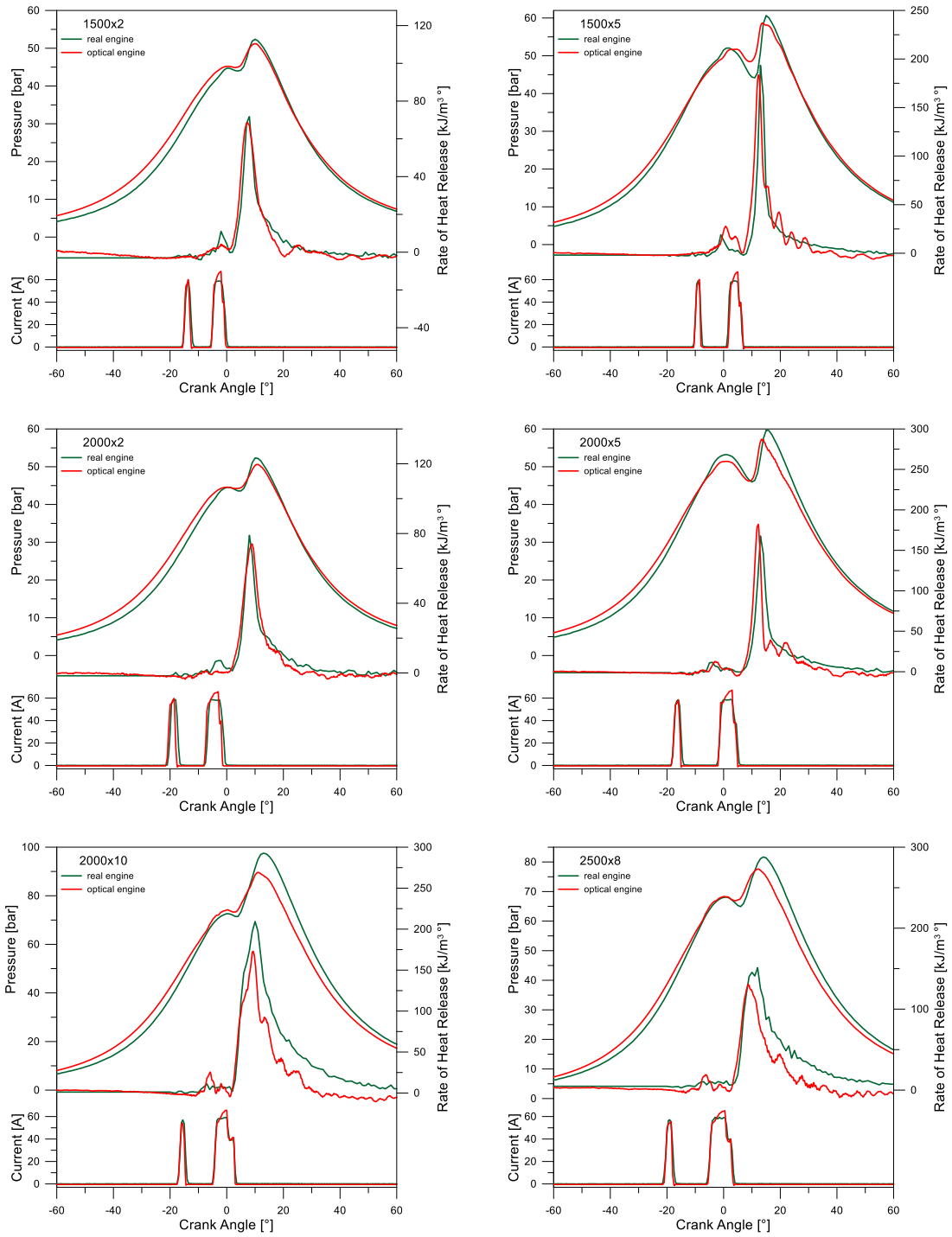

Figure 6.2 continue: In-cylinder pressure, rate of heat release, and drive current to the injector in the operating conditions 1000x0, 1500x2, 1500x5, 2000x2, 2000x5, 2000x10, and 2500x8.

6.2 Analysis of the fuel liquid phase

Figure 6.2 shows a collection of images of the pilot and main injections for all investigated conditions. A few characteristics crank angles have been chosen for each operating points to give an idea of the general evolution of the jets in the combustion chamber. It is important to note that imaging in the visible range can detect only the liquid phase. Hence, the jets disappear from the

image as the evaporation process takes place and no information about the vapor phase distribution is available.

The pilot injection has the role to prepare the combustion chamber to the combustion event. It is very short in time and a small quantity of fuel is injected. For this reason only a few images are available. At the start of injection, first column in figure 6.2, the fuel is going out of the injector nozzle and small jets are hardly detectable in almost all the cases. Then the fuel spreads until it evaporates and is no longer detectable using this technique. A few crank angles after the pilot injection, depending on the engine operating point, there is the main injection. Its role is to provide the fuel needed to get the desired output power. It has longer duration and injected quantity. It is detectable in the liquid phase for a longer time and can reach longer jet penetration in the combustion chamber. High penetrations are good for the air/fuel mixing but if too long the jet can reach the chamber wall giving place to the wall impingement. This produces fuel rich zones that burn in lack of oxygen so generating carbonaceous particles and lowering the combustion efficiency. Visible imaging does not give evidences of the fuel impingement on the chamber wall; however, this is likely due to the limits of this technique rather than to the absence of fuel/wall interactions. When the jet is completely developed, last and second last columns in figure 6.2, the jet tip appears not well defined and affected by fluctuations. This is due to the evaporation process on the jet tip and boundaries that is where the interaction with the air is more efficient. In the images, the jet contour appears darker than the jet core because it reflects less light. From the start of injection up to the end of the visualization, the jet keeps attached to the nozzle forming a single body.

Generally, the combustion starts after the end of the main injection; the flamelets in the figure are due to the combustion of the previous pilot injection that has had enough time to evaporate, mix with the air and react.

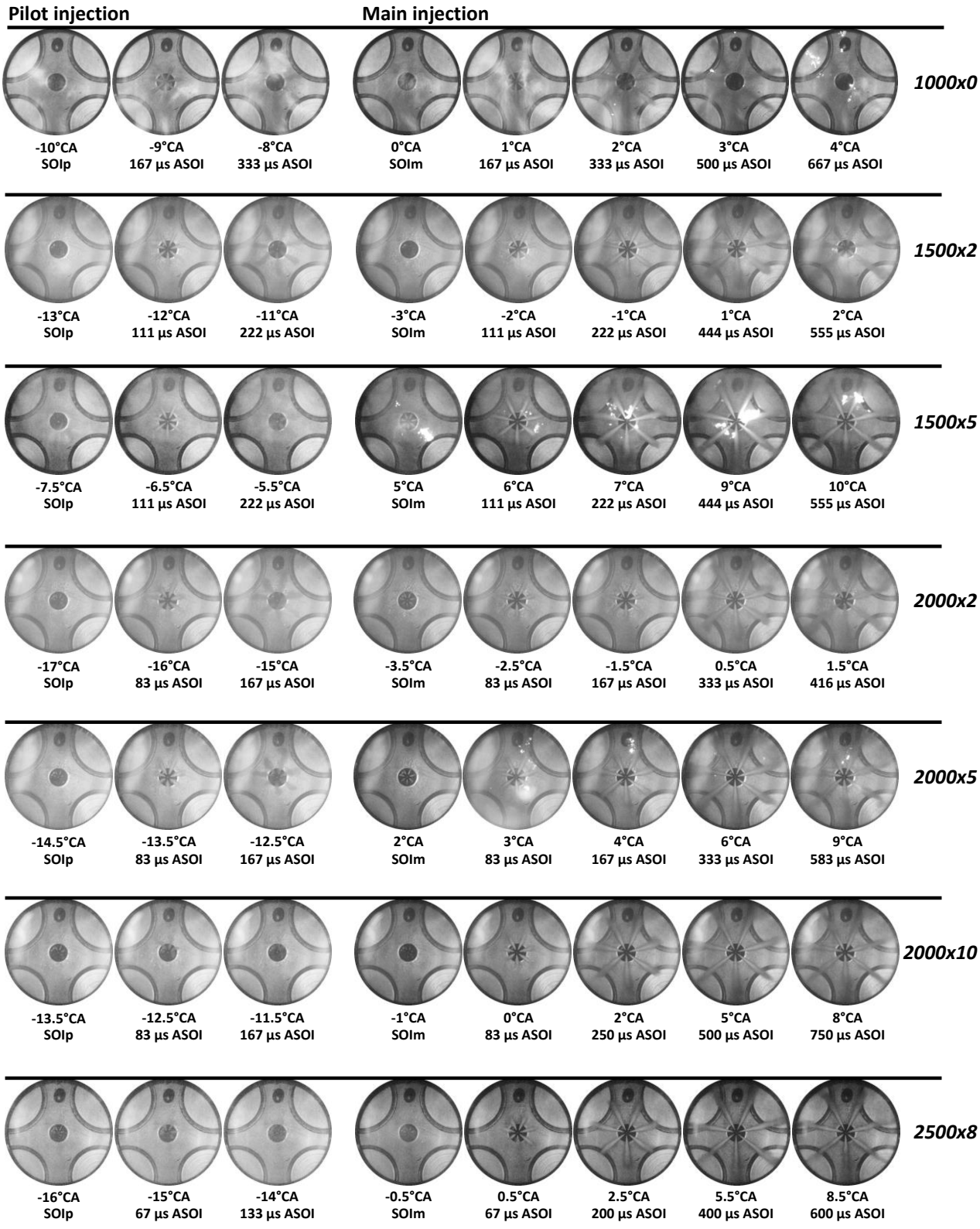

Figure 6.3: A collection of images of both the pilot and main injections for all investigated operating points.

The jet global quantities as penetration and cone angle have been measured from the images using the procedure illustrated in paragraph 5.6. The curves of jet penetration and cone angle for both pilot and main injection versus crank angle have been reported in figures 6.3 and 6.4. The

phasing of the two injections depends on the engine operating points; it can be noted that different start of injection and dwell time (time between injections) are needed as speed and load change. Pilot injection is characterized by lower maximum penetration and shorter duration while the main injection penetrates farther in the combustion chamber. As aforementioned, there is no evidence of wall impingement when visible images are elaborated. Only a rising phase of the penetration can be observed for the pilot injection, while a rising and a subsequent stabilization phase has been observed for the main injection. In addition, the jet recession has been detected in some cases (1500x5, 2000x5, 2000x10, and 2500x8). This is due to the ramp-down of the injection profile: as the injection rate decreases, there is no available liquid fuel to replace the one evaporated downstream and the tip penetration decreases. The fluctuations on the jet tip due to the evaporation process affect the measurements, large error can be observed on the curves in the last instant of penetration. The cone angle has been measured for both pilot and main injections but the values obtained for the first injection are very uncertain (large error bars) and do not have a significant trend. They increase in some cases and decrease in other cases. On the contrary, more coherent values have been measured during the main injection due to the longer extension of the jet and higher number of measurements. The cone angle variation is strictly linked to the penetration one. As penetration increases the cone angle decreases and, then, they both stabilize. It is interesting to note that whereas the jet tip recedes, an increase of cone angle is also observed (1500x5, 2000x5, 2000x10, and 2500x8).

Some main conclusions can be made by the analysis of the jet global quantities. The penetration and cone angle of the liquid jet provide useful and essential information about the fuel behavior in the engine but some aspects are missed. The pilot passes to the vapor phase shortly after the start of injection and only a few images can be collected. Moreover, the main spreads farther in the combustion chamber but the liquid penetration seems to arrest before reaching the wall. Therefore, it is likely to have vapor fuel that deposits on the chamber wall even if it was not observed.

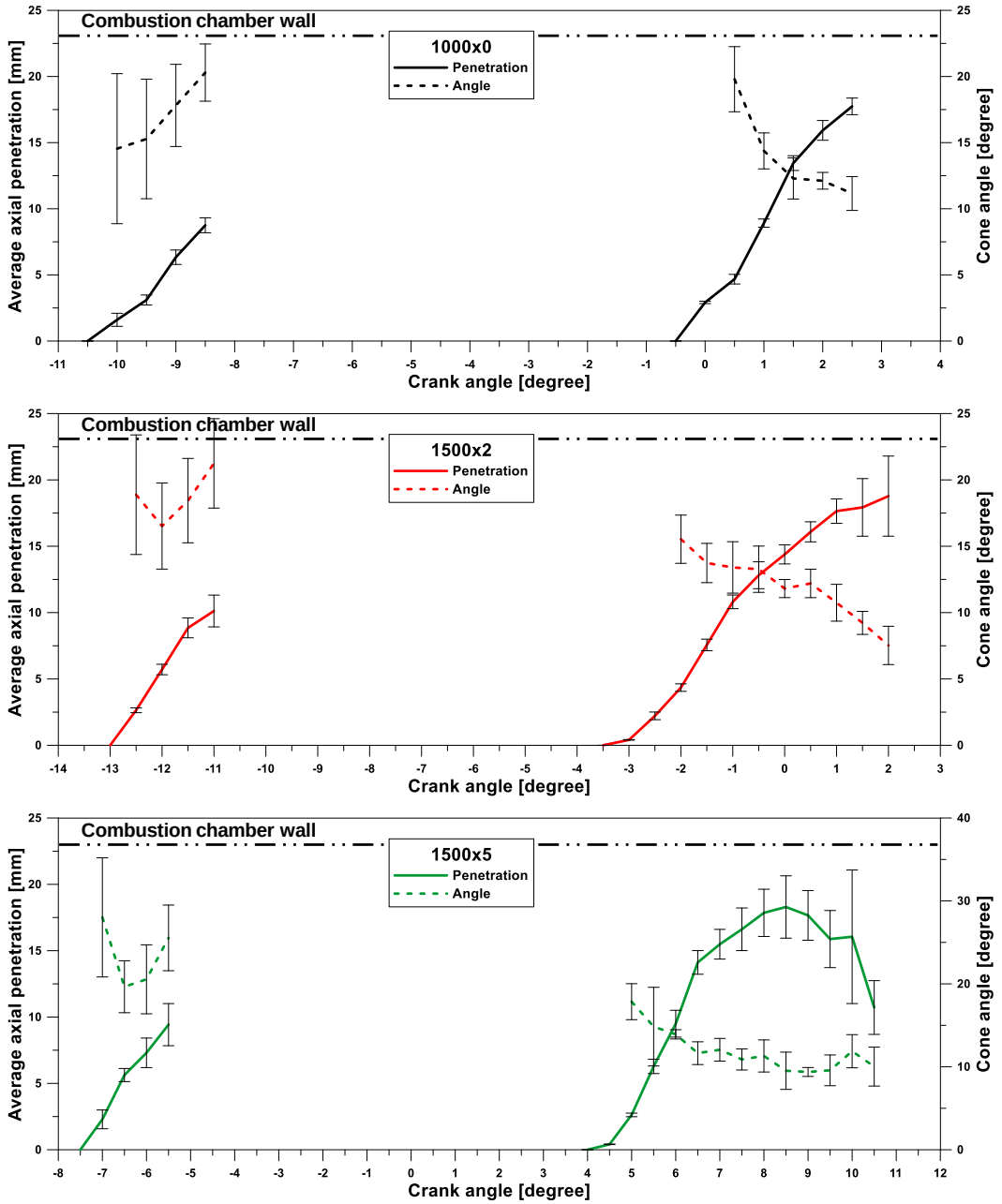

Figure 6.4: Penetration and cone angle of both the pilot and main injection at 1000x0, 1500x2, and 1500x5.

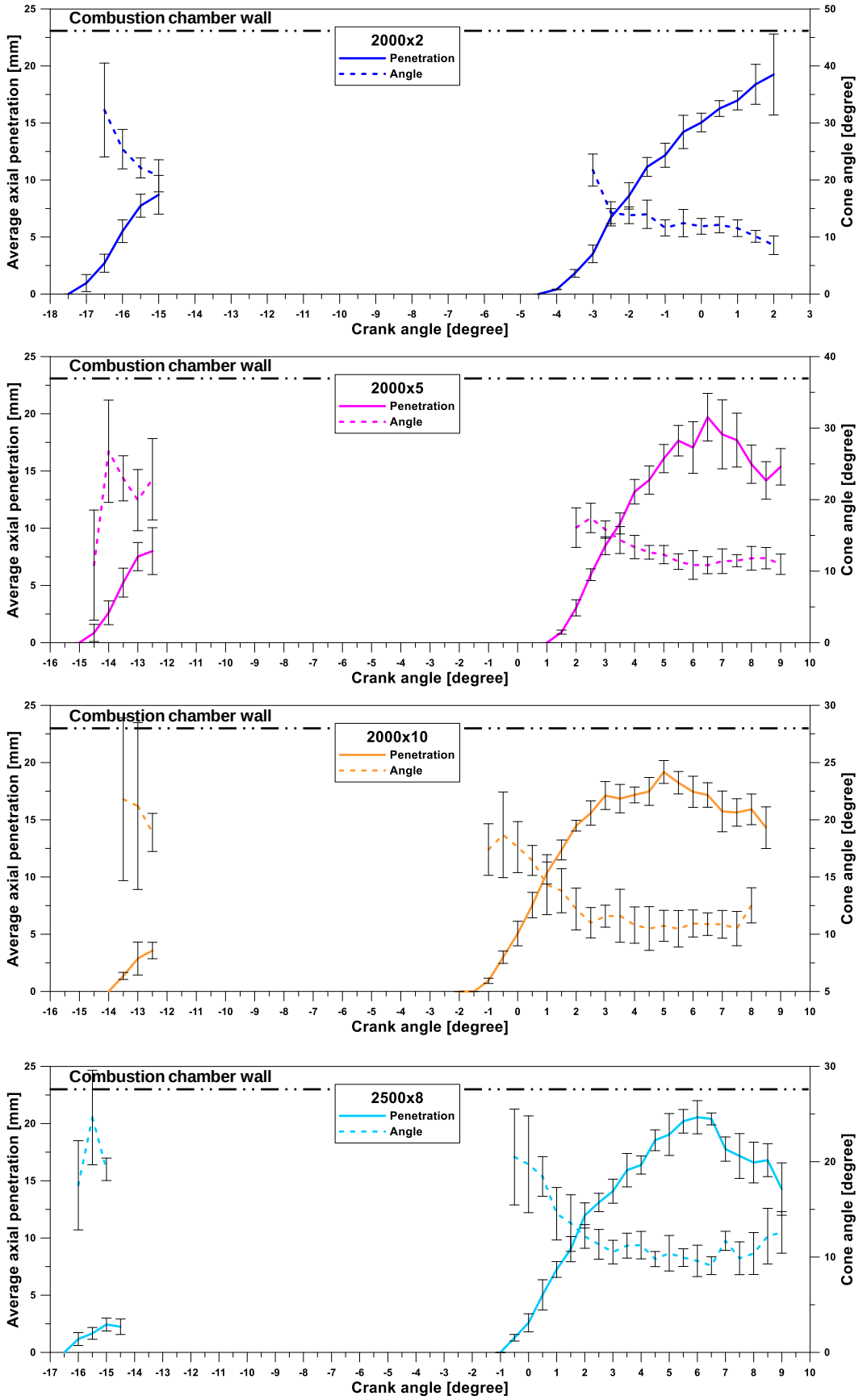

Figure 6.5: Penetration and cone angle of both the pilot and main injection at 2000x2, 2000x5, 2000x10, and 2500x8.

6.3 Accordance of experimental and model data: analysis of model sensitivity to injection parameters

A preliminary analysis of the model sensitivity to the injection parameters as the rate of injection and the cone angle has been carried out to investigate the capability of the model to match the experimental data.

The model considers a triangular jet shape defined by the cone angle (see figure 4.2). The boundaries of the control volume are where the velocity and F/A ratio are null. This assumption needs the vapor cone angle value; hence it is not true for the measured data because images in the visible range report only the liquid phase. The definition of the spreading angle is very important because it influences the spray equivalence ratio [82], and then the axial distance where the equivalence ratio curve crosses the threshold for the detection of the liquid penetration. Different values of the spreading angles have been used in the model to find the best match. In figure 6.5, preliminary results of the model and the experimental liquid penetrations have been reported as example in the conditions 1500x2 and 1500x5. The cone angles used are the average values during the late injection that is when the jet is completely developed; they are 12.4° and 11.4° at 1500x2 and 1500x5, respectively. In both investigated engine conditions a good agreement can be observed in the early injection phase; whilst there is an over prediction in the late injection. This discrepancy appears when the penetration becomes almost constant and it seems to be linked to the jet deceleration. By simulating the same conditions and using the average value of the cone angle during the early injection a different behavior can be observed. The new cone angle is 1.2 times wider than the average one in the late injection. This wider angle could be a good approximation of a volume composed of liquid and vapor fuel. The results have been reported in figure 6.6. Slight better results have been observed at 1500×2. On the other hand, a huge over prediction is still observable at 1500×5 even if its value is lower. In both cases, the separation between model and experimental curves is delayed and the over estimation is of lower intensity. However, the change of jet cone angle seems not to be the good solution.

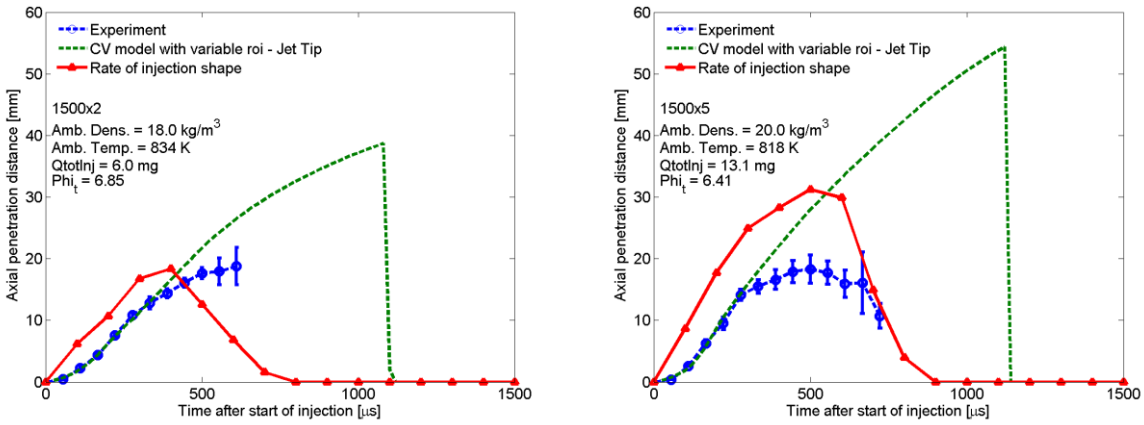

Figure 6.6: Model output with stabilized-jet cone angle: experimental vs. predicted penetration curve and related ROI for the conditions 1500×2 and 1500×5.

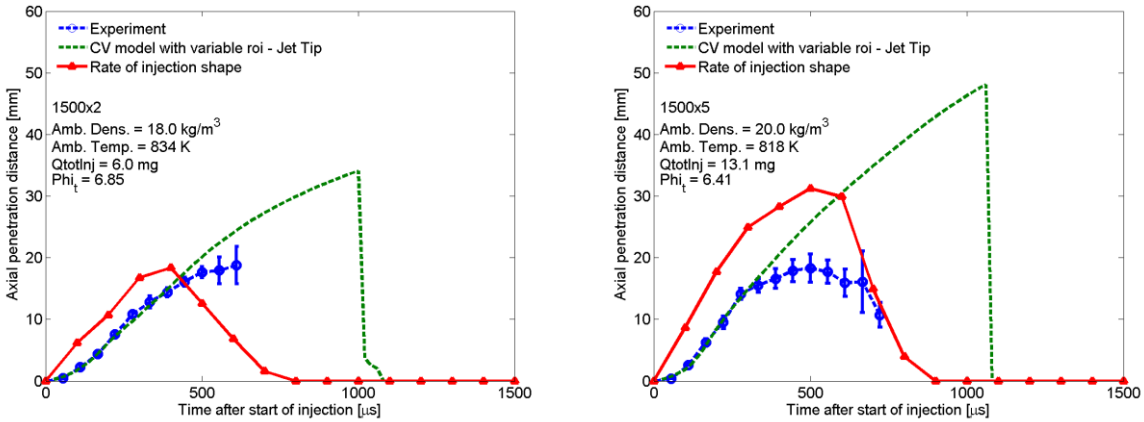

Figure 6.7: Model output with early-injection cone angle: experimental vs. predicted penetration curve and related ROI for the conditions 1500×2 and 1500×5.

It could be interesting to measure how much the variation of cone angle affects the curves of penetration. In Figure 6.7, the subtraction curves between the predicted penetrations in the two cases (cone angle early - cone angle late injection) have been shown for both engine points. The graph highlights that there is no effect of the cone angle before a certain time after the start of injection (150 µs ASOI). This observation is in line with Hiroyasu's description of the jet behavior. In the first stage, the jet penetration depends on the fuel momentum due to the injection pressure; on the contrary, it is affected by in-cylinder density in the subsequent phase. According to this comments, particular attention has been paid to the injection profile or rate of injection (ROI).

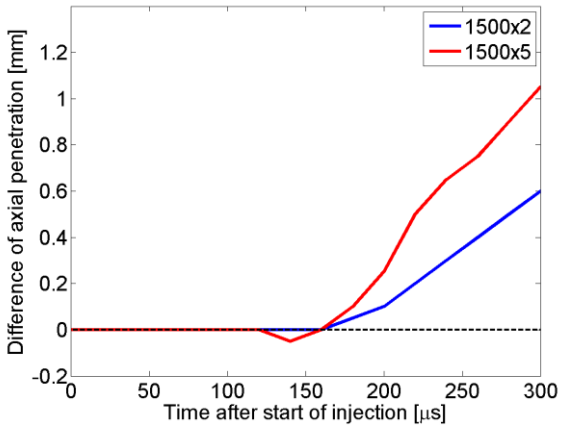

Figure 6.8: Difference between predicted penetration curves of Fig.6.5 and Fig.6.6 for both engine points.

In Figure 6.8, several penetration curves from the model have been compared with the experimental one using different ROI. The first ROI is the top-hat profile; the second is rump-up profile, and the third is a rump-up profile with two steps. Both the graphs at 1500x2 and 1500x5 show that the ROI shape strongly affects the penetration in the first instants of injection. The sharper is the rate of injection the longer is the early penetration. The analyses made so far on the effects of cone angle and ROI on the model penetration suggest that the mismatch between experimental and predicted data should neither be ascribed to the cone angle used nor to the ROI but to other causes. To understand the reasons of this mismatch it is important to clarify how the model takes into account for the liquid penetration.

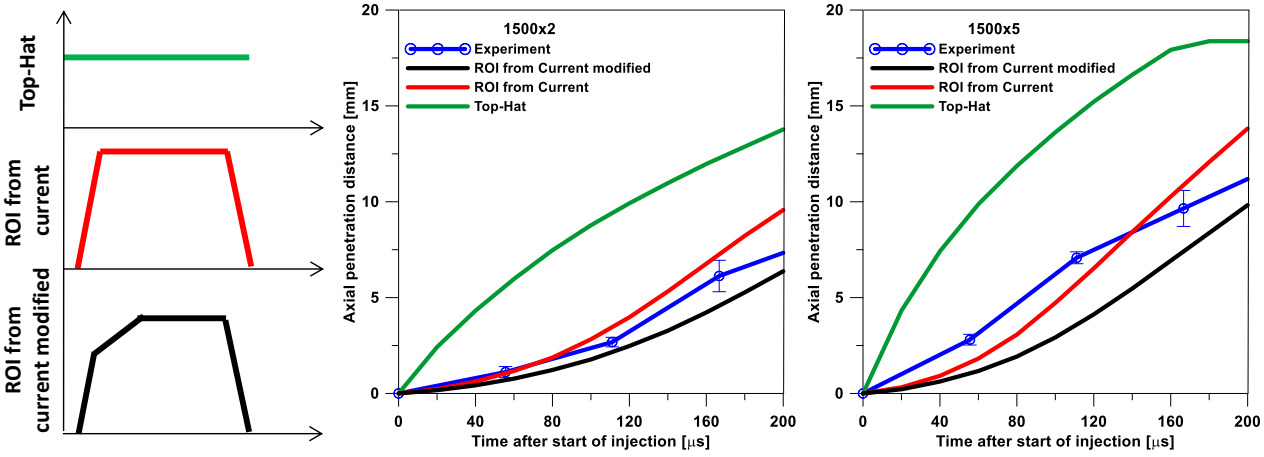

Figure 6.9: Experimental vs. predicted penetration curves obtained using different ROI at 1500×2 and 1500×5.

As stated in the paragraph 4.3, the model uses the equivalence ratio along the jet axis to detect the maximum liquid penetration. In Figure 6.9, the equivalence ratio of the centerline, the contour of the F/A ratio and the recorded image with the edge of the jet have been reported for the condition 1500×2 at 380 μs ASOI. At this instant, the model predicts very well the experimental

penetration. The equivalence ratio of the centerline (Figure 6.9a) shows rich regions near the injector (left side) and lean ones downstream. However, an increase in fuel fraction is observed on the jet tip. According to Pastor et al. [57], this behavior is typical of ROI with a ramped-up profile and it can be ascribed to the simplifications used in the model regarding the diffusive nature of the transient liquid jet tip. In this case, the model assumes that, during the injection ramp-up, the freshly injected fuel has higher velocity than the previously delivered one, and then the fuel accumulates on the tip. In this case, the threshold used is low enough to cross the equivalence ratio curve in a single point so generating a liquid region upstream and a vapor one downstream.

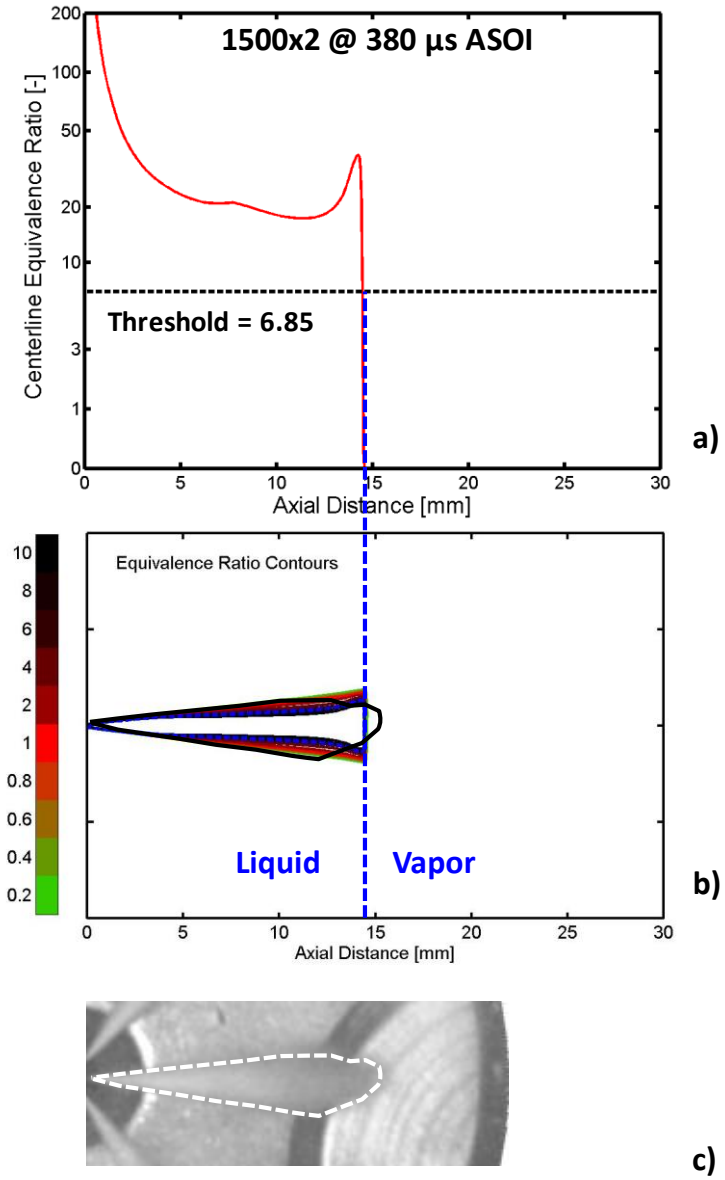

Figure 6.10: Condition 1500×2 at 380 µs ASOI a) Equivalence ratio along axial distance and threshold used. b) Equivalence ratio contour with indication of the liquid contour. c) Experimental image and liquid boundaries.

The good match between experimental and model data can be observed also in the 2d contour plot of modeled equivalence ratio in figure 6.9b where blue lines correspond to the liquid phase. The experimental jet contour has been obtained from the image of figure 6.9c. Figure 6.10 illustrates the same graphs for the condition 1500x2 at 600 µs ASOI. In this case, the local peak on the jet tip makes the threshold to cross the equivalence ratio curve in three points (a). As consequence, three regions are obtained: a liquid one upstream, attached to the nozzle; a vapor one in the middle; and another liquid region downstream (b). On the contrary, the experimental jet contour is characterized by a single body of liquid fuel that starts from the nozzle.

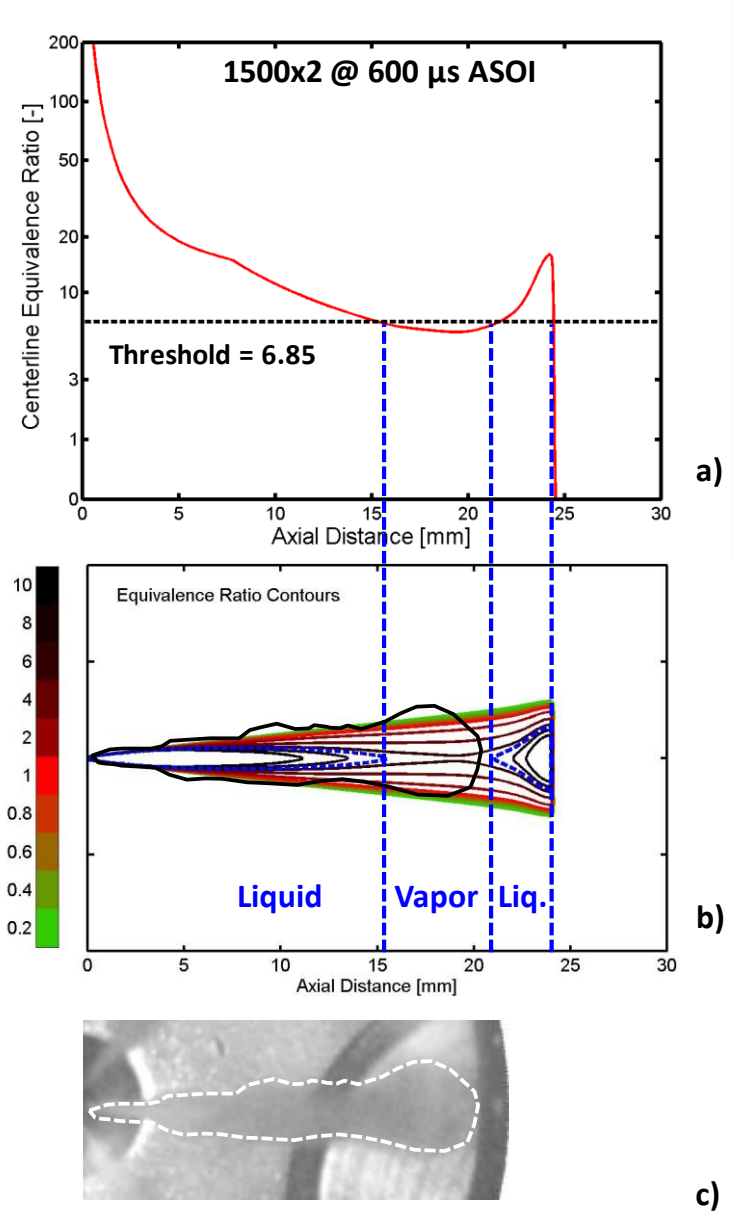

Figure 6.11: Condition 1500×2 at 600 µs ASOI a) Equivalence ratio along axial distance and threshold used. b) Equivalence ratio contour with indication of the liquid contour. c) Experimental image and liquid boundaries.

The overlaid image of experimental and model liquid contour reported in figure 6.10b highlights the deficiency of the model. Taking into account the considerations of Pastor et al. [57], previously reported, and the lack of experimental evidence of jet tip detachment, it is thought to follow the penetration of the jet body. Therefore, the model has been modified to return two liquid penetrations: one for the body and one for the detached tip of the jet. Figure 6.11 reports a comparison between model and experimental penetrations at 1500x2 and 1500x5. The penetration of the jet body can trace more accurately the experimental curve. In particular, only at 1500x2 encouraging results have been obtained. At 1500x5, the penetration is still over predicted even if the maximum penetration is almost halved. In addition, the jet body penetration can return also the typical jet recession at the end of injection.

It is evident that the graphs of figure 6.11 are not the definitive, additional implementations to the model are needed to fit even better the experimental data.

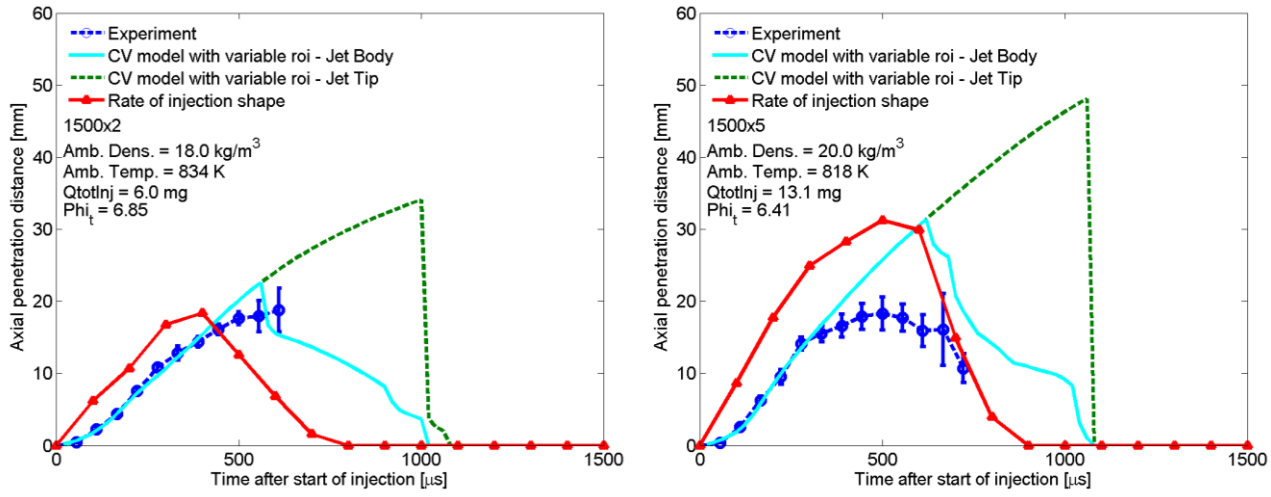

Figure 6.12: Model penetrations of the jet body and jet tip compared to experimental penetration of the liquid phase at 1500x2 and 1500x5.

6.4 Jet/wall interaction

As stated before commenting the images of figure 6.3, visible images can show only the liquid phase of the fuel missing information about the vapor fuel that moves toward the chamber wall. Knowing how much fuel accumulates on the chamber wall would be very useful for the evaluation of the combustion efficiency because it burns in rich conditions [83]. In order to visualize the reacting spray even after the vaporization and to investigate its evolution close to the periphery of the bowl, IR imaging has been performed. In particular, the IR wavelength at 3900 nm has been chosen because it can easily visualize the reacting spray without the influence of hot gas clouds

[84]. Fig. 6.12 shows a comparison between the images detected in the visible range and at 3900 nm for three crank angles of the late injection phase and the early combustion phase that is when impingement occurs. It is interesting to observe that at 3°CA after top dead center (ATDC), no more fuel can be detected from visible images, while its infrared radiation is still detectable. Infrared images allow to detect the fuel getting very close to the chamber wall. Moreover, at 6°CA ATDC and 9°CA ATDC, while the visible images show only the flames located on the jet axis, the fuel impingement is detectable at 3900 nm. In the IR images, the seven jets assume a mushroom shape on the tip due to the lateral diffusion of the fuel that impacts on the chamber wall. The experimental evidence of the fuel impingement is fundamental in order to understand the fuel/wall interaction and implement it in the 1d model.

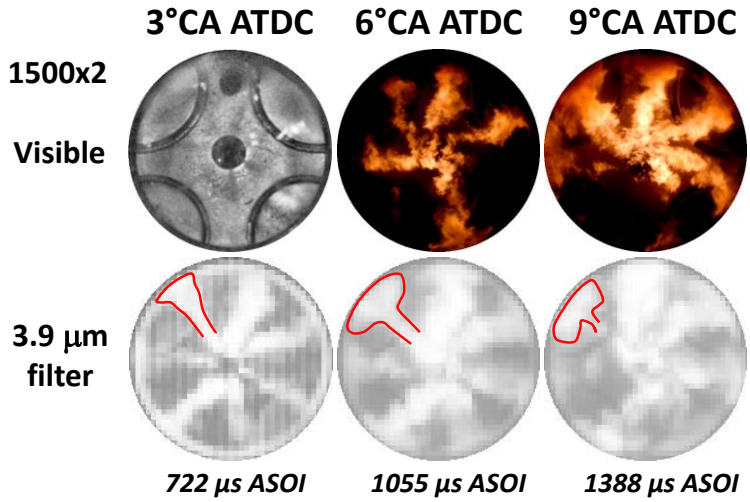

Figure 6.13: Images of the late injection and early combustion phases in the visible (first row) and infrared at 3900 nm (second row) at 1500x2.

As seen in figure 6.11, to consider an individual penetration curve for the jet body has allowed to better predict the experimental data. However it cannot be neglected that both the jet body and tip penetrations exceed the chamber limit of 22.88 mm. In order to reproduce the injection process within the combustion chamber of a modern diesel engine it is necessary to pass from an unlimited domain to a limited one setting the boundary conditions discussed in paragraph 4.4. In figure 6.13, the comparison between the experimental and the predicted penetrations considering an unlimited and limited domain have been reported for the engine condition 1500x2 as example. The predicted curves fit the experimental data for almost the whole injection process and stops at the wall distance.

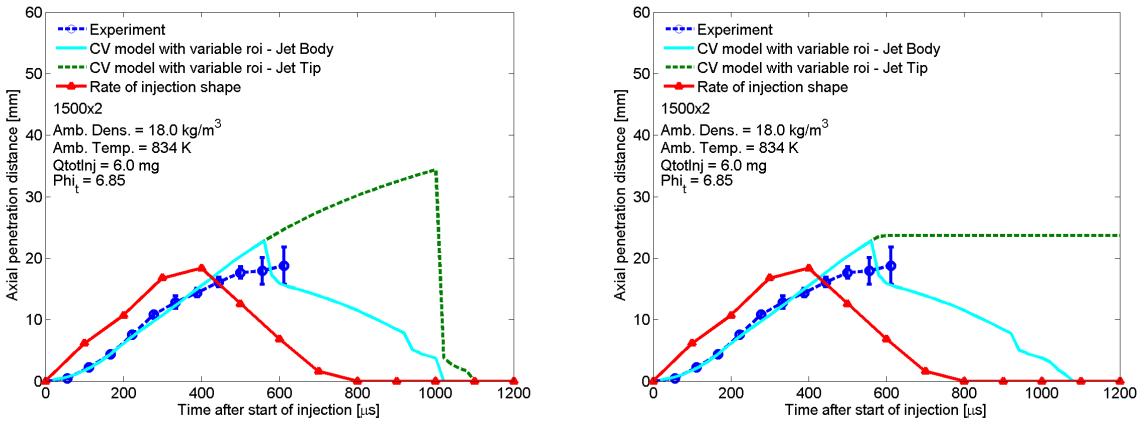

Figure 6.14: Experimental vs. predicted penetration curve and related ROI at 1500x2 without (left) and with (right) jet/wall interaction.

A separation between the jet body (solid line) and the jet tip (dotted line) can still be observed. When the jet/wall interaction is taken into account, different considerations can be made. Without jet/wall interaction, the farthest liquid region corresponded to the detached jet tip; now it corresponds to the fuel that impinges on the chamber wall. According to this, three phases of the penetration can be identified:

1. the fuel penetration increases (0–600 μs ASOI);
2. the fuel penetration arrests at the chamber wall (about 600 μs ASOI);
3. the jet recedes while a certain quantity of liquid fuel remains on the wall (after 600 μs ASOI).

Even if the liquid penetration of the jet body recedes, the vaporized fuel downstream continues moving toward the chamber wall. The accumulation of fuel on the wall caused by the momentum flow can be observed by the predicted 2d contour plot of the equivalence ratio of the jet reported in figure 6.14. No fuel can be observed after the wall limit and two liquid regions can be identified: the jet body and the impinging fuel. The first has the same shape of the case without wall interaction while the second has turned to a flat layer. As example, in figure 6.14, the comparison between the experimental and predicted penetrations has been reported for the conditions: 2000x2, 2000x5, 2000x10, and 2500x8. In all the cases, the total injected fuel mass has been reported together with the density and temperature values. An overall good agreement can be observed. The stage of increasing penetration is well predicted, and the maximum penetration values have been calculated quite well in terms of distance and time after the start of injection (ASOI). Whereas experimental data are available, the jet recession is followed with good approximation. Finally, after that the measured penetrations stops, the predicted ones continue

until the zero value. The lack of these data from the experiments could be due to the increase of in-cylinder temperature that promotes the fuel vaporization at the start of combustion not considered in this model.

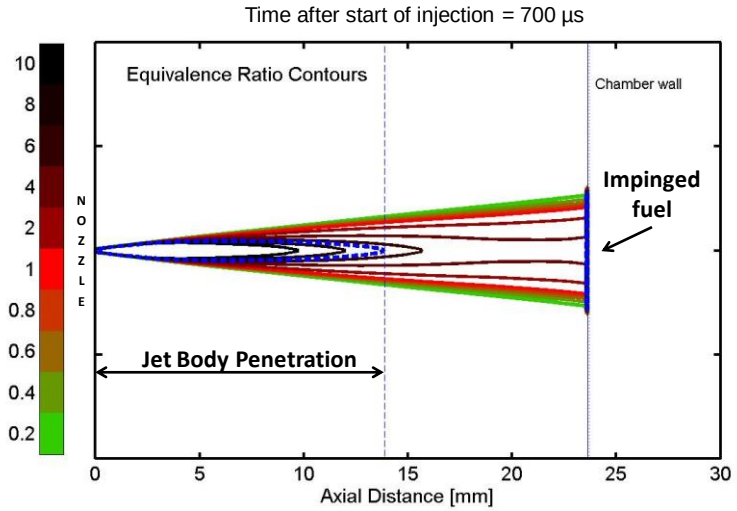

Figure 6.15: Predicted 2D contour plot of the equivalence ratio at 0.7 ms ASOI with wall interaction at 1500x2.

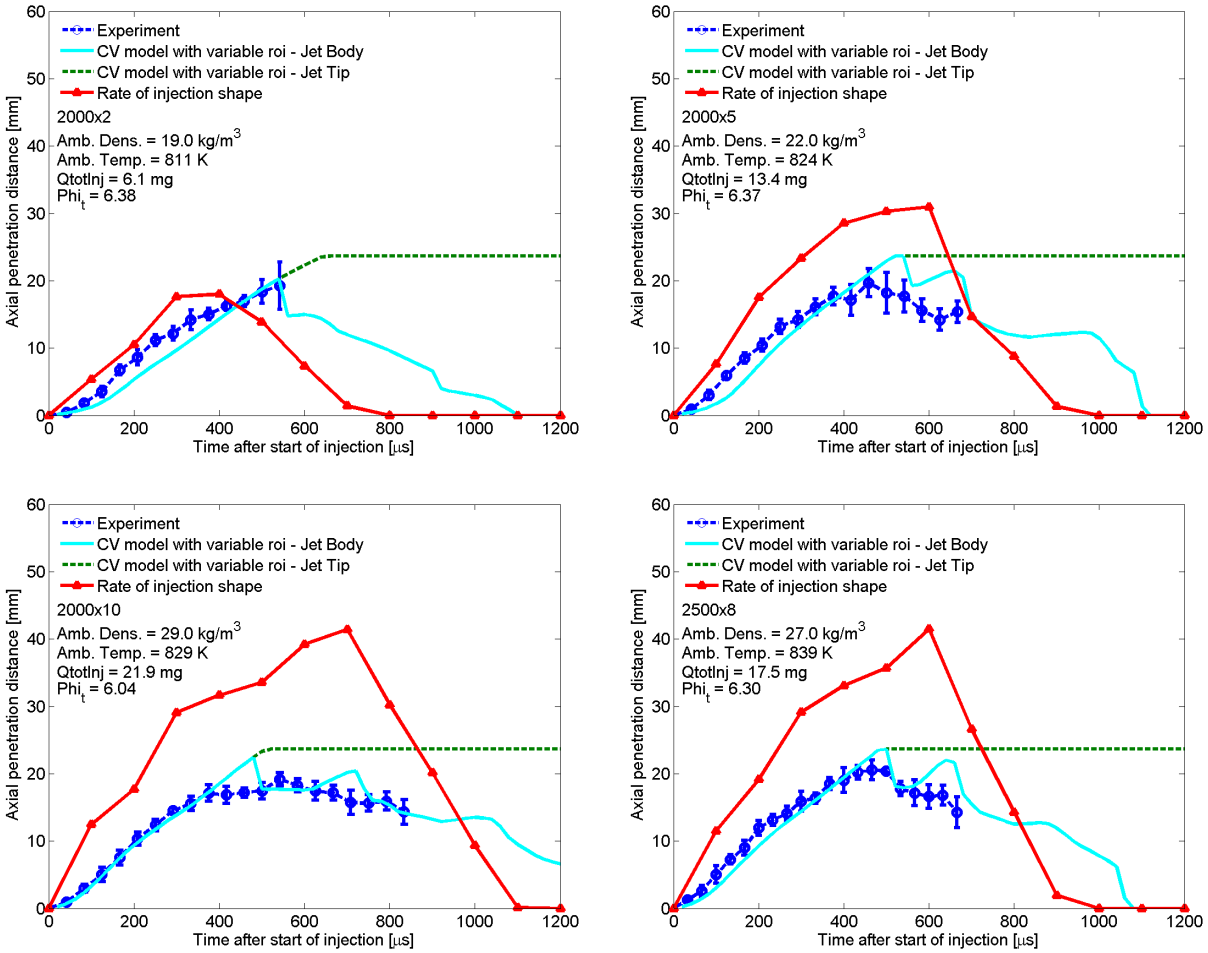

Figure 6.16: Experimental vs. predicted penetration curve and related ROI for the conditions 2000x2, 2000x5, 2000x10, 2500x8 with wall interaction.

6.5 Fuel impingement and PM emission at the exhaust

The fuel burning close to the chamber wall does not mix properly with the ambient gas and this affects the combustion efficiency in terms of performance and pollutants formation [2]. Moreover, if the mixture is poor in oxygen, some fuel droplets cannot get in contact with air and carbonaceous particles are generated [2, 85]. As reported in several papers, more intense is the impingement, less efficient is the combustion, then the PM emissions can increase [34, 37, 38, 83]. The fuel injected quantity has been calculated using the 1d model. Also the fuel amount impinging on the chamber wall has been evaluated so helping to understand the qualitative information of IR imaging. Figure 6.16 reports the normalized values of the fuel mass on the chamber wall and the particulate matter emissions with respect to the injected fuel amount for all the investigated engine conditions. It can be noted that both quantities in the graphs have the same trend. Higher impingement corresponds to higher PM emission. No significant effects can be ascribed to the engine speed; on the contrary, the engine load seems to play the main role. High impingement occurs at higher injection pressure and energizing time as observed at medium/high loads (5 - 10 bar of BMEP). This can be due to the combined effect of fuel velocity and total injected quantity that contribute to the fuel accumulation on the chamber wall to a greater extent compared to the low load conditions (0 and 2 bar of BMEP).

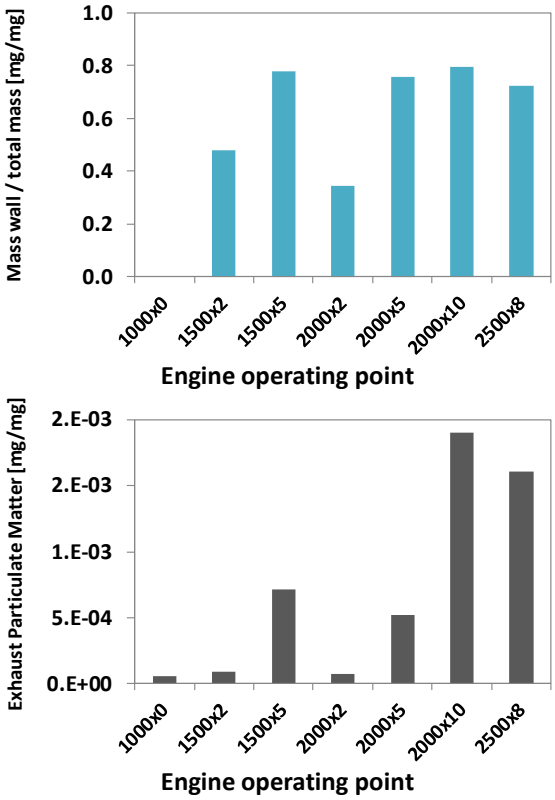

Figure 6.17: Normalized impinging fuel mass and particulate matter for all the engine operating points.

6.6 Infrared imaging: an innovative optical diagnostics to investigate the injection process and mixture formation

As demonstrated in the previous sections, the validation and tuning of the 1d model of Musculus and Kattke using experimental data has been fundamental to match in-cylinder conditions. However, diagnostics in the visible range is limited and it misses some important features of the fuel behavior in the combustion chamber. In particular, the lack of sensitivity to the fuel vapor phase is the most important issue. To this aim and to get further insights in the understanding of the fuel injection process and mixture formation in engine conditions a new optical diagnostics has been set up and applied. Infrared imaging at different wavelengths (3400 nm and 3900 nm) has been performed in the optical engine to overcome the limitation of the visible diagnostics. Since the optical technique is in the developing, the analysis concerned only one of the two injection events, the pilot, because of the absence of flames during the injection and its brevity. In addition, only two engine points have been investigated. The conditions 1500x2 and 2000x5 have been selected because they are characterized by the most frequent engine speed and load.

A sequence of images of the pilot injection in the visible range and in the infrared at 3400 nm and 3900 nm have been reported in figure 6.17 for the condition 1500x2. In particular, images of the end of injection process (from -11°CA to -8°CA) have been selected to highlight the different sensitivity of the two techniques adopted. In the visible, the liquid phase is detectable only at -11°CA and -10.5°CA. Then, the injected fuel is still observable but the jet shape is almost transparent and it is difficult to clearly identify the jet contour. In the following instants, from -10°CA to -8°CA, the fuel is invisible as the evaporation and mixing process is taking place. Visible images cannot show what happens in the combustion chamber, the lack of information about the fuel distribution and reaction in this phase represents a great limitation that can be overcome by using infrared diagnostics. Images at 3400 nm can show in a very defined and clear way the fuel during the whole investigated period. As previously described, the sensitivity to the C-H stretch bond makes this filter suitable for the fuel vapor detection [12, 46]. From -11°CA to -8°CA images show the fuel spreading in the combustion chamber. The jet contour can be easily outlined due to the high intensity of the images. The IR emission indeed depends on both fuel concentration and temperature [46]. The jet core is very intense while low IR emissions can be observed on the boundaries and on the jet tip. This is likely due to the more effective fuel/air mixing process in these regions. The maximum infrared intensity of these images increases over time (see Figure 6.17), as the piston is moving toward the TDC and the in-cylinder pressure and temperature

increase. Figure 6.18 reports a zoomed view of the combustion chamber in both the visible range and the wavelength at 3400 nm. The comparison shows that, when only the liquid phase is available (-11.5°CA, 111 µs ASOI), the jet shape detected is the same for visible and infrared. As the vaporization starts (-10°CA, 278 µs ASOI), liquid fuel is still detected along the jet axis in the visible image but the jet contour cannot be identified. On the contrary, the infrared image on the left side clearly denotes the liquid and vapor fuel locations. When all the fuel is in the vapor phase (-8°CA, 500 µs ASOI) and no information can be obtained from the visible images, the infrared radiation at 3400 nm puts in evidence the strong motion of the fuel in the combustion chamber that wraps the jet contour. Definitely, three intervals have been identified: until -11.5°CA, only liquid is in the combustion chamber; between -11°CA and -10°CA, the vaporization is started, there are both the liquid and the vapor phases; after -10°CA, all the injected fuel is in the vapor phase.

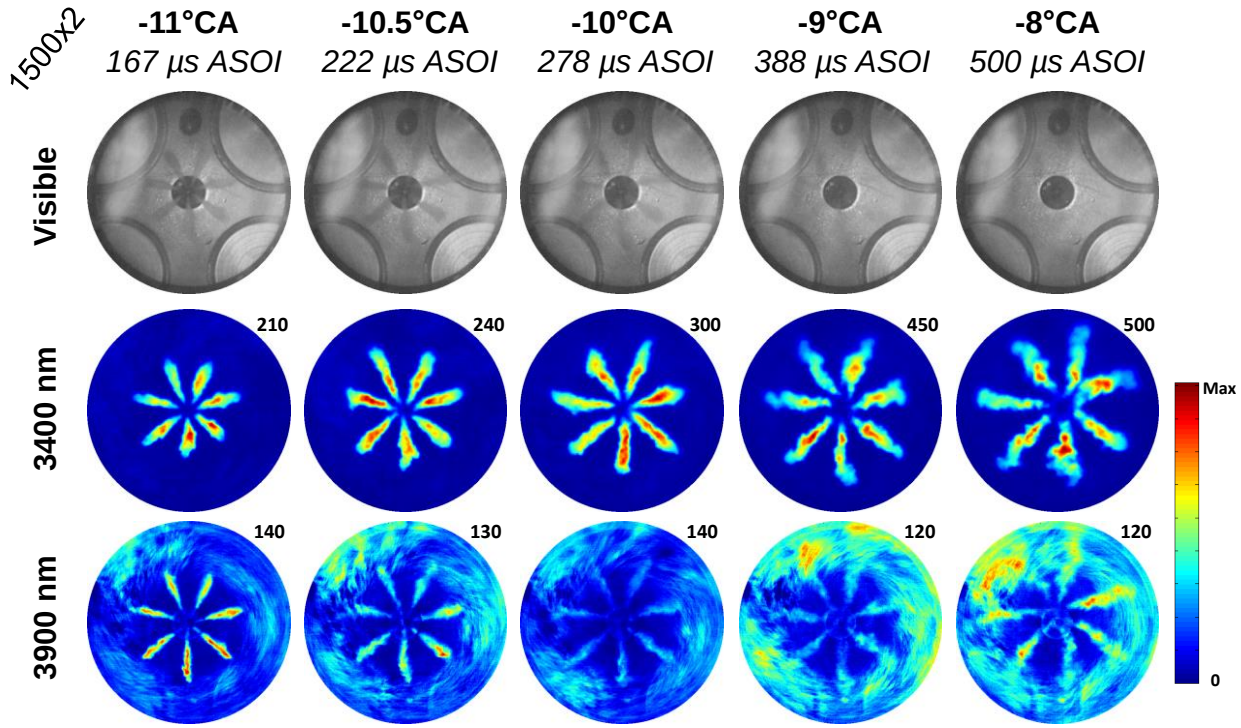

Figure 6.18: Images of the end of pilot injection at 1500x2 recorded in the visible (first row), in the infrared at 3400 nm (second row) and at 3900 nm (third row).

Finally, in the last row of figure 6.17 there are the images recorded at the wavelength of 3900 nm that revealed to be an indicator of the HCs [84, 86-88]. In the figure, the jets are well discernible at -11°CA. The core has higher intensity than the boundaries. The jets appear thinner in comparison to the image detected at 3400 nm but it seems they can reach the same penetration. At -10.5°CA, the jets are still detectable but with low intensity. As the evaporation process continues, the

infrared signal decreases and it is more affected by the noise. Finally, clouds close to the chamber wall can be observed in the images at 3900 nm due to the decrease of the signal to noise ratio.

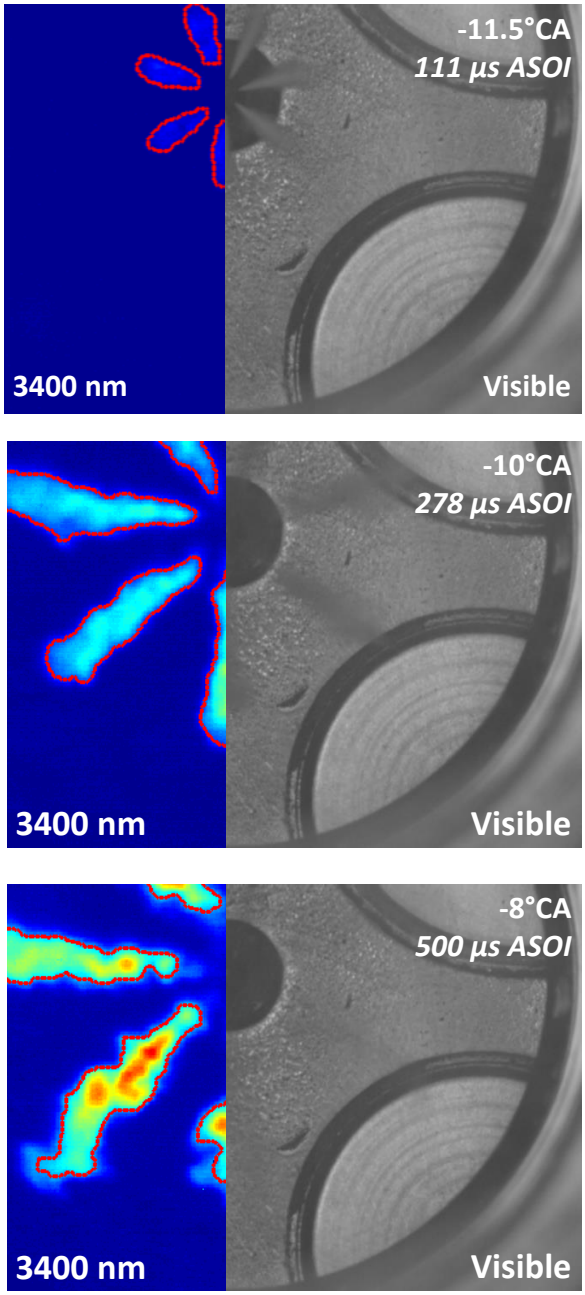

Figure 6.19: Comparison of the pilot injection at 1500x2 in the visible spectrum and in the infrared at 3400 nm.

The curves of measured jet penetration have been reported in Figure 6.19 for the two operating conditions and all the optical setup used. The figure shows that the visible penetration finishes at 200 µs after the start of injection (ASOI) in both engine conditions; this is the penetration of the liquid phase. At 1500x2 the maximum liquid penetration is 10 mm; while at 2000x5 it is 8 mm. As aforementioned, these distances will be considered in the model as the locations where the jet cone angle changes its value. The two IR curves at 3400 nm and 3900 nm overlap the visible one in

the first instants (until 111 µs/-11.5°CA, all the fuel is liquid; at this moment, the vaporization is not started yet). The curve at 3400 nm penetrates for a longer time, even when the fuel is completely vaporized, and reaches longer distance from the nozzle. The one at 3900 nm has the same penetration of the visible curve and a one-frame longer duration. The good agreement between the penetration curves of the visible images and those at 3900 nm indicates that this wavelength is appropriate to detect the liquid phase of the fuel using infrared diagnostics. This can greatly simplify the optical setup configuration for the acquisition of the liquid fuel by using only one camera without any external light source and by replacing the filter when necessary. On the other hand, the images at 3400 nm can detect the fuel vapor phase, as observed in the works [12, 46]. This allows to follow the spray evolution even when the jet disappears from the visible images. At 3400 nm, the jet stabilization can be appreciated around 400 µs ASOI for both operating conditions. As images of figure 6.17 show, the fuel vapor is highly affected by in-cylinder flows compared to liquid. For this reason, at each cycle, different values can be measured and high data dispersion is obtained. This explains the wider error bars calculated in this phase compared to the early injection.

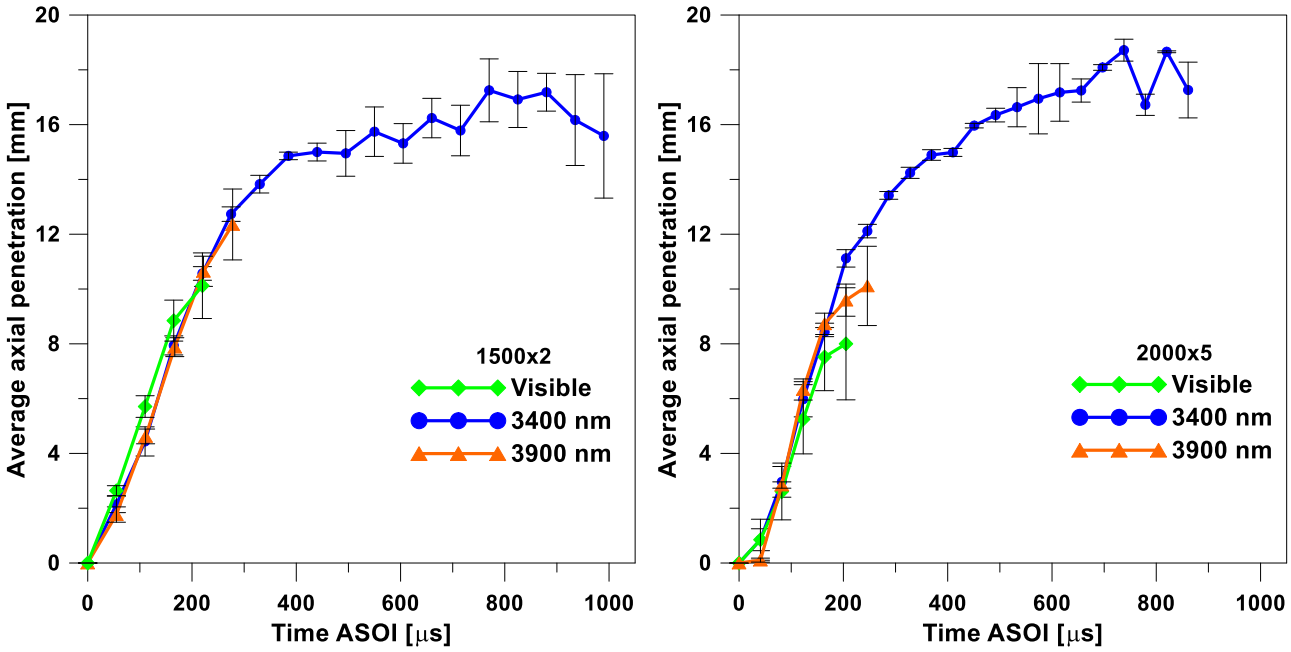

Figure 6.20: Average axial penetration of the pilot injection at 1500x2 and 2000x5, detected in the visible spectrum and at 3400 nm and 3900 nm.

Beside the jet penetration, the cone angle of the jets has been measured for the IR and visible images in both engine conditions. This is another significant parameter to evaluate the efficiency of the mixture formation. Figure 6.20 reports the average cone angle on five repetitions. Large data dispersion can be observed, especially in the early injection. A few data points are available

from the visible images and from those at 3900 nm, these are not sufficient to have an idea of the cone angle of the jets. On the other hand, images at 3400 nm provide useful information. Wider cone angles have been detected for the vapor phase, as expected, and narrower cone angles in the visible. It seems that the cone angles measured at 3900 nm are even smaller than the ones in the visible range for both the engine conditions. This can be ascribed to the sensitivity of this wavelength to the fuel rich zones of the jet that are located on the jet core [84, 87]; therefore the resulting image of the jet is narrower that the visible one. For each series of data, an interpolation line has been traced; the interpolation lines can be considered reliable only for the points related to 3400 nm because of the higher number of points and their coherence. Hence, from the data at 3400 nm, an average value of the cone angle has been extracted for the vapor phase of the jet; it is 22° at 1500x2 and 26° at 2000x5. The higher value in the medium load condition is justified by the higher in-cylinder density due to the higher pressure (see Figure 6.1).

The results obtained by the analysis of infrared images provided new insights about the fuel vapor phase. The application of this innovative optical diagnostics can lead to a better understanding of the processes that regulate the combustion process and formation of pollutant emissions.

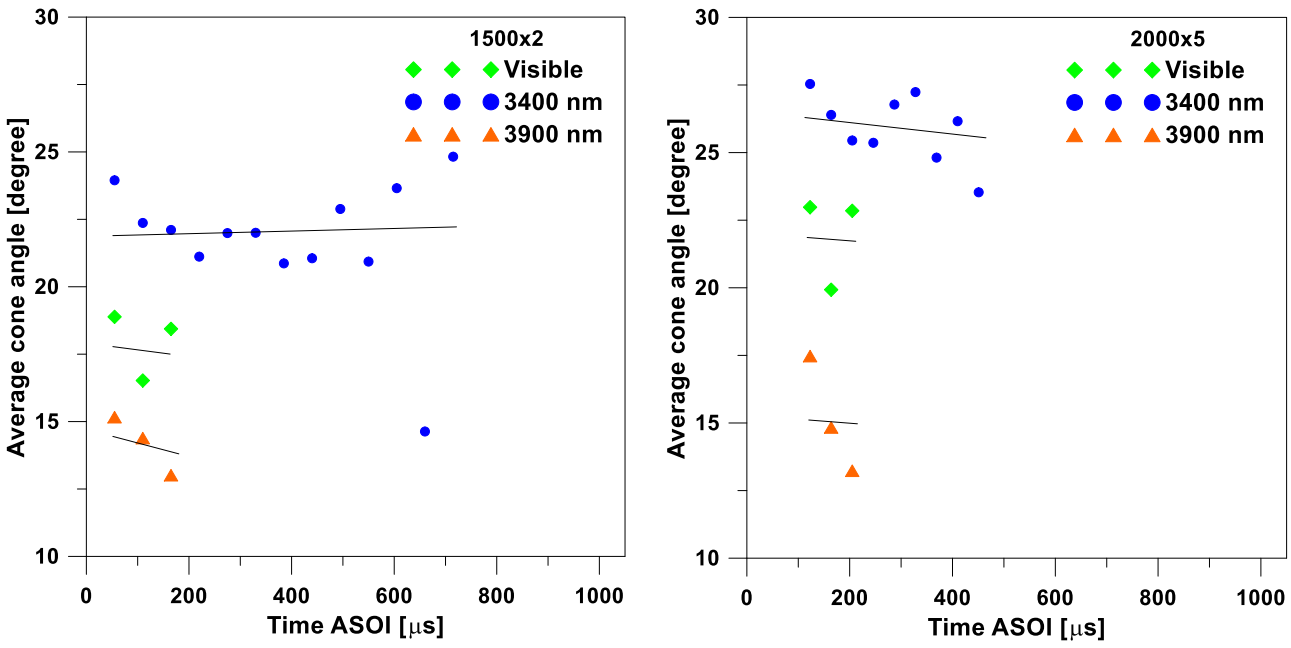

Figure 6.21: Average cone angle of the pilot injection at 1500x2 and 2000x5, detected in the visible spectrum and at 3400 nm and 3900 nm.

6.7 Analysis of infrared data with the support of the 1d model

The efforts made to adapt the 1d model of Musculus and Kattke to in-cylinder conditions find a concrete application in the present case. The collection of infrared images and the detection of the jet global parameters, as penetration and cone angle, provided new experimental data about the injection process that can be better understood by comparing them to the model results. Modeled liquid and vapor penetrations have been compared to the measurements in the visible range and in the infrared at 3400 nm and 3900 nm. The measured cone angles at 3400 nm have been used as input for the simulations. In particular, according to Pickett et al. [68],two values of cone angle have been considered. They have been correlated to the experimental ones in order to avoid the use of tuning parameters. The used values correspond to 2/3 of the experimental cone angle (measurements at 3400 nm), in the near field, and to 4/3, in the far field. This approximation has been used because, in the near field, it produces values close to the ones measured for the liquid jets. The values of cone angles are: 15° and 17° in the near field, and 29° and 35° in the far field, at 1500x2 and 2000x5, respectively. The axial distance where the cone angle changes is the maximum liquid penetration detected from visible images, 10 mm and 8 mm, for 1500x2 and 2000x5, respectively. For the simulation of the pilot injection, the in-cylinder thermodynamic properties as pressure, temperature, and ambient density have been considered to vary over time according to in-cylinder measurements.

Figure 6.21 reports the modeled and experimental penetrations at 1500x2 and 2000x5. A good match has been obtained both in terms of liquid and vapor penetration. The prediction of the liquid phase penetration fits very well the experimental data detected using different techniques. It seems that, in both engine conditions, the measurements of liquid penetration in the visible miss the last point of the model curve (green dots and cyan line). On the contrary, the measurements at 3900 nm catch the liquid penetration until the end of the curve. The mismatch of the visible data can be ascribed to the unclear contour of the jets when they get transparent (see Figure 6.17). Then it is difficult to detect the penetration. On the other hand, the radiation at 3900 nm is stronger and prevents this problem. The use of different cone angles along the jet length improves the model reliability in terms of vapor penetration. Whereas smaller cone angles in the near field are useful to simulate the rapid penetration of the fuel that is exiting from the injector nozzle, the wider values in the second phase can reproduce the effect of air entrainment that slows down the jet. For both the investigated conditions, the model and experimental curves match very well. It is important to remark that here the cone angle is not intended as a tuning

parameter used to get the best fit. It is derived from experimental measurements and used as it is in the model in order to provide outputs, e.g. jet penetration, jet velocity, and equivalence ratio, which represent reliably the tested conditions. This is fundamental when the model is used to understand and explain experimental results.

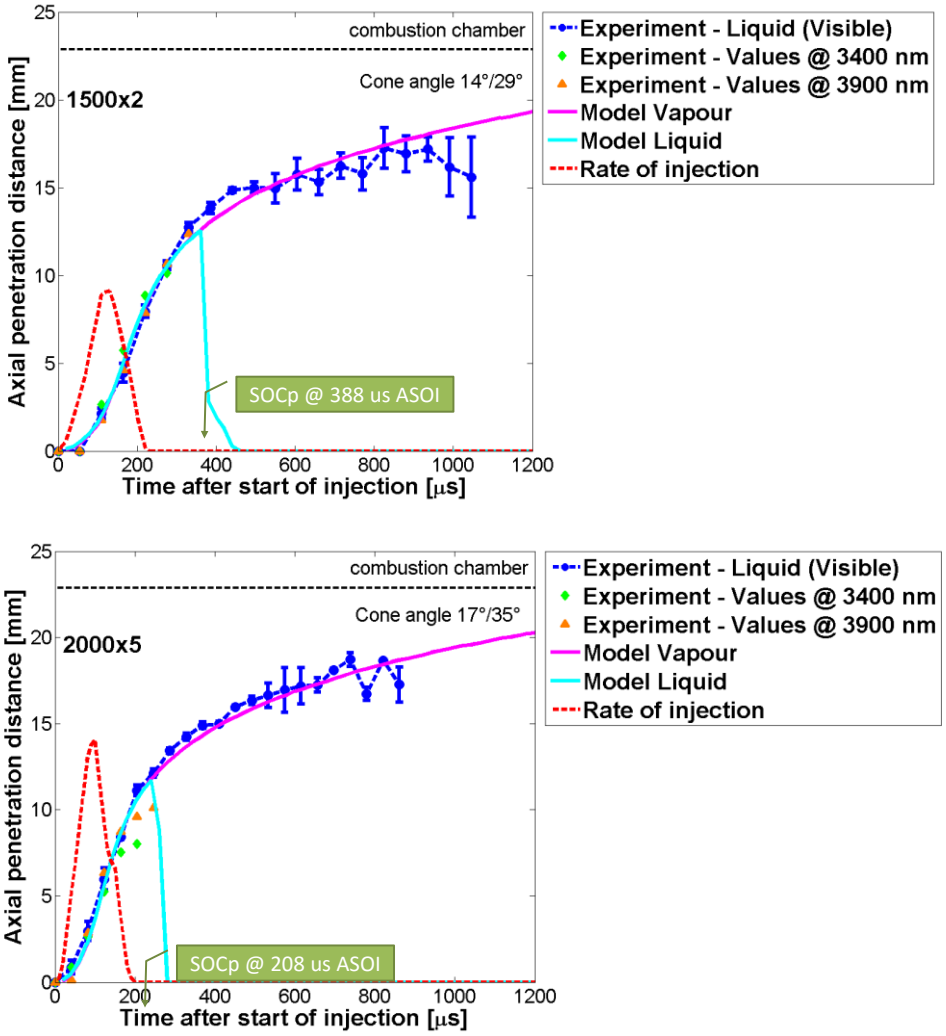

Figure 6.22: Experimental vs. predicted penetration of the liquid- and vapor- phase and ROI shape of pilot injection at 1500x2 and 2000x5 with variable cone angle. Near field limits: penetration <10 mm @ 1500x2, and <8 mm @ 2000x5.

Infrared imaging is sensitive to fuel temperature and concentration [46] and can provide information on the jet composition for which they should be used more sophisticated techniques (e. g. Rayleigh scattering).

The infrared emissions at 3400 nm and 3900 nm at 1500x2 have been evaluate along the jet axis defined in Figure 6.22. Since the same operating condition is considered in these measurements, the different emission behaviors are not due to temperature variation but depend on the species concentration. According to this line of reasoning, they should be indicative of the vapor and liquid fuel concentrations. Only one jet has been elaborated with the aim of making a qualitative analysis

and assuming that the seven jets have similar distribution in the combustion chamber. The results have been averaged on three image repetitions. The curves of infrared intensity along the jet axis have been reported in figure 6.23. They have been evaluated from the early injection (55 μs ASOI) until a few instants after the end of liquid penetration; the last graph corresponds to 444 μs ASOI.
At 55 μs ASOI no significant emission is detected at 3400 nm; on the contrary, at 3900 nm, a peak of emission is clearly observable close to the injector tip. This is due to the presence of liquid fuel at high concentration delivered from the nozzle at high injection pressure. The curve shows also high emission values close to the chamber wall. These are due to the clouds that form close to the chamber wall observed in Figure 6.17. Their contribution at 3900 nm is evident during the whole injection process; however, they do not prevent the identification of the jet. In the following instants (111 μs ASOI), immediately after the detection of high concentrated liquid fuel, significant contributions can be observed also at 3400 nm. This means that evaporation process starts already from the first instants of injection. However, the emission due to the liquid fuel is prominent compared to the vapor one. It is interesting to note that, despite of the maximum intensity, the curves cover the same distance from the injector tip. This means that the same jet penetration is obtained at both wavelengths (see Figure 6.19). From 167 to 222 μs ASOI, the increase of emission at 3400 nm can be observed while the peak value at 3900 is quite constant around 120 arbitrary units (a.u.). In particular, in this period, we can see the vapor emission intensity overcoming the liquid one. Reminding that only the concentration affects the different behavior of the two curves, some comments can be made. It seems that the liquid concentration increases and, then, decreases from the start of injection to 222 μs ASOI that is the end of injection detected from the ROI in figures 6.21 for 1500x2. On the contrary, there is evidence of vapor from the first instants and then its signal keeps to increase constantly as the fuel passes from the liquid state to the vapor phase. This indicates that the evaporation process starts immediately after the start of injection due to high pressure and temperature in the cylinder. At 278 μs ASOI, that is 55 μs after the end of injection, only a weak signal of the liquid phase can be detected. The liquid penetration can still be measured and it is the same of the vapor one. In the following, from 333 to 444 μs ASOI, only noise can be detected at 3900 nm while the emission of vapor phase is further increasing. From the time when no emission of the liquid fuel can be detected onwards, the increase of vapor signal is not justified by fuel evaporation because no more liquid fuel is available. In this case, it is rather the start of low temperature reactions that can affect the infrared signal but they are not such strong to produce a sharp increase of it.

Similar considerations can be made analyzing the data in the engine condition 2000x5. The figure 6.24 shows the model equivalence ratio and the measured infrared emission along jet axis at 3400 nm and 3900 nm from the early injection for a few crank angles. A peak of intensity close to the injector tip (-13.5°CA / 56 µs ASOI) due to the presence of high concentration of liquid fuel is evident again. At the start of evaporation process, the emission at 3400 nm becomes soon more prominent than the one at 3900 nm (from 111 to 222 µs ASOI). Vapor and liquid phase signals fall down at the same distance from the injector tip, meaning that the same jet penetration is obtained at both wavelengths. For the curve at 3900 nm a smoother profile can be observed and this makes it tricky to identify the jet penetration. However, from 278 µs ASOI on, the vapor concentration increases continuously as the fuel is evaporating; while, only a weak signal of the liquid phase can be detected.

Definitely, the comparison of infrared emission at 3400 nm and 3900 nm along the jet axis has highlighted the presence of three stages during the injection process: first, at the start of injection only liquid fuel is detected; second, both liquid and vapor are detected soon after the SOI; third, only vapor is detected. The identification of these three time intervals is perfectly in line with the one given above by the observation of penetration curves.

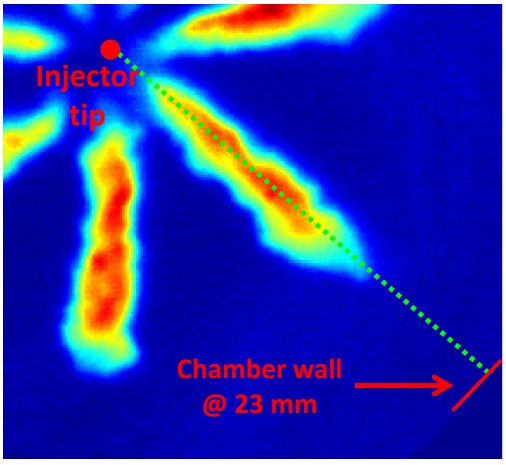

Figure 6.23: Investigated jet and definition of the jet axis profile.

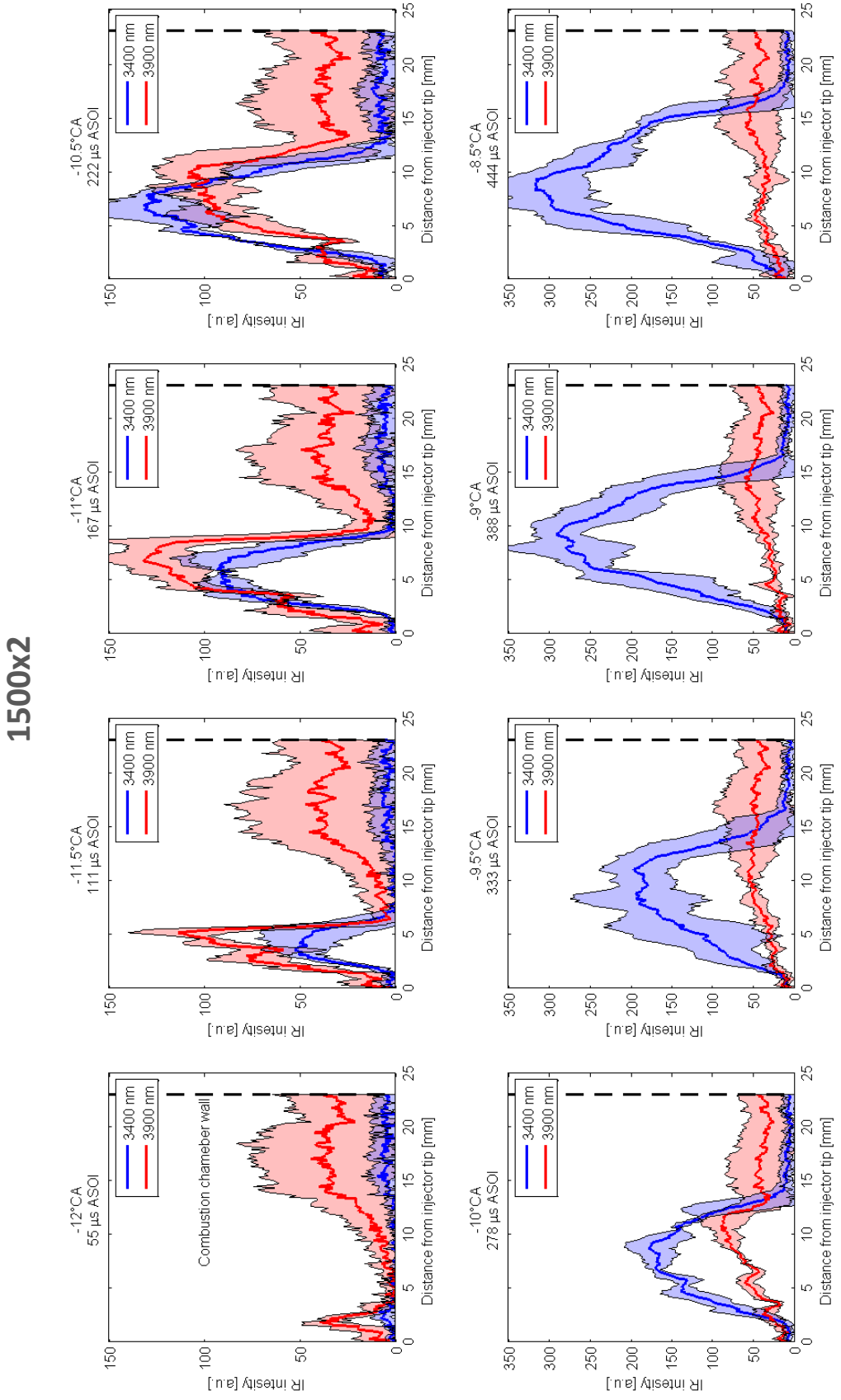

Figure 6.24: Infrared emission along jet axis at 3400 nm (blue curves) and 3900 nm (red curves) at 1500x2.

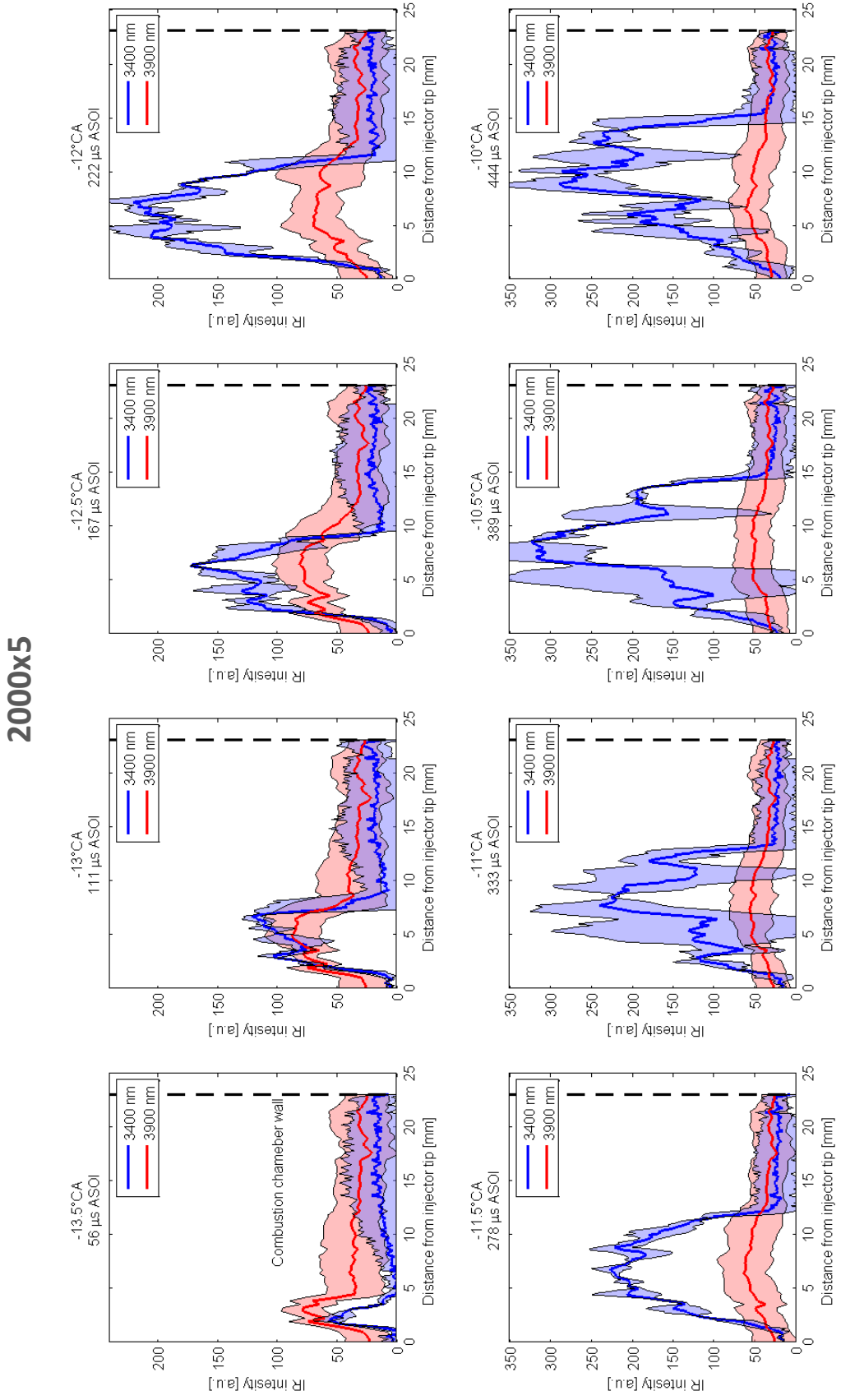

Figure 6.25: Infrared emission along jet axis at 3400 nm (blue curves) and 3900 nm (red curves) at 2000x5.

For this reason, it seems interesting to further investigate these stages with the support of the 1d model. It can help overcome the limitations due to the qualitative analysis of the infrared signals by getting quantitative estimation of the equivalence ratio. As for the evaluation of the infrared emission, the calculation of the fuel equivalence ratio has been made along the jet axis.

The curves of equivalence ratio along the jet axis for a few characteristic times of the injection process at 1500x2 and 2000x5 have been reported in figure 6.25. A semi-log scale on the y-axis has been used to represent clearly the values of both the early and late injections. The curves have the typical hyperbolic trend with a local peak on the jet tip. This is ascribed to the accumulation of fuel during the ROI ramp-up and has been discussed in more detail in [57, 89]. In order to find an indicator to compare the curves and to correlate them to the infrared emissions, the local minimum, before the peak of equivalence ratio, has been considered.

With regards to the condition 1500x2, at 55 μs ASOI, when no vapor is detected, the equivalence ratio is very high and the maximum value of the curve (green curve) is higher than 500 that is the y-axis limit. From 111 μs ASOI on, vapor is detected; the equivalence ratio is decreased to 150 (cyan curve) and gets even lower at 129 μs ASOI where it is 80 (black curve). Finally, 278 μs ASOI is the time when liquid fuel is no longer detected. The equivalence ratio has reached the value of 10 (second green curve of the plot). According to this comments, the liquid penetration should end at 278 μs ASOI that is indeed where the curve at 3900 nm has its last point in figure 6.19. However, the model prediction has a quite longer duration (see figures 6.21, cyan curves). It applies a threshold to the equivalence ratio curves of about 6 (dashed gray line in figure 6.25) and it identifies the end of liquid penetration around 387 μs ASOI. Similar results in terms of behavior of infrared emissions and value of critical equivalence ratio have been obtained also in the engine condition 2000x5. Here, the model identifies the end of liquid penetration at 278 μs ASOI, when the threshold of equivalence ratio is reached. This time is once again confirmed by infrared data because it is when no significant radiation at 3900 nm can be detected.

The main result of this analysis is that the emission at 3900 nm is related to the fuel equivalent ratio. The critical equivalence ratio for complete vaporization identified by experiments with model support is very close to the one obtained using the Siebers' theoretical correlation (used by the model) [14]. This depicts the wavelength at 3900 nm as a suitable way to detect the liquid phase of the fuel via infrared imaging. On the other hand, emission at 3400 nm, that is already used as an indicator of vapor fuel [12, 46, 75, 76], combined with the one at 3900 nm is able to

identify the start of fuel vaporization and to give information about the corresponding equivalent ratio with the support of 1d model.

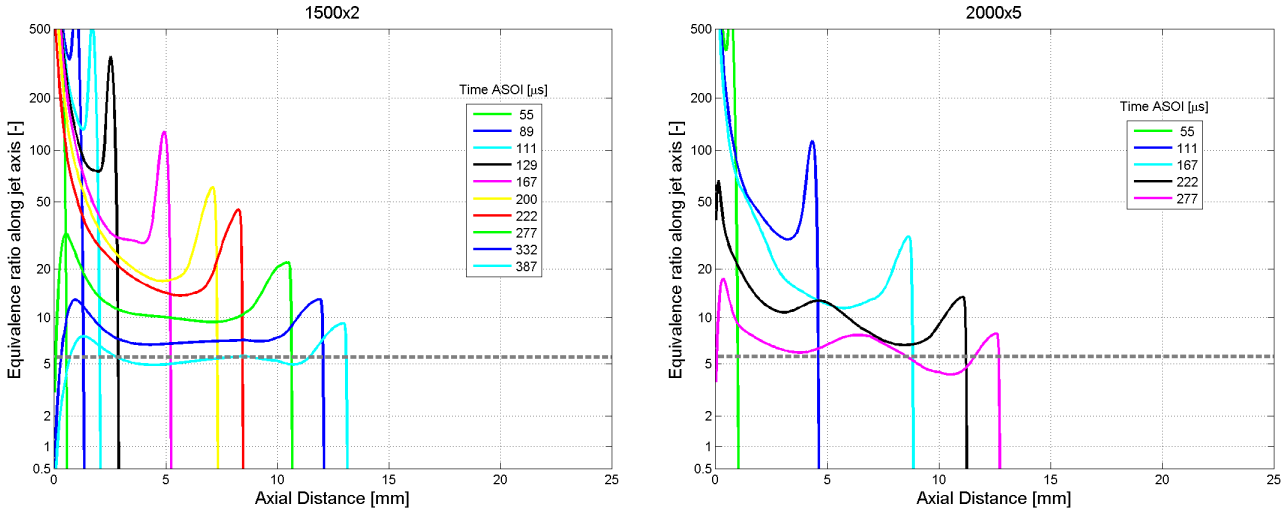

Figure 6.26: Model equivalence ratio along the jet axial at 1500x2 (left) and at 2000x5 (right).

6.8 Simulation of double injection strategies

After the model has proved its applicability to optical engines for the analysis of the separated injections, the natural evolution has been to reproduce the multiple injection strategies performed in the engine as also suggested by Tauzia et al. [70]. All the engine operating conditions analyzed in this work were characterized by two injections for each combustion cycle, the pilot and the main injections. Whereas the first has the role to prepare the chamber to the combustion event, the second one delivers the quantity of fuel needed to get the desired power output. Hence, the peculiarity of the main injection is that it enters in an environment composed of air and vaporized fuel of the pilot injection. Despite of its simplicity, the model is able to evaluate the behavior of a fuel jet injected in a mixture of air and fuel. Therefore, by setting the measured rate of injection for both pilot and main, and the pressure, temperature, and density variations over time, the model has been run to simulate the double injection strategies in all the engine operating conditions. Figure 6.26 shows the comparison between model and experimental results in the visible range. The model penetrations of liquid jet body and vapor phase have been reported together with the experimental data and the ROI. In the graphs, the two injection events are well discernable. The pilot injection is generally well predicted but the experimental data are available only for a few instants after the start of injection compared to the model data. This is more evident at high load conditions (2000x10 and 2500x8). As previously discussed, this is a limit of the visible imaging that is not able to follow the penetration of the pilot injection when the

evaporation process starts and the jets become transparent. Concerning the main injection, the experimental data are well predicted during both the rising phase and the stabilization period (evident at 2000x5, 2000x10, and 2500x8). In all the case, the model predicts the jet recession toward the nozzle after the end of injection.

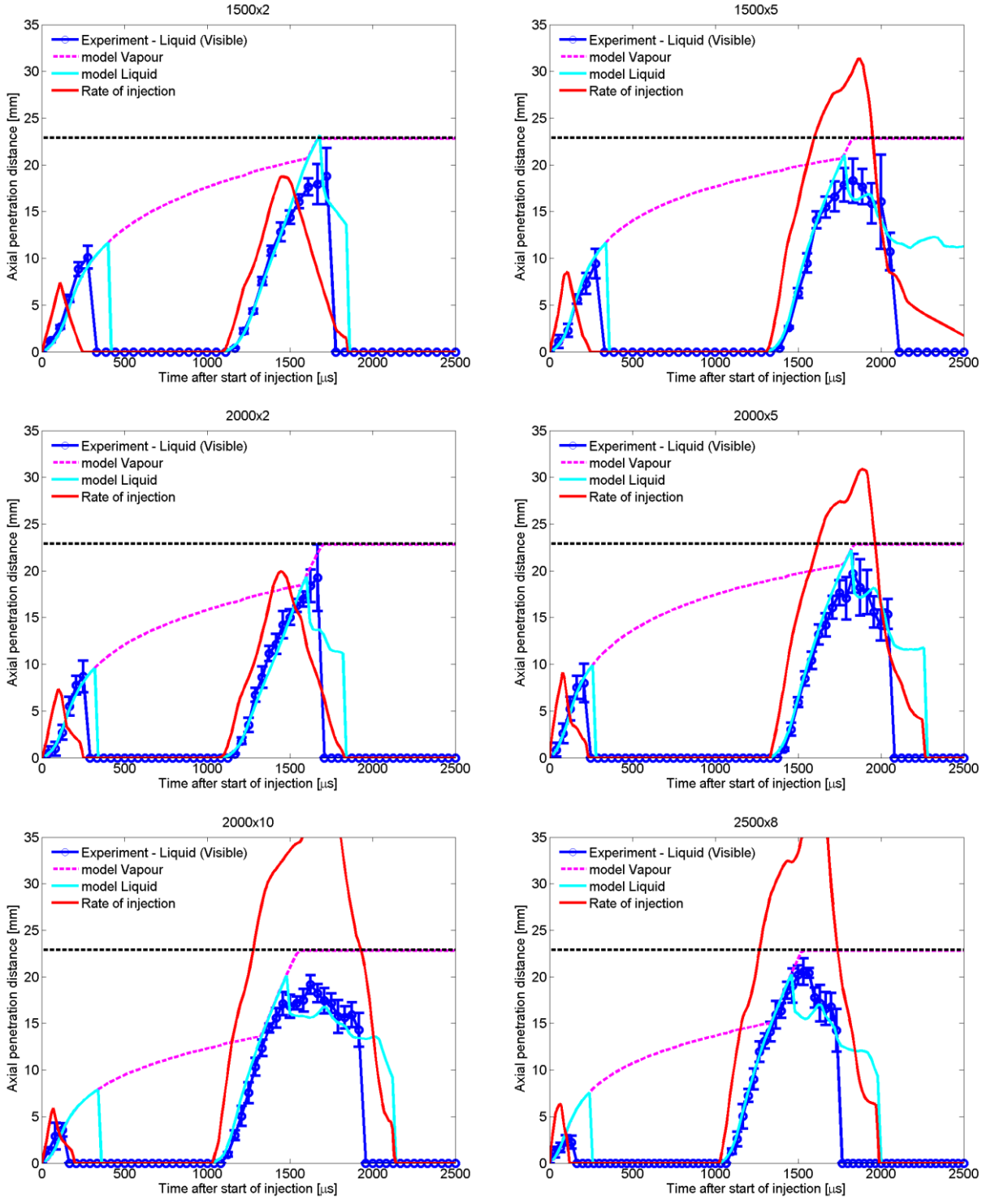

Figure 6.27: Simulation of double injection strategies at 1500x2, 1500x5, 2000x2, 2000x5, 2000x10, 2500x8.

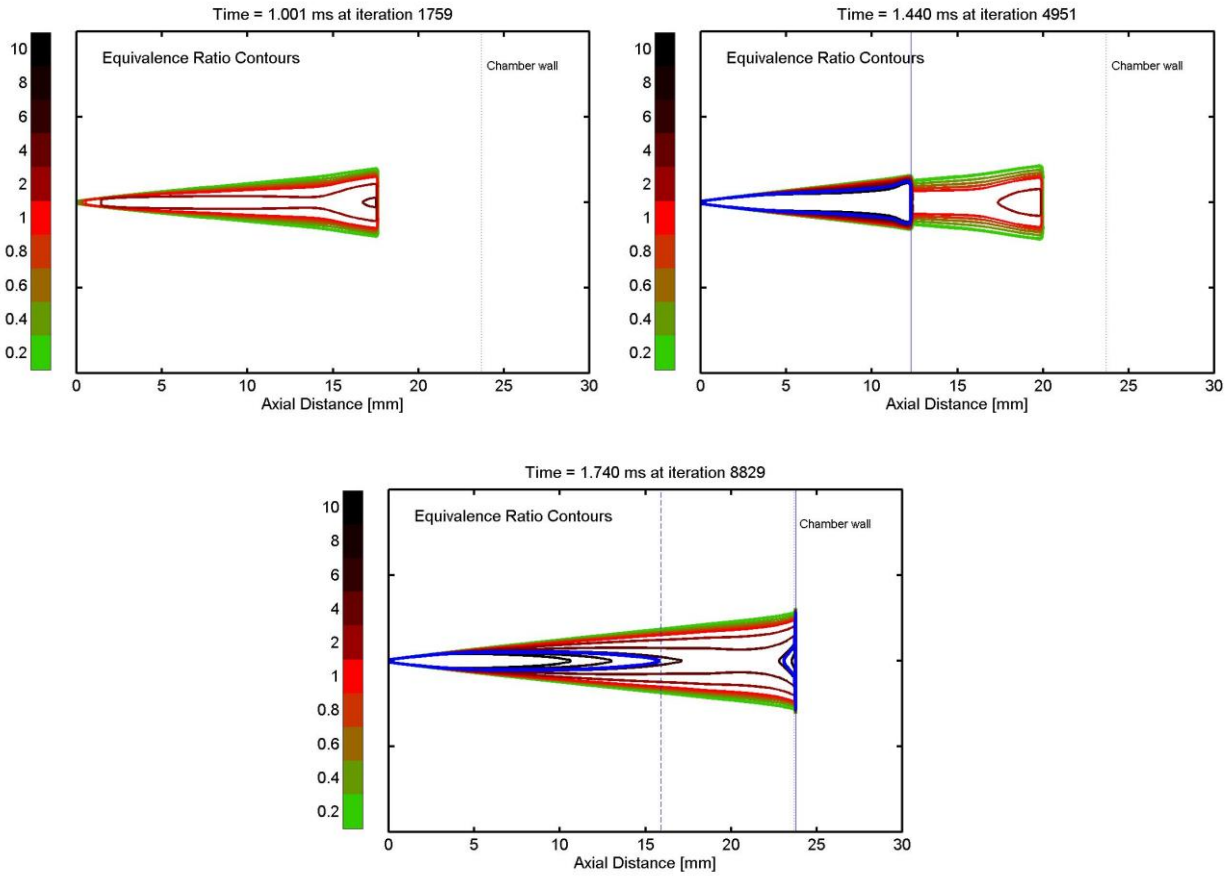

Figure 6.28: Simulation of double injection 1500x2. 2d contour of equivalence ratio.

Useful information about the vapor penetration is provided by the model. At the start of main injection it can be observed that the vapor extends almost until the chamber wall. As the main penetration increases, the vapor penetration increases too, but does not accelerate because its momentum is not affected by the one of the freshly injected fuel in this kind of model. The vapor penetration continues undisturbed until the main injection reaches it. At this moment, the vapor penetration accelerates abruptly and the fuel reaches the chamber wall. While the penetrations of the jet tip and vapor phase stop at the chamber limit, the liquid one recedes and matches the experimental data quite well in all the conditions. Some interesting images about the main injection penetration in an air fuel mixture have been reported in figure 6.27 where the 2d contour plot of equivalence ratio has been reported for a sequence of subsequent instant of the main injection. At 1 ms ASOI pilot, the vapor fuel of pilot injection occupies the volume from the nozzle to the chamber wall. At 1.44 ms ASOI pilot, the main injection has started and is penetrating in the vaporized fuel that is unperturbed by the new injection event. The main injection penetrates at higher velocity compared to the vapor fuel of the pilot. Therefore, it reaches the vapor jet tip and overcome it. This causes the jet penetration to increase abruptly. At

1.74 ms ASOI pilot, the fuel of main injection extends from the nozzle to the chamber wall where it impinges, while a portion of liquid fuel (jet body) is receding toward the nozzle (the liquid penetration is decreasing).

6.9 Evaluation of fuel evaporation rate

The 1d model of Musculus and Kattke [15] has been modified to match in cylinder conditions. A few modifications of the code have been necessary to get useful information about the jet/wall interaction, the distribution of the fuel vapor phase, and the interaction between pilot and main injections. However, some details about the amount of liquid and vapor phase in the jet cross section are still missing. The model is able to identify the vapor phase regions according to the fuel equivalence ratio. This approach is used for the detection of the liquid penetration along the jet axis, but misses of information along the transverse profile of the jet. To evaluate the amount of vapor fuel at a fixed distance from the nozzle a similar approach has been used; it is described in figure 6.28. Here, the radial distribution of the fuel volume fraction has been reported versus the normalized radial coordinate $\xi=r/R$, it is the ratio between the local radial coordinate r and the jet width $R=\tan(\vartheta/2)z$ (z is the distance from the virtual jet origin). Half of the jet is considered; hence ξ ranges between 0 and 1. The fuel volume fraction follows the Abramovich profile [67]; higher values have been obtained on the jet axis and lower ones on the boundaries. By applying a threshold value corresponding to the fuel volume fraction of complete vaporization, which can be derived from the threshold of equivalence ratio, a value ξ^* can be found. This identifies two regions in the jet cross section: the liquid region and the vapor one.

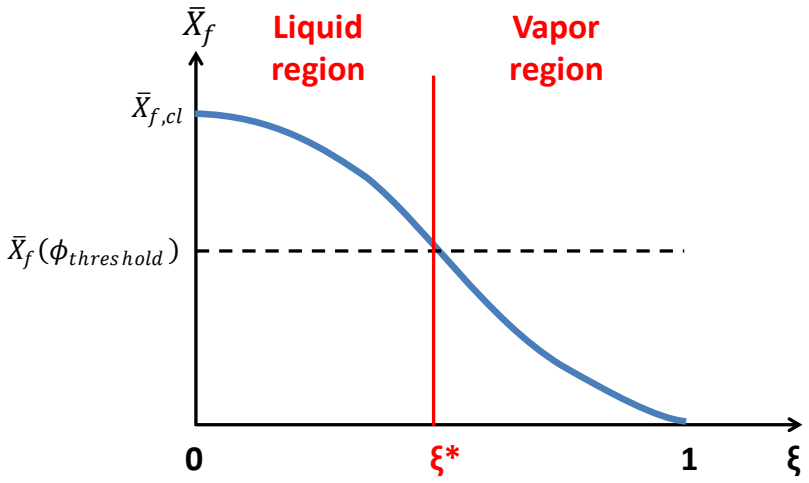

Figure 6.29: Radial profile of the turbulent mean fuel volume faction. The threshold value identifies the liquid and vapor phase in the jet cross section.

Then, the volume and the mass of liquid and vapor fuel can be calculated. A complete description of the equations used for this analysis has been reported in the Appendix C.

Figure 6.29 shows the evolution of total fuel mass, vapor fuel mass and liquid fuel mass over time for the double injection strategy at 1500x2. It can be seen that the total fuel mass increases when the injections take place (black). The liquid mass (blue) is characterized by an initial increasing part due to fuel delivery from the injector and a subsequent decrease because of evaporation process. In fact, the vapor mass increases at the expense of the liquid one. This can be clearly seen in the figure 6.29. After the end of pilot injection, the vapor mass is the same of the total injected fuel mass and no liquid fuel is present. With the start of main injection, the liquid mass increases again because the fresh fuel is being delivered. Soon after, the evaporation process of main injection starts and the vapor mass increases again so reducing the amount of liquid fuel. As for the pilot injection, at the end of main injection, the liquid fuel is completely vaporized. The vapor fuel mass corresponds to the total injected fuel mass.

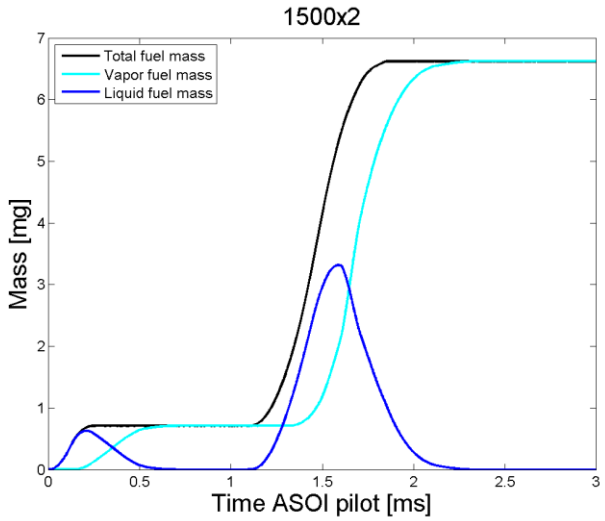

Figure 6.30: Evolution of total fuel mass, vapor fuel mass, and liquid fuel mass over time for double injection strategy at 1500x2.

The evolution of total fuel vapor mass over time allows to calculate the rate of evaporation of the fuel. This result can be easily obtained by the derivative of the total vapor fuel mass at each instant. The fuel evaporation rate versus time ASOI pilot has been reported in figure 6.30. The order of magnitude is 10e3 mg/s; this is in line with the results found in the literature [90-93]. This result is very encouraging because the rate of evaporation is calculated from a simplified model of fuel injection. This information is very useful because allows to connect the injection model to combustion models for which the rate of evaporation is an input and to evaluate the power output and heat release.

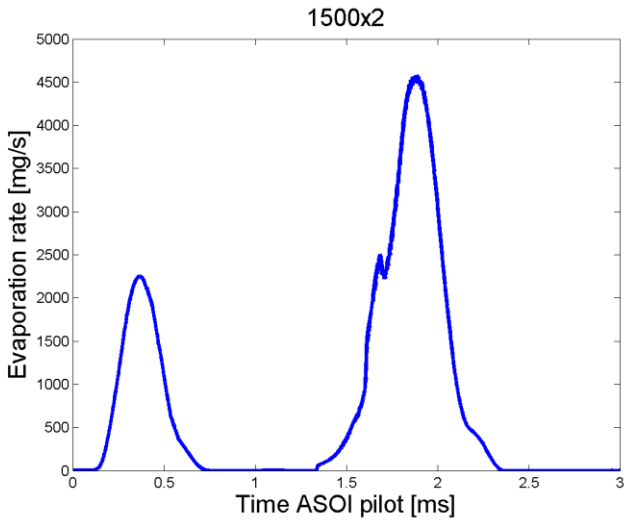

Figure 6.30: Modeled evaporation rate for double injection strategy at 1500x2.

Conclusions

Conclusions

Even if internal combustion engines are more than one century old, they are still the most used power train for transportation. In particular, compression ignition (CI) engines play the main role in the people and goods transport network. For this reason, a lot of research activities on CI engines are still on-going in order to improve their efficiency and performances. Moreover, they have been subjected to strict emission legislations, in terms of NOx and particulate matter (PM) emissions, to preserve the environment and to reduce the use of fossil fuels. To satisfy these criteria, modern diesel engines have reached a high technological level.

Experimental diagnostics and numerical simulations have allowed to understand their fundamental principles of operation. For example, experimental tests allow to reproduce the engine operating conditions in a controlled environment. In 1961, Bowditch patented the optical engine that revealed to be a powerful tool for the investigation of in-cylinder processes by their direct visualization. This test facility found large diffusion in the research context due to its great potential. Several optical techniques have been developed for the investigation of all the phenomena occurring inside the engine as the air flow, the fuel injection, the vapor fuel distribution, the detection of cold flames and pollutants formation. In addition, the rise of numerical models have strongly supported the experimental investigations of these phenomena and contributed to the control of the strategies, too. The combination of these two methodologies has demonstrated to be an effective tool for the study and the development of high pressure injection systems, allowing modern diesel engines to achieve high performance. The direct injection of fuel at high pressure inside the cylinder is a very fast and complex phenomenon that involves several physical and chemical aspects.

This thesis deals with the investigation of the injection process in a research CI engine performed via experimental and numerical methods. The experimental activities have been run on a single cylinder optical engine realized in the Istituto Motori of CNR. The engine has been equipped with an up-to-date Common Rail injection system; the head was from a commercial Euro 5, 4-cylinders engine with 1.9l of displacement. Only one cylinder has been used and it has been modified in order to obtain an optical access from beneath the piston. The engine has run seven operating conditions characteristics of the homologation cycle NEDC (New European Driving Cycle) when installed on a D-class vehicle. These operating points have been chosen in order to be as close as possible to the real working conditions of the engine. The investigation of the injection process has

been performed by visible imaging to detect the fuel liquid phase. The jet global quantities as penetration and cone angle have been detected for all the tested conditions. Besides visible imaging, a new non-conventional optical diagnostics in the infrared range has been realized and performed for the first time in an optical engine. To this aim, a part of the work made during this PhD has been dedicated to the study and setup of this innovative diagnostics to optical engines. Infrared imaging is not common for the investigation of high speed phenomena as that inside the engine due to the limitations of infrared cameras and their limited availability. The detection of the infrared self-emission of the fuel is very interesting; moreover, some issues of the well consolidated optical techniques can be overcome by infrared diagnostics (e.g. the number of optical accesses, the presence of light sources, and the purity of the excited fuel). In this work, two significant wavelengths in the infrared have been identified in order to analyze in-cylinder processes: 3400 nm and 3900 nm. The first has been chosen because it is sensitive to C-H single bond stretch emission and therefore it could give information on the fuel distribution in the combustion chamber. The second one is able to shield the hot gases radiation and it has been selected to take the hydrocarbons emissions into account. The results obtained via infrared imaging have been interpreted and understood with the support of a 1d model of fuel injection. A well proofed model developed in the Sandia National Laboratories for the simulation of fuel injection in a constant volume combustion vessel has been implemented by considering the volume and the thermodynamic properties variations inside the cylinder, and by modeling the jet/wall interaction. The adaptation of the 1d model to in-cylinder conditions allowed to use it to simulate the seven engine operating conditions experimentally tested.

The combined analysis of experimental and model data provided useful information on the fuel behavior in the combustion chamber. By considering the combustion chamber limits in the model prediction, a good match with experimental penetration has been obtained. The fuel mass that impinges on the chamber wall has been evaluated using the model results. By comparing it to the measurements of PM at the exhaust, a qualitative correlation between impinging fuel mass and PM at the exhaust has been found. Higher fuel impingement has shown to meet higher PM emissions. The jets penetration and cone angle have been measured for both visible and infrared images at the two selected wavelengths. At 3400 nm, it has been possible to follow the jets penetration for a longer period than at 3900 nm and in the visible range. Also the jets cone angles are wider at this wavelength suggesting that it can detect the fuel vapor. Penetration curves detected from images in the visible and infrared ranges have been compared to the predicted

ones obtained from the simulations. The comparison pointed out the suitability of the infrared filter at 3400 nm for the detection of the fuel vapor phase, and at 3900 nm for the liquid phase. By comparing the infrared emissions of the liquid and vapor phases at the same time during the injection process, it has been noted that for a very short period after the start of injection, only liquid fuel is in the combustion chamber; subsequently, the evaporation process starts and consumes the liquid fuel. The model has been also used to evaluate the jet equivalence ratio over time and these results have been compared to the infrared radiation at 3900 nm. The signal at this wavelength was detected until the evaporation threshold of equivalence ratio was reached. This correlation could lead to use the emission at 3900 nm as an indicator of the jet equivalence ratio even if additional investigations are needed.

The techniques and the results illustrated in this thesis contribute to the knowledge on the injection process in a CI engine and on the optical diagnostics for its investigation. The adaptation of a 1d model for engine environment is not limited to compression ignition engines but can be extended to all kinds of direct injection systems. For example, the gasoline direct injection engines for which new and more stringent emissions regulations have been promulgated. Another interesting application would also be to implement the injection model by coupling it to a combustion model for the evaluation of the engine performances. Concerning the application of infrared technique to engine optical diagnostics, at the moment several combustion research groups all over the world are working to set up this methodology. Hence, the observations and results reported in this thesis can be useful tools for the development of this technique.

APPENDIX A: Analysis of in-cylinder pressure

The trace of the in-cylinder pressure over time can give quantitative information about the evolution of the combustion process and the rate of reactions. The rate of heat release (ROHR), the heat released (HR) and the mean temperature in the cylinder can be derived from the pressure trace [2].

The ROHR is one of the most important parameter and indicates the rate of reaction of the fuel. It is used for the determination of the start of combustion, the combustion center, and to identify the kind of combustion is in progress, e.g. premixed, diffusive. For heat release analysis, the cylinder is considered as a thermodynamically closed system. According to the first law of thermodynamics, the energy balance of such a system can be expressed as follows [2]:

$$\frac{dQ}{dt} = \frac{dU}{dt} + \frac{dW}{dt} \qquad (AA.1)$$

Where *dQ/dt* is the rate of heat transfer to the system, *dU/dt* is the rate of change of internal energy of the system, and *dW/dt* is the rate of work transfer from the system. The internal energy, U can be expressed as:

$$U = mc_v T \qquad (AA.2)$$

Where *m* is the mass in the system, c_v is the specific heat at constant volume, and *T* is the temperature. If the mass in the system is constant, the derivative of *U* is:

$$\frac{dU}{dt} = mc_v \frac{dT}{dt} \qquad (AA.3)$$

From the ideal gas law:

$$pV = mRT \qquad (AA.4)$$

Where *V* is the volume and *R* is the specific gas constant. If *m* and *R* are assumed as constant, it follows:

$$\frac{dT}{T} = \frac{dV}{V} + \frac{dp}{p} \qquad (AA.5)$$

Using eqs. AA.4 and AA.5, eq. AA.3 can be rewritten as:

$$\frac{dU}{dt} = \frac{c_v}{R}\left(p\frac{dV}{dt} + V\frac{dp}{dt}\right) \qquad (AA.6)$$

The work performed by the system can be expressed as:

$$\frac{dW}{dt} = p\frac{dV}{dt} \qquad (AA.7)$$

Neglecting the mass exchange and using eqs. AA.6 and AA.7, eq AA.1 becomes:

$$\frac{dQ}{dt} = \frac{c_v}{R}\left(p\frac{dV}{dt} + V\frac{dp}{dt}\right) + p\frac{dV}{dt} \qquad (AA.8)$$

The specific gas constant can be expressed as:

$$R = c_p - c_v \qquad (AA.9)$$

Where c_p is the specific heat at constant pressure. Eq. AA.9 and the ratio $\gamma = c_p/c_v$ can be used to simplify eq. AA.8 in:

$$\frac{dQ}{dt} = \left(\frac{\gamma}{\gamma - 1}\right)p\frac{dV}{dt} + \left(\frac{1}{\gamma - 1}\right)V\frac{dp}{dt} \qquad (AA.10)$$

It is of interest to study the heat release rate as a function of crank angle degree, θ, hence, eq. AA.10 can be rewritten as:

$$\frac{dQ}{d\theta} = \left(\frac{\gamma}{\gamma - 1}\right)p\frac{dV}{d\theta} + \left(\frac{1}{\gamma - 1}\right)V\frac{dp}{d\theta} \qquad (AA.11)$$

APPENDIX B: Correlation between model and experimental cone angle

Discussions in the paragraph 6.3.1 pointed out the influence of the cone angle on the model results and the criticism of identifying the correct value. Experimental measurements offer a great support. However, Pickett et al. [55] noted that the angle value is very sensitive to the optical setup used, and finding the correct value could be not easy.

In the present study, several simulations have been run using different input cone angles until the best match has been found for each operating condition. The cone angles from model tuning (θ_{model}) versus the experimental (θ_{exp}) one for all the tested conditions have been reported in figure B.1. The experimental values in the graph correspond to the average cone angle during the late-injection phase (stabilized phase). As observable in the figure, a linear correlation can be extracted between the model and experimental cone angle. The relationship between them can be written as follow:

$$\theta_{model} = 2.3 \cdot \theta_{exp} - 9.5 \qquad (AB.1)$$

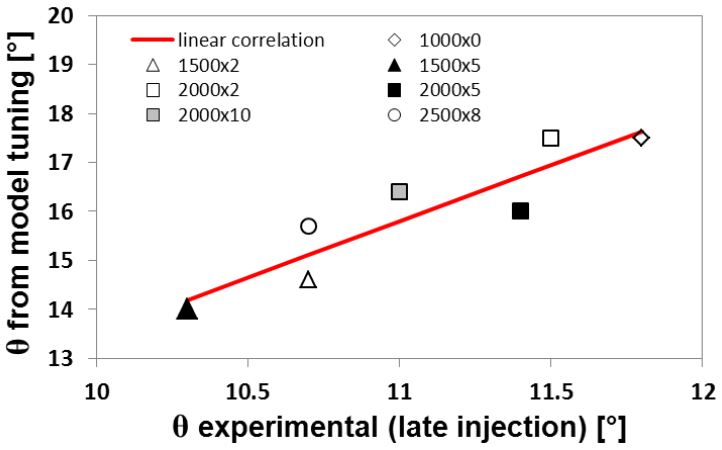

Figure B.1: Model tuning versus experimental cone angles.

To characterize the vapor spray boundaries in the model, greater values of the cone angle (θ_{model}) are needed compared to the experimental ones. θ_{exp} indeed represents the liquid phase cone angle and spans from 10° to 12°. The correlation AB.1 seems to predict quite well the cone angle to use as input in the model in all the engine conditions. This result is very encouraging because it allows to calculate the model cone angle using the experimental measurements. In addition to this analysis, a deep investigation has been made also to find a correlation between the vapor cone angle and the fuel/ambient properties starting from the equation of Siebers [14]:

$$\theta_{Siebers} = 2 \cdot \arctan\left\{ c \cdot \left[\left(\frac{\rho_a}{\rho_f} \right)^{0.19} - 0.0043 \sqrt{\frac{\rho_f}{\rho_a}} \right] \right\} \qquad (AB.2)$$

where '*c*' is a constant value set to 0.26 in [14]; ρ_a and ρ_f are the air and the fuel density, respectively. In figure B.2, the Siebers' cone angle from Eq. (AB.2) has been reported for different densities ratio (solid line with triangles). Also the cone angles from model tuning have been plotted (dashed line with squares). The figure shows that the Siebers' values are aligned along a straight line due to the monotonic dependence on the density ratio. On the contrary, some oscillations can be observed for the model tuning cone angles. In the present work, more than one parameter is changing simultaneously between the different engine conditions. In particular, the fuel injected quantity and the intake air mass are changing. The square root of the air mass flow/fuel consumption ratio has been reported in figure B.2 as a solid line with diamond markers. The same oscillations of the model cone angles have been obtained.

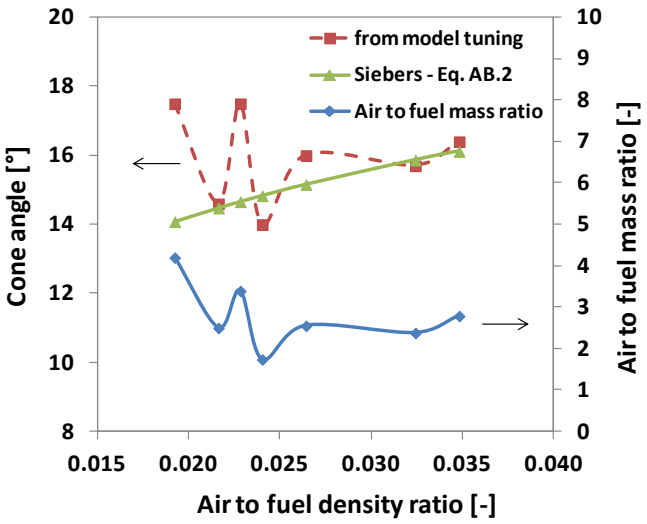

Figure B.2: Model tuning versus experimental cone angles.

For this reason, the air to fuel mass ratio has been used to correct the Siebers' equation for the application to the optical engine. The final equation for the model cone angle is:

$$\theta_{Model} = 2 \cdot \arctan\left\{ c \cdot \left[\left(\frac{\rho_a}{\rho_f} \right)^{0.19} - 0.0043 \sqrt{\frac{\rho_f}{\rho_a}} \right] \cdot \sqrt{\frac{m_a}{m_f}} \right\} \qquad (AB.3)$$

The constant value '*c*' is the calibration parameter to be optimized when applying the correlation on different engines. Figure B.3 (left) shows the comparison between the model cone angle and Eq. (AB.3) using c = 0.18. The curves have the same shape, and percentage error is lower than 12%

(figure B.3, right). Since the cone angle is a tuning parameter in the 1D model, the use of Eq. (AB.1) or Eq. (AB.3) to evaluate it has been very helpful and has allowed to understand deeply the model.

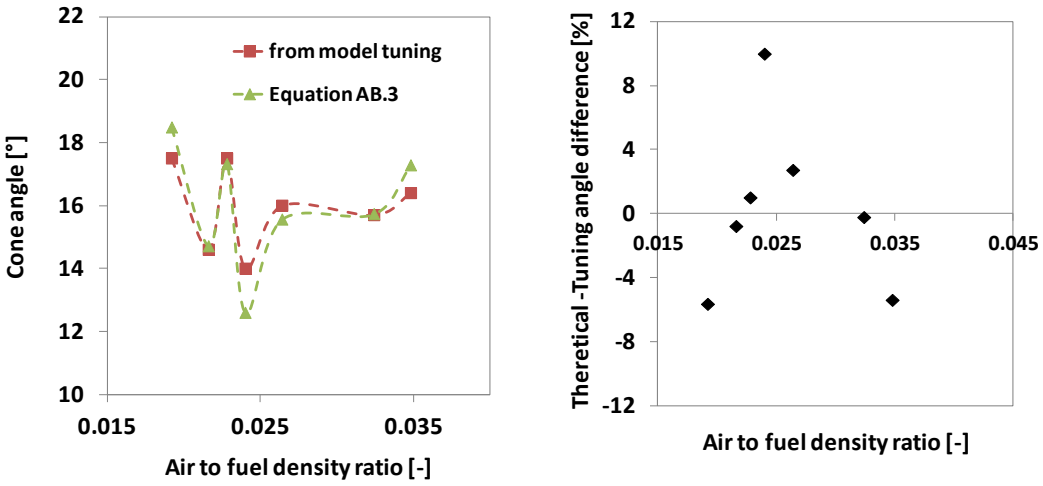

Figure B.3: Comparison between cone angle from model tuning and Eq. AB.3 (left), and percentage error (right).

APPENDIX C: Calculation of fuel vapor mass and evaporation rate

As affirmed several times in the text, the model of fuel injection by Musculus and Kattke [15] was not built to take into account the fuel vapor phase. However, assuming the process of vaporization is mixing limited [14, 18], a distinction between the fuel and vapor phase can be made upon the local equivalence ratio. In fact, it exits a threshold value depending on fuel composition and thermodynamic properties under which the fuel can be considered as completely vaporized. According to this assumption, the liquid penetration has been found by evaluating the equivalence ratio along the jet axis. However, this kind of analysis can only find the last element where fuel was in the liquid phase but it lacks of information about the state of the fuel inside the element. Assuming the hypothesis of self-similarity of properties along the transverse profile of the jet, higher fuel concentration is expected in the center and lower ones on the boundaries. This means that there is a liquid jet core surrounded by vaporized fuel.

To calculate the vapor and liquid phase inside a single element the approach used consisted in analyzing the radial profile of the jet and identifying the portions that were above and under the turbulent mean fuel volume fraction threshold derived from the equivalence ratio threshold. The region with higher values corresponded to the liquid part and the one with lower values to the vaporized one. Figure AC.1 describes the approach used.

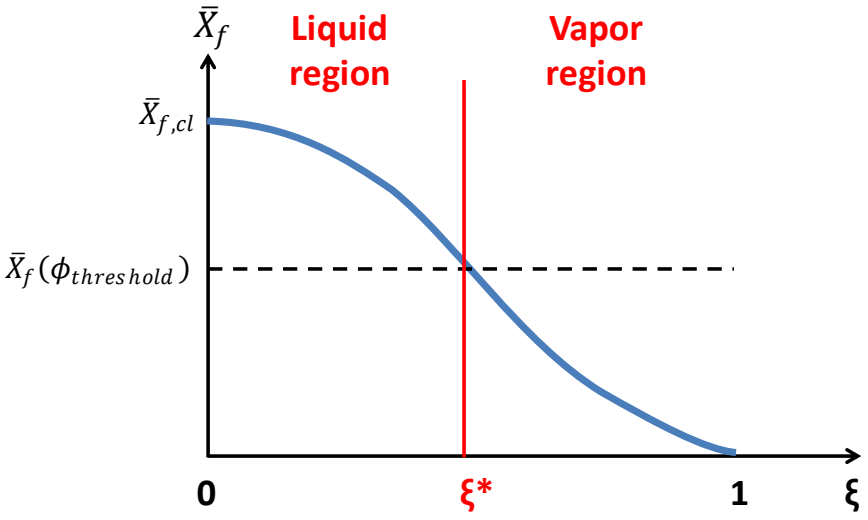

Figure AC.1: Radial profile of the turbulent mean fuel volume faction. The threshold value identify the liquid and vapor phase inside the element.

The turbulent mean fuel volume faction in a discrete volume element is the ratio between the fuel volume and the element volume:

$$\bar{X}_f = \frac{V_f}{V} \qquad (AC.1)$$

The variation of fuel fraction along the radial profile is assumed to follows the Abramovich profile [67]:

$$\frac{\bar{X}_f}{\bar{X}_{f,cl}} = (1 - \xi^{\alpha})^2 \qquad (AC.2)$$

The subscript *cl* denotes the value on the jet centerline, ξ=*r/R* is the ratio between the local radial coordinate *r* and the jet width *R=tan(ϑ/2)z* (z is the distance from the virtual jet origin), and α is a shape parameter of the Abramovich profile.

Once the threshold of equivalence ratio $\Phi_{threshold}$ is identified, the normalized radial position ξ* corresponding to $\bar{X}_f(\phi_{threshold})$ can be calculated as:

$$\xi^* = \left(1 \pm \sqrt{\frac{\bar{X}_f(\phi_{threshold})}{X_{f,cl}}}\right)^{1/\alpha} \qquad (AC.3)$$

where $\bar{\bar{X}}_f(\phi)$ is the following:

$$\bar{\bar{X}}_f(\phi) = \frac{\phi\rho_a}{\rho_f\left(\frac{m_a}{m_f}\right)_{st} + \phi\rho_a} \qquad (AC.4)$$

And the centerline quantity $X_{f,cl}$ can be related to the cross-sectionally averaged fuel volume fraction $\bar{\bar{X}}_f$ by:

$$\bar{\bar{X}}_f = \frac{\int \bar{X}_f dA}{\int dA} = 2X_{f,cl}\int_0^1 (\xi - 2\xi^{\alpha+1} + \xi^{2\alpha+1})d\xi \qquad (AC.5)$$

Knowing the value ξ* for which the fuel can be considered as liquid, the integration limits of eq. AC.5 can be modified and the following expression for $\bar{\bar{X}}_f liq$ is obtained:

$$\bar{\bar{X}}_f liq = 2X_{f,cl}\int_0^{\xi^*}(\xi - 2\xi^{\alpha+1} + \xi^{2\alpha+1})d\xi = 2X_{f,cl}\left(\frac{\xi^*}{2} - \frac{2\xi^{*2}}{\alpha+2} + \frac{\xi^{*2\alpha+2}}{2\alpha+2}\right) \quad (AC.6)$$

Equation AC.6 allows to calculate the volume and mass of the liquid phase and then of the vapor phase according to the following relationships:

$$V_f liq = \frac{\bar{\bar{X}}_f liq}{V} \quad (AC.7)$$

$$m_f liq = V_f liq \cdot \rho_f \quad (AC.8)$$

$$V_f vap = V_f - V_f liq \quad (AC.9)$$

$$m_f vap = m_f - m_f liq \quad (AC.10)$$

Finally, the total liquid and vapor mass in the jet can be calculated by integrating along the z axis.

$$m_f liq\ tot = \int m_f liq(z)dz \quad (AC.11)$$

$$m_f vap\ tot = \int m_f vap(z)dz \quad (AC.12)$$

and the evaporation rate is:

$$\frac{d}{dt}\left(m_f vap\ tot(t)\right) \quad (AC.13)$$

Nomenclature

Acronyms

ASOI	After Start Of Injection
ATDC	After Top Dead Center
BDC	Bottom Dead Center
BMEP	Brake Mean Effective Pressure
CCD	Charge Coupled Device
C-H	Carbon Hydrogen Single Bond
CI	Compression Ignition
CO	Carbon Monoxide
CO_2	Carbon Dioxide
CV	Coefficient Of Variation
DI	Direct Injection
ECU	Electronic Control Unit
EGR	Exhaust Gas Recirculation
ET	Energizing Time
F/A	Fuel/Air Ratio
FID	Flame Ionization Detector
FSN	Filter Smoke Number
GHG	Greenhouse Gases
ICE	Internal Combustion Engine
IDI	Indirect Injection
IR	Infrared
LIF	Laser Induced Fluorescence
ND1	Neutral Density Filter With 10% Attenuation
NDIR	Non-Dispersive Infrared
NEDC	New European Driving Cycle
NOx	Nitrogen Oxides
OH	Hydroxyl Radical
PAH	Poly-Aromatic Hydrocarbons
PM	Particulate Matter
ROHR	Rate Of Heat Release
ROI	Rate Of Injection
SI	Spark Ignition
SOI	Start Of Injection
TDC	Top Dead Center

Symbols

A	Jet cross sectional area
B	Fuel/air ratio threshold for evaporation
C_a	Orifice coefficient of area-contraction
C_i	Concentration of the species *i*
L	Optical length
M	Molecular weight, Momentum
$\dot{M}$	Momentum flow
Q	Heat
Q_λ	Absorption efficiency
R	Gas constant, Jet width
S	Penetration
T	Temperature
U	Velocity, Internal energy
U_0	Initial velocity
V	Volume
W	Work
X	Volume fraction
Z	Compressibility
1d	Mono-dimensional
a	Coefficient
b	Coefficient
c_p	Specific heat at constant pressure
c_v	Specific heat at constant volume
d_0	Nominal diameter of the nozzle
h	Specific enthalpy
$\dot{m}$	Mass flow rate
r	Local radial coordinate
t	Time
t_{br}	Time break-up

Greek symbols

Δp	Pressure difference
Φ	Equivalence ratio
α	Shape parameter of the Abramovich profile
γ	Specific heat ratio c_p/c_v
θ	Measured spray angle, Crank angle
λ	Wavelength
ξ	Normalized radial distance

ρ	Density

Subscripts

a	Air
cl	Centerline
f	Fuel
liq	Liquid
s	Saturation condition
st	Stoichiometric
vap	Vapor

List of Figures

List of Tables

References

[1] C. L. Cummins, *Internal fire*. Carnot Press, 1976.

[2] J. B. Heywood *et al.*, *Internal combustion engine fundamentals*. McGraw-Hill New York, 1988, vol. 930.

[3] EU emissions standards. available at http:/www.dieselnet.com/standards/eu/ld.php.

[4] http://appsso.eurostat.ec.europa.eu/nui/show.do?wai=true&dataset=demo_find.

[5] http://www.npr.org/sections/thetwo-way/2015/10/08/446861855/volkswagen-u-s-ceo-faces-questions-on-capitol-hill, it was installed for this purpose,' VW's U.S. CEO tells congress about defeat device, 8 oct 2015.

[6] http://www.bbc.com/news/business-34712435, volkswagen says 800,000 cars may have false CO2 levels, 4 nov 2015.

[7] http://www.bbc.com/news/business-34352243, vw could face long legal nightmare, 24 sep 2015.

[8] A. Leipertz and M. Wensing, "Modern optical diagnostics in engine research," in *Journal of Physics: Conference Series*, vol. 85, no. 1. IOP Publishing, 2007, p. 012001.

[9] G. S. Settles, *Schlieren and shadowgraph techniques: visualizing phenomena in transparent media*. Springer Science & Business Media, 2012.

[10] H. Zhao, *Laser diagnostics and optical measurement techniques in internal combustion engines*, 2012.

[11] H. Zhao and N. Ladommatos, *Engine combustion instrumentation and diagnostics,* Warrendale, PA: Society of automotive engineers inc.)," 2001.

[12] M. Jansons, S. Lin, and K. Rhee, "Infrared spectral analysis of engine preflame emission," *International Journal of Engine Research*, vol. 9, no. 3, pp. 215–237, 2008.

[13] L. Dombrovsky, S. Sazhin, S. Mikhalovsky, R. Wood, and M. Heikal, "Spectral properties of diesel fuel droplets," *Fuel*, vol. 82, no. 1, pp. 15–22, 2003.

[14] D. L. Siebers, "Scaling liquid-phase fuel penetration in diesel sprays based on mixing-limited vaporization," SAE technical paper, 1999-01-0528, 1999.

[15] M. P. Musculus and K. Kattke, "Entrainment waves in diesel jets," *SAE International Journal of Engines*, vol. 2, no. 1, pp. 1170–1193, 2009.

[16] R. Payri, F. Salvador, J. Gimeno, and J. De la Morena, "Influence of injector technology on injection and combustion development–part 1: Hydraulic characterization," *Applied Energy*, vol. 88, no. 4, pp. 1068–1074, 2011.

[17] R. Payri, F. Salvador, J. Gimeno, and J. De la Morena, "Influence of injector technology on injection and combustion development–part 2: Combustion analysis," *Applied Energy*, vol. 88, no. 4, pp. 1130–1139, 2011.

[18] J. D. Naber and D. L. Siebers, “Effects of gas density and vaporization on penetration and dispersion of diesel sprays,” Sandia National Laboratory, No. CONF-960204, 1996.

[19] S. Kook, C. Bae, P. C. Miles, D. Choi, M. Bergin, and R. D. Reitz, “The effect of swirl ratio and fuel injection parameters on co emission and fuel conversion efficiency for high-dilution, low-temperature combustion in an automotive diesel engine,” *SAE paper*, pp. 01–0197, 2006.

[20] C. Baumgarten, *Mixture formation in internal combustion engines*. Springer Science & Business Media, 2006.

[21] C. Arcoumanis, M. Gavaises, and B. French, “Effect of fuel injection processes on the structure of diesel sprays,” SAE Technical Paper, 970799, 1997.

[22] S. Hwang, Z. Liu, and R. D. Reitz, “Breakup mechanisms and drag coefficients of high-speed vaporizing liquid drops,” *Atomization and Sprays*, vol. 6, no. 3, 1996.

[23] S. A. Krzeczkowski, “Measurement of liquid droplet disintegration mechanisms,” *International Journal of Multiphase Flow*, vol. 6, no. 3, pp. 227–239, 1980.

[24] H. Hiroyasu and M. Arai, “Structures of fuel sprays in diesel engines,” SAE Technical Paper, 900475, 1990.

[25] H. Hiroyasu and M. Arai, “Fuel spray penetration and spray angle in diesel engines,” *Trans. JSAE*, vol. 21, no. 5, p. 11, 1980.

[26] M. Arai, M. Tabata, H. Hiroyasu, and M. Shimizu, “Disintegrating process and spray characterization of fuel jet injected by a diesel nozzle,” SAE Technical Paper, 840275, 1984.

[27] F. Payri, J. Desantes, and J. Arregle, “Characterization of di diesel sprays in high density conditions,” *SAE transactions*, vol. 105, pp. 1085–1094, 1996.

[28] J. Dent, “A basis for the comparison of various experimental methods for studying spray penetration,” SAE Technical Paper, 710571, 1971.

[29] J. Jiménez, F. Castro, F. Tinaut, and B. Gimenez, “The tip evolution of an evaporative intermittent fuel spray,” in *Thermo-and Fluid-dynamic Processes in Diesel Engines: Selected Papers from the THIESEL 2000 Conference Held in Valencia, Spain, September 13-15, 2000*. Springer Verlag, 2002, p. 175.

[30] C. Bae, J. Yu, J. Kang, J. Kong, R. Cuenca, and K. Lee, “The influence of injector parameters on diesel spray,” 2002.

[31] J. E. Dec, “A conceptual model of di diesel combustion based on laser-sheet imaging*,” SAE technical paper, 970873, 1997.

[32] P. F. Flynn, R. P. Durrett, G. L. Hunter, A. O. zur Loye, O. Akinyemi, J. E. Dec, and C. K. Westbrook, “Diesel combustion: an integrated view combining laser diagnostics, chemical kinetics, and empirical validation,” 1999.

[33] H. K. Newhall and S. Shahed, “Kinetics of Nitric Oxide formation in high-pressure flames,” in *Symposium (International) on Combustion*, vol. 13, no. 1. Elsevier, 1971, pp. 381–389.

[34] B. S. Haynes and H. G. Wagner, “Soot formation,” *Progress in Energy and Combustion Science*, vol. 7, no. 4, pp. 229–273, 1981.

[35] R. Jorach, R. Judge, B. Annycke, and F. Lamacchia, “Diesel common rail fuel systems technology for high efficiency ultra-low emissions medium duty engines,” in *Fuel Systems for {IC} Engines*, IMechE, Ed. Woodhead Publishing, 2012, pp. 141 – 154. [Online]. Available: http://www.sciencedirect.com/science/-article/pii/B9780857092106500118

[36] M. Twigg, “Advanced integrated exhaust aftertreatment systems and the mechanisms of {NOx} emissions control,” in *Internal Combustion Engines: Performance, Fuel Economy and Emissions*, IMechE, Ed. Woodhead Publishing, 2013, pp. 219 – 229. [Online]. Available: http://www.sciencedirect.com/science/-article/pii/B9781782421832500172

[37] M. P. Musculus, J. E. Dec, and D. R. Tree, “Effects of fuel parameters and diffusion flame lift-off on soot formation in a heavy-duty di diesel engine,” SAE Technical Paper, 2002-01-0889, 2002.

[38] D. R. Tree and K. I. Svensson, “Soot processes in compression ignition engines,” *Progress in Energy and Combustion Science*, vol. 33, no. 3, pp. 272–309, 2007.

[39] Ö. Andersson, “Diesel combustion” in *Handbook On Combustion*, 2010.

[40] G. A. Lavoie, J. B. Heywood, and J. C. Keck, “Experimental and theoretical study of nitric oxide formation in internal combustion engines,” *Combustion science and technology*, vol. 1, no. 4, pp. 313–326, 1970.

[41] K. Akihama, Y. Takatori, K. Inagaki, S. Sasaki, and A. M. Dean, “Mechanism of the smokeless rich diesel combustion by reducing temperature,” SAE technical paper, 2001-01-0655, 2001.

[42] T. Kamimoto and M. Bae, “High combustion temperature for the reduction of particulate in diesel engines,” Society of Automotive Engineers, Warrendale, PA, 1988.

[43] F. W. Bowditch, “A new tool for combustion research a quartz piston engine,” SAE Technical Paper, 610002, 1961.

[44] U. Aronsson, “Processes in optical diesel engines - emissions formation and heat release,” Ph.D. dissertation, Department of Energy Sciences, Faculty of Engineering, Lund University, 2011.

[45] M. Jansons, R. Florea, K. Zha, and E. Gingrich, “The effect of HCHO addition on combustion in an optically accessible diesel engine fueled with JP-8,” *SAE Int. J. Fuels Lubr*, vol. 3, no. 2, pp. 671–690, 2010.

[46] W. E. Eagle, L.-M. Malbec, and M. P. Musculus, “Comparing vapor penetration measurements from ir thermography of c-h stretch with schlieren during fuel injection in a heavy-duty diesel engine,” in *9th U. S. National Combustion Meeting Organized by the Central States Section of the Combustion Institute May 17-20, 2015 Cincinnati, Ohio*, 2015.

[47] U. Aronsson, C. Chartier, Ö. Andersson, R. Egnell, J. Sjöholm, M. Richter, and M. Aldén, “Analysis of the correlation between engine-out particulates and local in the lift-off region of a heavy duty diesel engine using Raman spectroscopy,” *SAE International Journal of Fuels and Lubricants*, vol. 2, no. 1, pp. 645–660, 2009.

[48] E. Mancaruso, L. Sequino, and B. M. Vaglieco, “First and second generation biodiesels spray characterization in a diesel engine,” *Fuel*, vol. 90, no. 9, pp. 2870–2883, 2011.

[49] EU, 2009, regulation (EC) no 443/2009, official journal of European Union, 5.6.2009, l 140/1.

[50] E. Mancaruso and B. M. Vaglieco, “Spectroscopic measurements of premixed combustion in diesel engine,” *Fuel*, vol. 90, no. 2, pp. 511–520, 2011.

[51] Z. Hu, L. Somers, T. Davies, A. McDougall, and R. Cracknell, “A study of liquid fuel injection and combustion in a constant volume vessel at diesel engine conditions,” *Fuel*, vol. 107, pp. 63–73, 2013.

[52] A. K. Agarwal, S. Som, P. C. Shukla, H. Goyal, and D. Longman, “In-nozzle flow and spray characteristics for mineral diesel, karanja, and jatropha biodiesels,” *Applied Energy*, vol. 156, pp. 138–148, 2015.

[53] L. M. Pickett, J. Manin, A. Kastengren, and C. Powell, “Comparison of near-field structure and growth of a diesel spray using light-based optical microscopy and x-ray radiography,” *SAE International Journal of Engines*, vol. 7, no. 2, pp. 1044–1053, 2014.

[54] F. Payri, R. Payri, M. Bardi, and M. Carreres, “Engine combustion network: influence of the gas properties on the spray penetration and spreading angle,” *Experimental Thermal and Fluid Science*, vol. 53, pp. 236–243, 2014.

[55] L. M. Pickett, J. Manin, C. L. Genzale, D. L. Siebers, M. P. Musculus, and C. A. Idicheria, “Relationship between diesel fuel spray vapor penetration/dispersion and local fuel mixture fraction,” *SAE International Journal of Engines*, vol. 4, no. 1, pp. 764–799, 2011.

[56] J.-G. Nerva, C. L. Genzale, S. Kook, J. M. Garcá-Oliver, and L. M. Pickett, “Fundamental spray and combustion measurements of soy methyl-ester biodiesel,” *International Journal of Engine Research*, vol. 14, no. 4, pp. 373–390, 2013.

[57] J. V. Pastor, J. J. López, J. M. Garcá, and J. M. Pastor, “A 1d model for the description of mixing-controlled inert diesel sprays,” *Fuel*, vol. 87, no. 13, pp. 2871–2885, 2008.

[58] E. C. Trujillo, F. J. Jiménez-Espadafor, J. A. B. Villanueva, and M. T. Garcá, “Methodology for the estimation of cylinder inner surface temperature in an air-cooled engine,” *Applied Thermal Engineering*, vol. 31, no. 8, pp. 1474–1481, 2011.

[59] R. Royo, M. Albertos-Arranz, J. Cárcel-Cubas, and J. Payá, “Thermographic study of the preheating plugs in diesel engines,” *Applied Thermal Engineering*, vol. 37, pp. 412–419, 2012.

[60] R. Royo, “Characterization of automotion brake thermal conditions by the use of infrared thermography,” *Infrared Training Center and FLIR Systems*, pp. 259–266, 2004.

[61] R. Royo, “Characterization of the exhaust flow in the catalytic converter of a spark ignition engine using infrared thermography,” *The Infrared Training Center*, pp. 192–200, 2003.

[62] G. Stumpp and M. Ricco, “Common rail-an attractive fuel injection system for passenger car di diesel engines,” *SAE paper*, vol. 960870, no. 1, p. 996, 1996.

[63] N. Guerrassi and P. Dupraz, “A common rail injection system for high speed direct injection diesel engines,” SAE Technical Paper, 980803, 1998.

[64] J. Schommers, F. Duvinage, M. Stotz, A. Peters, S. Ellwanger, K. Koyanagi, and H. Gildein, “Potential of common rail injection system for passenger car di diesel engines,” SAE Technical Paper, 2000-01-0944, 2000.

[65] BOSCH, *Diesel-engine management Common Rail*. SAE INTERNATIONAL, 2nd edition, 1999.

[66] K. Kuo, “Principles of combustionjohn wiley,” *New York*, 1986.

[67] G. N. Abramovich, *Chapter 5: Jet of an Incompressible Fluid in a Coflowing Exte Stream - The Theory of Turbulent Jets*, U. Cambridge, MA, Ed. The MIT Press, 1963.

[68] L. M. Pickett, J. Manin, R. Payri, M. Bardi, and J. Gimeno, “Transient rate of injection effects on spray development,” SAE Technical Paper, 2013-24-0001, 2013.

[69] CMT website. “virtual injection rate generator” <http://www.cmt.upv.es/ecn09.aspx>.

[70] X. Tauzia, A. Maiboom, and G. Ma, “A 1d model for diesel sprays under reacting conditions,” SAE Technical Paper, Tech. Rep., 2015.

[71] Engine Combustion Network data archive. <http://www.sandia.gov/ecn/>.

[72] D. R. Lide, *CRC handbook of chemistry and physics*. CRC press, 2004.

[73] U. Aronsson, C. Chartier, U. Horn, Ö. Andersson, B. Johansson, and R. Egnell, “Heat release comparison between optical and all-metal hsdi diesel engines,” SAE Technical Paper 2008-01-1062, doi:10.4271/2008-01-1062, Tech. Rep., 2008.

[74] D. Pavia, G. Lampman, G. Kriz, and J. Vyvyan, *Introduction to spectroscopy*. Cengage Learning, 2008.

[75] E. Tomita, N. Kawahara, A. Nishiyama, and M. Shigenaga, “In situ measurement of hydrocarbon fuel concentration near a spark plug in an engine cylinder using the 3.392 μm infrared laser absorption method: application to an actual engine,” *Measurement Science and Technology*, vol. 14, no. 8, p. 1357, 2003.

[76] A. E. Klingbeil, J. B. Jeffries, and R. K. Hanson, “Temperature-dependent mid-IR absorption spectra of gaseous hydrocarbons,” *Journal of Quantitative Spectroscopy and Radiative Transfer*, vol. 107, no. 3, pp. 407–420, 2007.

[77] N. Rahmat, A. Z. Abdullah, and A. R. Mohamed, “Recent progress on innovative and potential technologies for glycerol transformation into fuel additives: a critical review,” *Renewable and Sustainable Energy Reviews*, vol. 14, no. 3, pp. 987–1000, 2010.

[78] W. Bosch, “The fuel rate indicator: A new measuring instrument for display of the characteristics of individual injection,” SAE technical paper, SAE 660749,” 1966.

[79] www.horiba.com.

[80] R. D. Atkins, *An introduction to engine testing and development*. SAE International Warrendale, 2009.

[81] J. Holman, *Experimental methods for engineers*, McGraw-Hill, Singapore, 1994, pp. 49-103.

[82] R. Finesso, E. Spessa, E. Mancaruso, L. Sequino, and B. M. Vaglieco, "Assessment of a new quasi-dimensional multizone combustion model for the spray and soot formation analysis in an optical single cylinder diesel engine," *SAE International Journal of Engines*, vol. 6, no. 3, pp. 1677–1693, 2013.

[83] H. Zhao, *Advanced Direct Injection Combustion Engine Technologies and Development: Diesel Engines*. Elsevier, 2009, vol. 2.

[84] E. Mancaruso, B. M. Vaglieco, and L. Sequino, "Using 2d infrared imaging for the analysis of non-conventional fuels combustion in a diesel engine," *SAE International Journal of Engines*, vol. 8, no. 5, pp. 1701–1715, 2015.

[85] J. Benajes, J. M. Garcá-Oliver, R. Novella, and C. Kolodziej, "Increased particle emissions from early fuel injection timing diesel low temperature combustion," *Fuel*, vol. 94, pp. 184–190, 2012.

[86] C. Beatrice, G. Di Blasio, M. Lazzaro, E. Mancaruso, R. Marialto, L. Sequino, and B. M. Vaglieco, "Investigation of the combustion in both metal and optical diesel engines using high-glycerol ethers/diesel blends," *International Journal of Engine Research*, vol. 16, no. 1, pp. 38–51, 2015.

[87] E. Mancaruso, L. Sequino, and B. M. Vaglieco, "IR digital imaging for analysing in-cylinder combustion process in transparent diesel engine," in *Photonics Technologies, 2014 Fotonica AEIT Italian Conference on*. IEEE, 2014, pp. 1–4.

[88] E. Mancaruso, L. Sequino, and B. M. Vaglieco, "2d infrared imaging at different wavelengths to characterize the air/fuel interactions in diesel engine," in *10th Pacific Symposium on Flow Visualization and Image Processing Naples, Italy, 15-18 June, 2015*, 2015.

[89] E. Mancaruso, R. Marialto, L. Sequino, and B. M. Vaglieco, "Comparison of spray characteristics measured in an optical single cylinder diesel engine with 1d model," SAE Technical Paper, Tech. Rep., 2014.

[90] C. Rakopoulos, K. Antonopoulos, and D. Rakopoulos, "Development and application of multi-zone model for combustion and pollutants formation in direct injection diesel engine running with vegetable oil or its bio-diesel," *Energy conversion and management*, vol. 48, no. 7, pp. 1881–1901, 2007.

[91] C. Rakopoulos, K. Antonopoulos, and D. Rakopoulos, "Multi-zone modeling of diesel engine fuel spray development with vegetable oil, bio-diesel or diesel fuels," *Energy Conversion and Management*, vol. 47, no. 11, pp. 1550–1573, 2006.

[92] C. Rakopoulos, K. Antonopoulos, D. Rakopoulos, and D. Hountalas, "Multi-zone modeling of combustion and emissions formation in di diesel engine operating on ethanol–diesel fuel blends," *energy conversion and management*, vol. 49, no. 4, pp. 625–643, 2008.

[93] N. Stamoudis, C. Chryssakis, and L. Kaiktsis, "A two-component heavy fuel oil evaporation model for CFD studies in marine diesel engines," *Fuel*, vol. 115, pp. 145–153, 2014.